Delft University of Technology

A numerical heat transfer study on spheres and droplets in two-phase flows

Taleban Fard, Nafiseh

Important note
To cite this publication, please use the final published version (if applicable).
Please check the document version above.

A numerical heat transfer study on spheres and droplets in two-phase flows

Nafiseh Talebanfard

A numerical heat transfer study on spheres and droplets in two-phase flows

Proefschrift

ter verkrijging van de graad van doctor

aan de Technische Universiteit Delft,

op gezag van de Rector Magnificus Prof. dr. ir. T.H.J.J. van der Hagen,

voorzitter van het College voor Promoties,

in het openbaar te verdedigen op woensdag 5 september 2018 om 15:00 uur.

door

Nafiseh TALEBANFARD

Master of Science in Mechanical Engineering,

Ferdowsi University of Mashhad, Iran

geboren te Shiraz, Iran

Dit proefschrift is goedgekeurd door de promotor:

Prof. dr. ir. B. J. Boersma

Samenstelling promotiecommissie bestaat uit:

Rector magnificus	voorzitter
Prof. dr. ir. B.J. Boersma	Technische Universiteit Delft, promotor

Onafhankelijke leden:

Prof. dr. D.J.E.M Roekaerts	Technische Universiteit Delft
Prof. dr. ir. C. Vuik	Technische Universiteit Delft
Prof. dr. A.E.P. Veldman	Rijksuniversiteit Groningen
Prof. dr. ir. R.A.W.M. Henkes	Technische Universiteit Delft
Prof. dr. ir. J.G.M. Kuerten	Technische Universiteit Eindhoven
Dr. ir. D. van der Heul	Technische Universiteit Delft

Contents

Summary

A numerical heat transfer study on spheres and droplets in two-phase flows

In many industrial processes droplets are present with different physical and chemical properties. Heat transfer from droplets as a major step is present in many different processes, such as spray drying, combustion, spray cooling, etc. The purpose of the present research is to investigate heat transfer in deforming droplets.

As an initial step the problem of heat transfer in a solid sphere where the temperature of the sphere is assumed to remain constant is considered. The model is validated by comparison with literature results. The effect of the mesh size on the accuracy of the Nusselt number is also investigated. As next step, the heat transfer from a solid sphere in which there is internal temperature distribution is considered to show the effect of the variable surface temperature on heat transfer rate. This is presented by the variation of the local and average Nusselt number. The results show that the internal temperature distribution affects the heat transfer rate significantly. Therefore, to have a reliable estimation of the local Nusselt number, the internal temperature distribution and the local variation of the surface temperature of the particle should also be considered. The result of the mesh sensitivity study shows that the grid resolution while does not significantly affect the average Nusselt number but affects the local Nusselt number at the front stagnation point and at the rear of the particle, therefore a proper mesh resolution should be used.

By using a coupled level-set and volume of fluid method the problem of heat transfer from deforming droplets are solved as the final step. The deformation of droplets as well as the location of the droplet in the domain can be captured with this method. Although the level-set method is not mass conserving, coupling it with the volume of fluid method provides mass conservation. The case of a falling droplet and colliding droplets with different geometrical configurations for different Reynolds and Weber numbers are considered.

In the study of heat transfer over a falling and deforming water droplet in air for different Weber and Reynolds numbers, the results show that in order to have a reliable estimation of the local Nusselt number, the internal temperature distribution should be considered. In this way the correct local surface temperature of the droplet which is used in the Nusselt number calculations is obtained. A cyclic deformation is observed in the surface area of a falling droplet for which the period increases by increasing the Weber number. Since in the calculation of the Nusselt number the surface area is used, it is important to use the correct surface area from which the heat is being transferred.

The sensitivity study of the heat transfer rate to the Reynolds number and the Weber number shows that increasing the Reynolds number and Weber number both increase the Nusselt number. However, the effect of the Reynolds number variation is more significant.

The flow and heat transfer in colliding droplets is studied in 3D for different Weber numbers, Reynolds numbers and eccentricity of droplets. Droplets are allowed to deform under the hydrodynamic forces of the surrounding flow. A coupled level-set and volume of fluid (CLSVOF) method is applied to model the highly deforming topology of the droplets. The temperature distribution inside the droplet as well as the outer domain is considered and the consequent effect on the Nusselt number is studied.

The results show that the eccentricity of droplets has a significant effect on the Nusselt number. If the droplets deform considerably due to the collision, the heat transfer from the droplets will be strongly enhanced. It is concluded from the calculations for different Reynolds numbers that heat transfer rate is increased by increasing the Reynolds number. The surface tension controls the extent of deformations, so increasing the Weber number for a certain approach velocity results in larger deformations in droplets and therefore a higher heat transfer rate is achieved. The role of using the real surface area of droplets in calculation of the Nusselt number is also studied, it is concluded that in problems with high Weber numbers it is required that the real surface area is used in the heat transfer calculations. On the other hand, for cases with lower Weber numbers in which the deformations are negligible, using the real surface area is not necessary.

In the study of flow and heat transfer in colliding droplets two different solvers for pressure and velocity have been used: an iterative solver and a direct solver. Since the direct solver is computationally less effortful and much faster than the iterative solver it can be applied on finer meshes. Therefore, results with higher resolution and less numerical instabilities can be achieved which makes the direct solver a suitable choice to solve problems with large topological changes.

1   Introduction

1.1 Background and motivation

Droplets and bubbles are observed in different shapes and sizes in nature, such as in rain or waterfall mists and in various fields of industry, from food industry to oil and gas production. In many industrial applications droplets are present, such as spray combustion, spray drying, spray cooling, spray atomization, spray deposition, spray cleaning and surface treatment.

Droplets may form in different ways, such as, condensation, liquid breakup and melting. In many industrial applications, droplets are formed due to liquid break up like in atomization which in turn can be obtained by aerodynamic or mechanical forces, or by exposing the liquid to ultrasonic or electrostatic fields. The size and shape of droplets are of high importance in applications with discrete droplets, where reaction rates, cooling, solidification or evaporation rates are dependent on the surface area of droplets. Droplet deformation due to impact on a surface is also an important phenomenon, such

as, erosion in aircraft surfaces due to rain drops, or the erosion of turbine blades in wet steam.

When there are different phases present in a flow and each phase with its own properties, exchange of momentum, mass and energy may occur. Heat and mass transfer in droplets is important phenomena, such as evaporation of fuel droplets in internal combustion engines, film evaporation of water from the surface of biomass fuels and mass transfer to the absorbent droplets in CO_2 capture are a few examples. Some examples of industrial processes in which multiphase flows are present are as follows.
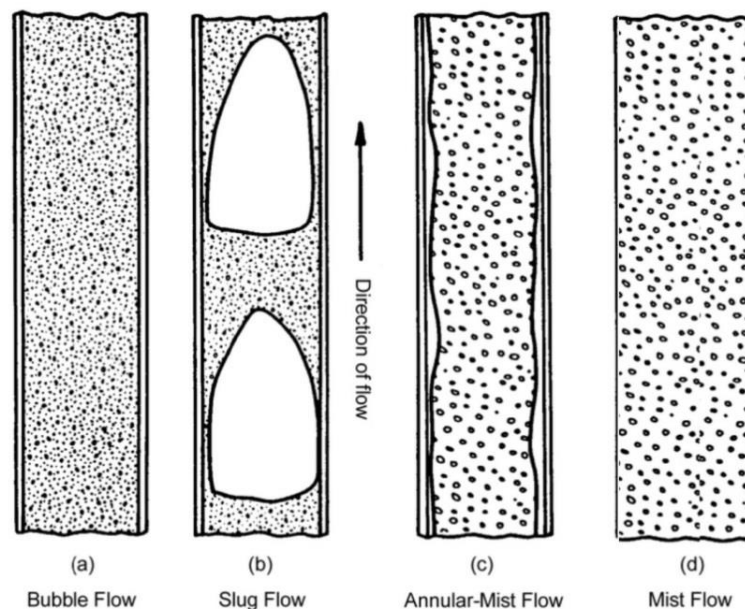
Figure 1.1 Flow regimes in a geothermal well.

In an oil pipeline, gas bubbles can assist in the lifting of the oil. On the other hand they affect the pressure, temperature and viscosity of the mixture in the pipeline. In some cases these droplets can coalesce and therefore, making liquid slugs in the pipeline which can cause damage to the pipeline due to vibrations. In a geothermal well, hot water and steam move upwards. Since the pressure of the fluid decreases along the pipeline, more vapors are produced in time, which can result in different flow regime as

shown in Figure 1.1. The vapor phase initially appears as spherical bubbles. As the concentration of the bubbles increases, they can coalesce to make irregular bubbles or elongated Taylor bubbles, this regime is known as the slug flow. When the concentration of the vapor goes even higher, an annular flow will form. The last stage is the droplet flow in which the liquid annulus evaporates due to low pressure and breaks into droplets. In boilers and burners almost all these regimes occur, but due to addition of heat at the end, droplets and the liquid film evaporate to vapor. Here, thermal instabilities may cause problems which have to be controlled. Another undesired evaporation is cavitation that can occur due to pressure drop below the vapor pressure. This evaporated liquid will rupture farther down in the form of droplets in the flow due to increase in the surrounding pressure. The result of these bursts is damage to the structure on which cavitation is occurring. Figure 1.2 shows how a cavitating flow looks like and how it can damage the structures.
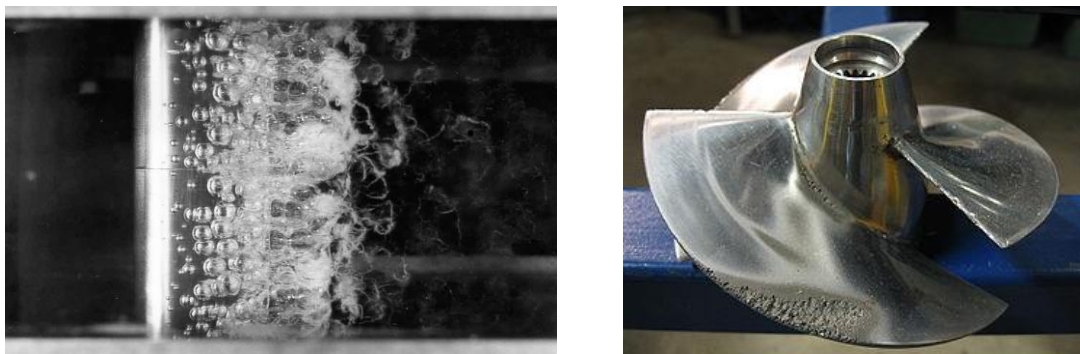
Figure 1.2 Cavitation near the maximum thickness of an airfoil. From Kermeen (1965) (left), damage caused by cavitation on a pump propeller (right).

Condensation is also an important phenomenon in many industrial applications, in which colder droplets are introduced into the steam through some spray nozzles. Vapor condenses when encountered with colder droplets and therefore, droplets grow in size. In this procedure heat transfer, droplet size, and relative velocity are important parameters. The evaporation can be done by adding bubbling steam, and the fractions of oil are condensed at different temperatures.

Spray drying can be used in food, pharmaceutical or chemicals production. This procedure is done by introducing a hot air flow through the spray of the material, the droplets evaporate due to heat exchange with the hot air flow and thus the material is

dried. Efficient heat transfer will enhance the production of dried material at the end of the procedure. In the review of the literature there is a wide range of research that has been performed on heat and mass transfer to or from droplets.

1.2 Literature review

The main interest in this work is the flow and heat transfer in deforming droplets. The relevant literature has been reviewed and the summary of the past work on this problem is presented in this section.

1.2.1 Experimental work on droplet heat transfer

In order to perform accurate measurements proper optical facilities are required. Different measurement techniques can be used to extract velocity and temperature fields. To track the velocity field, tracer particle can be added to the liquid phase. By using Particle Image Velocimetry (PIV) the velocity field can be measured. For temperature measurements a two-color laser-induced fluorescence (LIF) can be used to characterize the temporal evolution of the temperature field and to measure heat transfer a laser phase-Doppler anemometry (PDA) can be used.

There are many experimental studies on heat and mass transfer of multiphase flows with discrete droplets. Different optical equipment, various measurement techniques and facilities are applied to enhance the understanding of the physics of the problem and the characteristic parameters. The problem of flow over droplets and heat and mass transfer from them has been treated with different experimental means. The main issue in performing experiments is to have proper optical facilities to accurately capture the moving interfaces. In the study of Fujita, Kurose and Komori (2010) the effect of relative humidity on heat transfer of an evaporating water droplet in air flow is investigated. PIV is applied to measure the flow velocity as in the study by ten Cate et al. (2002). Castanet, Labergue and Lemoine (2011) have investigated the heat and mass transfer between the two phases of an evaporating droplet stream by using laser-induced fluorescence (LIF) techniques. They have used a two-color laser induced fluorescence to characterize the temporal mean temperature of droplets. To track the vapor phase acetone planar laser-induced fluorescence is used (PLIF) which is based on the absorption of the incident light by molecules which are excited to a higher energy level. A study on the measurement of heat transfer from hot surfaces to non-wetting droplets is performed by Chatzikyriakou et al. (2011) using transient, high resolution, infrared

microscopy and by observing a thin metallic layer from beneath through an infrared-transparent substrate. Another experimental study on droplet dynamics and heat transfer in spray cooling is performed by Jia and Qiu (2003). The incoming and outgoing droplets were characterized in situ with a newly developed laser phase-Doppler anemometry (PDA).

For an extensive review of literature on experimental studies on droplets the reader is referred to the experimental study of Oldenziel (2014) on droplet collisions in turbulence.

1.2.2 Computational work on droplet heat transfer

As the computers and also the numerical methods improved in time, further numerical studies performed in more detail with higher accuracy. To optimize the design of systems and machines, numerical modeling is an important step to have an estimate of the physics of the problem and to avoid expensive fabrication of small or large scale experimental models. Also there is the possibility of changing inputs more easily when working with the numerical models comparing to an actual system in which changing a specific parameter might not be feasible. The more the physics of the problem is known the closer one can get to a sustainable design.

In the early studies with lower performance computations, it was only possible to perform studies on one or two dimensional heat and mass transfer from droplets and the Reynold numbers were mostly limited to the laminar range of flow. In most of these studies the droplets are assumed to remain spherical (non-deforming droplets) or droplets with low Weber numbers were considered. Other assumptions were made on the temperature of the droplets. In some studies the droplets were assumed to have uniform temperature, and in some other studies the surface temperature of the droplets was assumed uniform.

To name a few examples of such studies the work of Galloway and Sage (1964) on thermal and material transfer in turbulent gas streams for spheres, Chen and Mucoglu (1977) on flow and heat transfer characteristics of laminar mixed forced and free convection about a sphere and Hayward and Pei (1978) on the local heat transfer of a sphere in turbulent air stream can be mentioned. In all of these studies the surface temperature is assumed to be uniform. Woo and Hamielec (1971) performed a numerical study of falling evaporating droplets for a Reynolds number up to 300 with axisymmetric flow assumption. The same assumption was used in the study of Prakash and Sirignano (1980) in which the radius of the droplet was also assumed to remain constant during evaporation. The changes of droplet radius has been considered with a

rescaling mesh in the study of Renksizbulut and Haywood (1988). However, two-dimensional axisymmetric equations were still solved. Even in some recent studies such as the work of Abou Al-Sood and Birouk (2008), Juncu (2010) and Castanet et al. (2011) still assumptions such as spherical droplets and uniform surface temperature are used. There are also studies on heat transfer in liquid droplets considering the internal circulation but the droplet is assumed to remain a sphere, Nguyen, Paik and Chung (1993).

To investigate the problem of flow and heat transfer in droplets comprehensively, the deformation of droplets and the internal temperature distribution should also be considered. The deformation of droplets will change the interface as well. Therefore, locating the interface is a major task in the computational approach to solve multiphase flows with topological changes. As it was mentioned in the previous section, there are different methods to capture the interface in multiphase flows. Therefore, this is a moving boundary problem, for which either Eulerian or Lagrangian methods can be used. Tracking methods are of Lagrangian nature, in these methods the interface between the phases is tracked by the marker points which are defined at the interface.

Examples of tracking methods are, front-tracking method as in Tryggvason et al. Tryggvason et al. (2001), the Constrained Interpolation Profile (CIP) method as in Hu and Kashiwagi (2004), Yabe, Xiao and Utsumi (2001) and Takizawa et al. (2007) and boundary integral such as study of Hou, Lowengrub and Shelley (2001). There are many studies using adaptive mesh or moving mesh for multiphase heat and mass transfer problems, such as study of Petera and Weatherley (2001) on mass transfer from a falling droplet, Quan, Lou and Schmidt (2009) using interface tracking in merging and breakup by using moving mesh. Adaptive mesh has been used by Anderson, Zheng and Cristini (2005) for simulation of multiphase flow, Quan and Schmidt (2007) for capturing interface curvature, Tan, Lim and Khoo (2007) for incompressible mixture flows and by Quan (2011) for multiphase flows interface tracking. In these studies the whole domain or a part of it has to be re-meshed every time step which makes them computationally expensive and therefore not suitable for problems with many droplets or with large topological changes.

In order to avoid the computational effort of re-meshing the domain, the governing equations can be solved on an Eulerian grid, using a front-capturing method to capture the interface location and shape. Examples of such methods are the volume of fluid (VOF) method, phase-field methods and the level-set method, in which the marker function is directly advected. The reader is referred to Hirt and Nichols (1981), Puckett

et al. (1997) and Badalassi, Ceniceros and Banerjee (2003) for more details on these methods.

There are a number of studies using such methods for heat and mass transfer problems. Most of these studies are limited to two-dimensional or axisymmetric cases. Examples of such studies are, the work of Gibou et al. (2007) applying a level set sharp interface method for multiphase flow with phase change, Tanguy, Ménard and Berlemont (2007) using a Level set method for vaporizing two-phase flows. Davidson and Rudman (2001) used the VOF method for heat and mass transfer in deforming interfaces. Flow with phase change have been studied by Welch and Wilson (2000), Jin and Shaw (2010) and Banerjee (2013) applying the VOF method.

There have been also studies on heat and mass transfer in droplets in 3D but they are mostly limited to the case of a single droplet. The study of Gilmanov and Acharya (2008) on heat transfer and flow past deformable objects and Hase and Weigand (2004) on heat transfer from a single deforming droplet by VOF are such examples.

Al-Sharafi, Yilbas and Ali (2017) have studied the effect of droplet size on droplet thermal characteristic on micro-post arrays which are created via lithography on a silicon wafer. Che et al. (2015) have shown the effect of the flow inside of droplets on heat transfer in droplet-based microchannel heat sinks using the finite volume method and the level-set methods. To our knowledge, although there are extensive numerical and experimental studies focused on hydrodynamics of binary collision of droplets in the literature, such as Pan and Suga (2005), Mohammadi, Shahhosseini and Bayat (2012), Nikolopoulos et al. (2012) and Kwakkel, Breugem and Boersma (2013), Hu et al. (2017) Sun et al. (2018), the study of heat transfer in colliding droplets has not been studied in detail.

1.3 Objective

The objective of this work is to develop a numerical model for multiple droplets colliding, deforming with thermal interaction with the ambient flow. A coupled level set and volume of fluid method is applied to capture the interfaces in the computational domain while conserving mass and volume. The code is equipped with a coalescence and break up module that can prevent numerical coalescence of droplets when they are in the vicinity of each other and not colliding.

1.4 Outline

The content of the following chapters are as follows. In Chapter 2 the governing equations, the numerical solutions for the governing equations of multiphase flow, the spatial and temporal discretization, the interface description and advection are presented. The fast pressure and momentum solver is also introduced in this chapter. Chapter 3 is focused on the heat transfer from a single solid sphere. The effect of considering internal temperature distribution inside the solid sphere on the Nusselt number is studied and the results are compared with the case of isothermal solid sphere. In Chapter 4 the case of heat transfer from a single deforming droplet is studied for different Reynolds numbers and Weber numbers. Heat transfer from colliding droplets for different Reynolds numbers, Weber numbers and eccentricities of droplets with an iterative solver and a direct solver is studied in Chapter 5. The conclusions and recommendations for future work are given in Chapter 6.

2 Governing equations and the numerical method

In this chapter the governing equations and the numerical solution are presented. The non-dimensional numbers such as the Weber number and the Reynolds number are introduced and the non-dimensional forms of the governing equations which are obtained by using these numbers are also discussed. The Coupled Level-Set and Volume of Fluid method (CLSVOF) for solving problems with large topological changes is introduced and the numerical schemes which are applied for the advection and diffusion terms are presented. At the end of this chapter the fast pressure and momentum solver are discussed which have been implemented to decrease the computational cost and to improve the numerical convergence.

2.1   Governing equations for multiphase flows

In this work one set of equations is used for the whole domain while the fluid properties can change moving from one fluid to another. Since the magnitude of the velocity in this study is much smaller than the speed of sound. Thus, the Mach number which is the ratio of the fluid velocity and the speed of sound is much smaller than one. Therefore, the flow can be assumed incompressible, with different viscosities and densities. Since there are no chemical reactions involved viscosity and density remain constant in each phase. The mass continuity equation can be written as, Tryggvason et al. (2006),

$$\frac{\partial \rho}{\partial t} + \nabla \cdot \left(\rho \mathbf{u} \right) = 0 \tag{2.1}$$

In which $\mathbf{u}$, is the velocity, ρ is the density and ∇ is the divergence operator. The density is assumed to be constant therefore, equation (2.1) can be reduced to:

$$\nabla \cdot \mathbf{u} = 0 \tag{2.2}$$

The momentum equation holds at every point in the domain, Tryggvason et al. (2006),

$$\frac{\partial \rho \mathbf{u}}{\partial t} + \nabla \cdot \left(\rho \mathbf{u}\mathbf{u} \right) = -\nabla p + \nabla \cdot \left(\mu \left(\nabla \mathbf{u} + \nabla \mathbf{u}^T \right) \right) + \rho g \tag{2.3}$$

In which μ is the dynamic viscosity, p is the pressure and g is the gravity force. With the help of equation(2.1), (2.3) can be written as,

$$\frac{\partial \mathbf{u}}{\partial t} + \nabla \cdot \left(\mathbf{u}\mathbf{u} \right) = -\frac{1}{\rho} \nabla p + \frac{1}{\rho} \nabla \cdot \left(\mu \left(\nabla \mathbf{u} + \nabla \mathbf{u}^T \right) \right) + g \tag{2.4}$$

The conservation of energy equation from Bird, Stewart and Lightfoot (2007) for an incompressible flow is,

$$\frac{\partial \left(\rho C_p T \right)}{\partial t} + \nabla \cdot \left(\rho C_p \mathbf{u} T \right) = \nabla \cdot \left(k \nabla T \right) \tag{2.5}$$

In which C_p is the heat capacity, T is the temperature and k is thermal conductivity of the fluid. In this study the variation of the heat capacity with temperature is assumed to be negligible. Since C_p remains constant in each phase the energy equation can be rewritten as,

$$\frac{\partial T}{\partial t} + \nabla \cdot (\mathbf{u}T) = \frac{1}{\rho C_p} \nabla \cdot (k \nabla T) \tag{2.6}$$

The governing equations are made non-dimensional with the help of the characteristic length scale D_0, for instance the droplet diameter, velocity scale U_0, which is the relative velocity of droplets in case of colliding droplets and the inlet velocity in case of a single falling droplet, density ρ_g, viscosity μ_g, thermal conductivity k_g and specific heat capacity at constant pressure C_{pg} of the carrier phase. T_s and T_∞ are respectively the initial droplet temperature and the far field ambient flow temperature. This results in the definition of the following non-dimensional variables:

$$x' = \frac{x}{D_0}, \mathbf{u}' = \frac{\mathbf{u}}{U_0}, t' = \frac{t}{D_0/U_0}, \rho' = \frac{\rho}{\rho_g}, \mu' = \frac{\mu}{\mu_g}, p' = \frac{p}{\rho_g U_0^2}, C_p' = \frac{C_p}{C_{pg}}, k' = \frac{k}{k_g}, T' = \frac{T - T_\infty}{T_s - T_\infty}$$

By introducing these variables in the equations and dropping the primes, the non-dimensional form of the governing equations are obtained:

$$\nabla \cdot \mathbf{u} = 0 \tag{2.7}$$

$$\frac{\partial \mathbf{u}}{\partial t} + \nabla \cdot (\mathbf{u}\mathbf{u}) = -\frac{1}{\rho} \nabla p + \frac{1}{\rho Re} \nabla \cdot \left(\mu \left(\nabla \mathbf{u} + \nabla \mathbf{u}^T \right) \right) + \frac{1}{Fr} z \tag{2.8}$$

$$\frac{\partial T}{\partial t} + \nabla \cdot (\mathbf{u}T) = \frac{1}{\rho C_p RePr} \nabla \cdot (k \nabla T) \tag{2.9}$$

These equations are valid in each phase but special treatment is required at the interface which is discussed in section 2.2. The dimensionless parameters in equations (2.7)-(2.9) are the Reynolds number, Froude number and Prandtl number which are respectively defined as:

$$Re = \frac{\rho_g U_0 D_0}{\mu_g}, Fr = \frac{U_0^2}{gD_0}, Pr = \frac{C_{p_g} \mu_g}{k_g} \tag{2.10}$$

2.2   Interface conditions

In numerical simulation of multiphase flow the usual governing equations are solved, but in order to couple the equations of different phases the jump conditions at the interface have to be exerted. The jump conditions are obtained from the continuity of velocity, stresses and heat flux across the interface. The normal velocity should be continuous across the interface, Tryggvason, Scardovelli and Zaleski (2011), Tryggvason et al. (2006), which can be written as,

$$V = \mathbf{u}_1 \cdot \mathbf{n} = \mathbf{u}_2 \cdot \mathbf{n} \tag{2.11}$$

In which V in the interface velocity and $\mathbf{n}$ is the normal to the interface. $\mathbf{u_1}$ and $\mathbf{u_2}$ are fluid velocity vectors at the interface for each phase as shown in Figure 2.1.

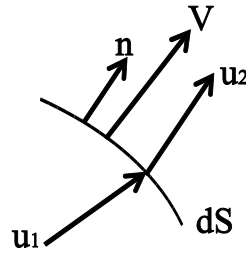**Figure 2.1 An infinitesimal interface dS, showing the normal to the interface n, the interface velocity V, inside and outside velocities u_1 and u_2 respectively.**

Since for viscous fluids the no-slip boundary condition should hold for the tangential velocity at the interface, the interface condition for the velocity vector can be written as,

$$[\mathbf{u}]_\Gamma = 0 \tag{2.12}$$

Where $[.]_\Gamma$ is the jump notation, i.e. $[x]_\Gamma = x_2 - x_1$. $[\mathbf{u}]_\Gamma = 0$ implies that there is no jump in the velocity at the interface.

Figure 2.3 shows the forces acting on the interface for a stationary case. When there is fluid motion, the stresses induced by the velocity should also be considered. Since the conservation of momentum should hold at the interface, and the interface is assumed to move with the fluid velocity. The jump condition for stresses at the interface can be written as,

$$\left[p\mathbf{n} + \mu \left(\nabla \mathbf{u} + \nabla \mathbf{u}^T \right) \cdot \mathbf{n} \right]_\Gamma = \sigma \kappa \mathbf{n} \tag{2.13}$$

In which $\mathbf{n}$ denotes the interface normal vector, κ is the magnitude of the interface curvature and σ is the surface tension coefficient which is assumed to be constant. It should be noted that the pressure and velocity jump conditions are coupled.

Kang, Fedkiw and Liu (2000) proposed to regularize the viscosity across the interface. In that case the velocity gradients become continuous across the interface. Sussman and Puckett (2000) and Chang et al. (1996) have proposed the following smoothed Heaviside function to regularize the viscosity:

$$H(\phi) = \begin{cases} 0 & \text{if } \phi < -\alpha \\ \frac{1}{2}\left(1 + \left(\frac{\phi}{\alpha} \right) + \frac{1}{\pi} sin\left(\frac{\pi\phi}{\alpha} \right) \right) & \text{if } |\phi| \leq \alpha \\ 1 & \text{if } \phi > \alpha \end{cases} \tag{2.14}$$

Where $\alpha = 3/2h$ and h is the uniform mesh width. The Heaviside function of $H(\phi)$ for a uniform mesh width of 0.05 is shown in Figure 2.2.
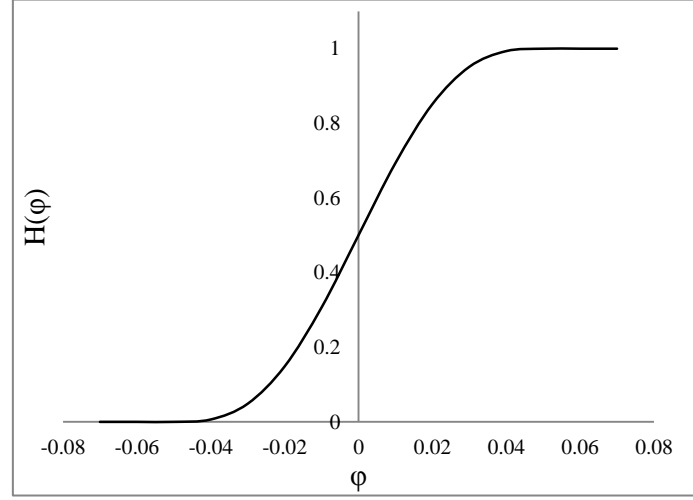
Figure 2.2 The relation between H (φ) and φ for a uniform mesh width of 0.05.

Then the viscosity can be regularized as follows:

$$\mu = \mu_g \left(1 - H\left(\phi\right)\right) + \mu_l H\left(\phi\right) \qquad (2.15)$$

By using the regularized viscosity across the interface, the gradient of velocities are also continuous across the interface and equation (2.13) can be reduced to:

$$\left[p\mathbf{n}\right]_\Gamma = \sigma\kappa\mathbf{n} \qquad (2.16)$$

With this reduction the jump conditions for the pressure and velocity are decoupled, and there is only a pressure jump at the interface due to the surface tension force. It means the same numerical scheme can be used in the whole domain to discretize the derivatives of the velocity.
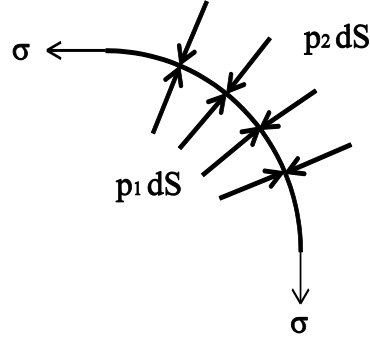
Figure 2.3 Forces acting on an interface for stationary fluids with a surface tension of σ.

When there is no phase change due to evaporation or condensation and there is thus no latent heat production, the heat flux q should also be continuous across the interface. Therefore the jump condition for heat flux can be written as,

$$[k\nabla T]_\Gamma = 0 \tag{2.17}$$

Inserting the dimensionless variables in jump condition equations, the scaled form of the jump conditions are obtained,

$$[\mathbf{u}]_\Gamma = 0 \tag{2.18}$$

$$[p\mathbf{n}]_\Gamma = \frac{1}{We}\kappa\mathbf{n} \tag{2.19}$$

$$[k\nabla T]_\Gamma = 0 \tag{2.20}$$

The dimensionless Weber number in equation (2.19) is defined as,

$$We = \frac{\rho_g D_0 U_0^2}{\sigma} \tag{2.21}$$

The other scalar properties, the thermophysical properties and the temperature are also smoothed across the interface and are defined as:

$$\rho = \rho_g \left(1 - H\left(\phi\right)\right) + \rho_l H\left(\phi\right) \tag{2.22}$$

$$C_p = C_{p_g} \left(1 - H\left(\phi\right)\right) + C_{p_l} H\left(\phi\right) \tag{2.23}$$

$$k = k_g \left(1 - H\left(\phi\right)\right) + k_l H\left(\phi\right) \tag{2.24}$$

$$T = T_g \left(1 - H\left(\phi\right)\right) + T_l H\left(\phi\right) \tag{2.25}$$

The dimensionless thermophysical properties and the temperature used in the non-dimensional Navier-Stokes equations, the energy equation and the interface conditions are defined by:

$$\mu = 1 + \left(\frac{\mu_l}{\mu_g} - 1\right) H\left(\phi\right) \tag{2.26}$$

$$\rho = 1 + \left(\frac{\rho_l}{\rho_g} - 1\right) H\left(\phi\right) \tag{2.27}$$

$$C_p = 1 + \left(\frac{C_{p_l}}{C_{p_g}} - 1\right) H\left(\phi\right) \tag{2.28}$$

$$k = 1 + \left(\frac{k_l}{k_g} - 1\right) H\left(\phi\right) \tag{2.29}$$

$$T = 1 + \left(\frac{T_l - T_\infty}{T_g - T_\infty} - 1\right) H\left(\phi\right) \tag{2.30}$$

2.3 Computational methods for multiphase flows

A major challenge in solving the governing equations in multiphase flows is to capture the whole range of length and time scales to deliver a solution with acceptable accuracy. The large scales are droplet, bubbles or wakes and small scales can refer to the filament between two bouncing droplets. In colliding and deforming droplets where they can break-up or coalesce, smaller scales become more important. Therefore, the applied numerical methods should necessarily capture these small scales accurately. There are different methods for solving multi-phase problems, these methods can be categorized as, the Two-Fluid approach as in Ishii and Mishima (1984), the Discrete Bubble method as in Jain et al. (2013) and direct methods for two-phase flow. In the first two methods, a simplified description of the physics is used and the equations are solved with less computational effort. These methods are applicable for large scale industrial flows, such as the work of Portela and Oliemans (2006) in which they have studied and compared different approaches for multiphase flow simulations in industrial applications. In these methods additional terms, known as closure terms, are used to represent the interaction between phases. Since simplified description of the physics is used, small scales are not captured accurately. Therefore, the accuracy of the model depends on the definition of the closure terms which can add extra complexity to the problem. On the other hand in direct methods, a detailed representation of interfaces is used and the Navier-Stokes equations are solved without the need of the closure terms. The study of Irfan and Muradoglu (2017) on evaporation in a multiphase system and the study of Eisenschmidt et al. (2016) on direct numerical simulation of multiphase flows give a good overview of these methods. Besides the complexity of the programming, a major obstacle in performing direct methods is the computational effort. However, the latter can be overcome with the improvements in computing power.

2.4 Interface handling in direct methods

The problem of locating the interface in the domain can be handled by different meshing methods. One way is to define the mesh such that the interface always sticks to a specific layer of cells, in such methods the 3D grid spacing and locations has to deform in time. One technique is adding grid points by splitting a regular structured grid locally. To increase the resolution small cells can be split further. This is called the adaptive mesh refinement (AMR). The work by Kadioglu and Sussman (2008) for

underwater explosions and implosions and the simulation of rising bubbles by Hua and Lou (2007) on adaptive mesh are examples of such studies. Other techniques such as moving mesh or variable grid spacing can also be used. In these methods the whole domain or a part of it has to be re-meshed every time step which makes them not only computationally expensive but also complex from an implementation point of view and therefore not suitable for complicated problems. Examples of moving mesh and adaptive mesh are shown in Figure 2.4 and Figure 2.5. In order to eliminate the re-meshing step, a fixed grid can be used.

In this study a marker function or marker particles are required to describe the interface. Every time step these marker functions or marker particles have to be updated when the interfaces are moving and deforming. There are some popular ways to describe the interface in multiphase problems. These methods are categorized based on implicit or explicit description of the interface which will be discussed in more detail in sections 2.4.1 and 2.4.2.
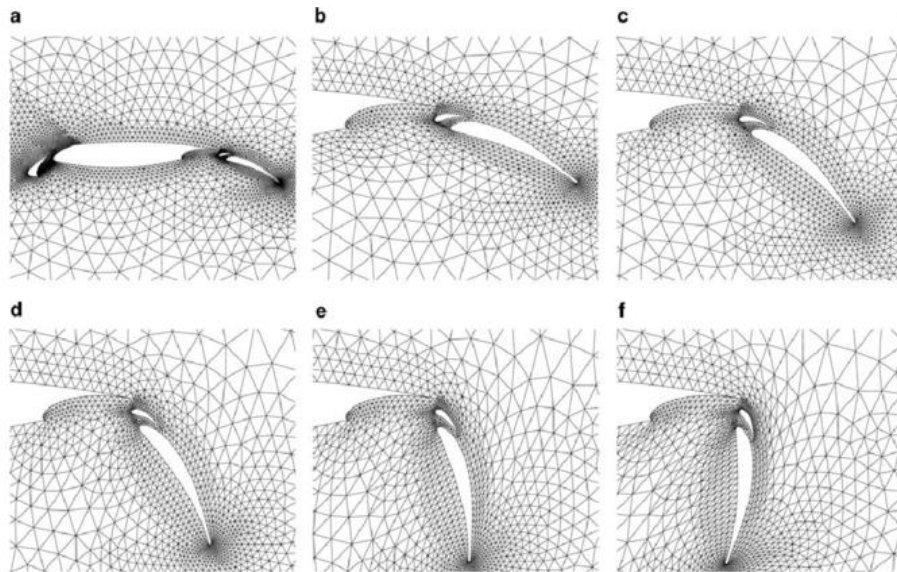

**Figure 2.4 Moving mesh arounf main foil and flaps.
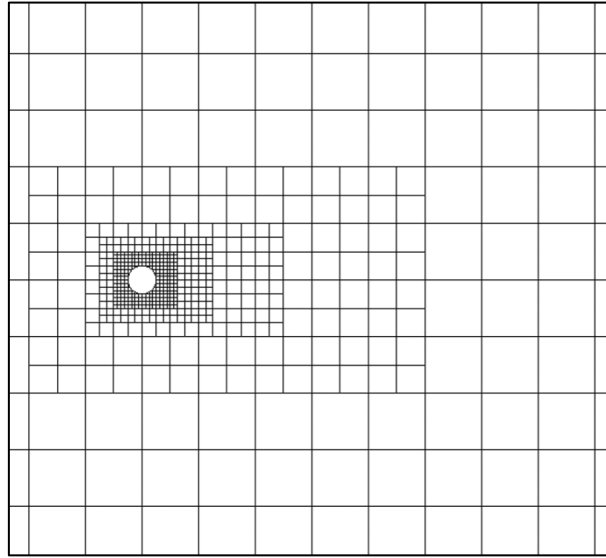Image source: Qin, Liu and Xia (2005)**

Figure 2.5 Adaptive mesh refinement.
Image source: Vanella, Posa and Balaras (2014)

2.4.1 Front-tracking methods

In front-tracking methods an explicit description of the interface is used. In front-tracking methods the interface is identified by connected marker points as shown in Figure 2.6. The marker points are advected by the velocity from the Eulerian grid. In general a triangular unstructured grid is used to represent the interface, in this way grid points can be added or removed in a straightforward way as in Unverdi and Tryggvason (1992) for viscous, incompressible, multi-fluid flows. In their study the unstructured grid moves through the stationary grid while the interface deforms. Therefore the grid should be restructured during the solution.

The different front-tracking methods are distinguished by the way the marker points interact with the fixed grid. One simple approach is to consider the front as a smooth transition between the different fluids.

There are different methods to keep the interface sharp. One way is to modify the numerical approximations near the front by the front-tracking method as in Glimm and McBryan (1985), in which the field variables at the interface are extrapolated to grid points on the other side of the front, allowing the use of finite-difference discretization for grid points next to the interface. Another way is to modify the fixed grid near the interface such that the grid lines coincide with the interface.

One disadvantage of the front-tracking method is that the advection of the marker particles is not necessarily mass conserving. This error can be controlled by adjusting the numerical properties (order) of the advection scheme. Another error is caused by the interpolation of velocities which might not necessarily be divergence-free. Furthermore it should be noted that in the front-tracking methods the changes in topology are not handled automatically.
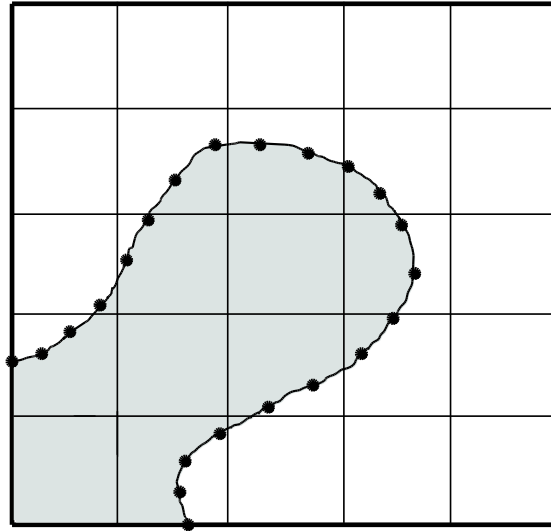
Figure 2.6 Connected marker particles in front-tracking method. Figure adapted from Tryggvason, Scardovelli et al. (2011).

2.4.2 Front-capturing methods

In front-capturing methods an implicit description of the interface is used. The interface can be described by a marker function. This marker function can be the mass or volume fraction inside a computational cell, which is *1* if the cell is completely filled with the fluid, *0* if the cell is empty and a value between *0* and *1* if the cell is partially filled. In this way the interface is defined with a sharp change from on phase to the other. The interface can also be determined by a smooth function *F*, which takes the value of *0* at the interface, *F>0* in one phase and *F<0* in the other phase (this is the basis of the level-set method).

In front-capturing methods such as the phase-field method, the CIP (cubic interpolated pseudo-particle or constrained interpolation profile) method, the level-set method and the Volume-of-fluid method the marker function is directly advected.

Phase-field method

In the phase-field method by modifying the governing equations, the interface remains sharp. Updating the phase function is done by adding a nonlinear diffusion term to the advection equation, Tryggvason et al. (2011). The diffusive term prevents extreme changes in the thickness of the interface and therefore keeps it finite. The Navier-Stokes equations are also modified by adding a term which results in surface tension forces in the interface region. The phase-field method is mainly used for solidification problems; it is also suitable for small scale problems and multiphase problems. This method is used in the study of Chiu and Lin (2011) for incompressible two-phase flows and in a later study for topology optimization by Jeong et al. (2014). The phase field method is comparable to other methods using a fixed grid. The smoothing of the interface and using the front-capturing makes this method similar to the level-set method. The advantage of the phase-field method over tracking methods that start from sharp interfaces is that it can be used for small-scale phenomena.

CIP method

In the CIP method the advection equations are solved for both a marker function and its derivatives. By fitting a cubic polynomial to the nodal values of the marker function and its derivatives the dispersive error is reduced. In the study of Che Sidik and Niaki Attarzadeh (2012) this method is used for transient hydrodynamics of solid spheres. Matsumoto (2015) has used the CIP method for two-dimensional single-phase hydrothermal reservoir simulations. Although the CIP method was not originally invented for discontinuous solutions yet due to very low dispersive errors it performs well for such problems but still some oscillations occur.

Volume of fluid method

In the volume of fluid method the marker function is defined as a volume fraction of a computational cell of the reference phase as shown in Figure 2.7. The interface is implicitly identified by the volume of fluid in each cell. The interface is reconstructed according to the velocities and the volume of fluid in each cell. The method of reconstruction of the interface determines the accuracy of the scheme. In general a VOF method consists of two steps, reconstruction of the interface and advection of the reconstructed interface. Falcão, Pereira and Pinto (2016) have used this method to model the two-phase flow phenomena in low temperature fuel cells.

Interface advection

To advect an interface accurately special techniques should be used. In the simple line interface calculation (SLIC) by Noh and Woodward (1976) the marker function is advected by time splitting. Therefore, in a two-dimensional problem the marker function is first advected in one direction and then the other. In the method proposed by Hirt and Nichols (1981) the interface is approximated by straight lines. Using the values of the marker function in the neighboring cells, the normal to the interface and consequently the orientation of the interface can be found. In these methods the interface is distorted and pieces of interface which break away in an unphysical way can be generated.

In order to have a more accurate advection scheme it is important to reconstruct the interface in each cell by using the volume of fluid in that cell and its neighbors. This has been considered in the piecewise linear interface calculation (PLIC) method. In this method the interface is approximated by a straight- line segment in each cell using the normal to the interface to determine the orientation of the line. The normal is obtained by considering the volume of fluid in the cell and its neighbors. After construction of the interface in each cell, the fluxes between cells are computed. Since the accuracy of the advection is influenced by the accuracy of the interface reconstruction, it has become an important task to find the normal accurately in PLIC methods. In Figure 2.8, the VOF reconstruction of the solution in two dimensions using different reconstruction methods is shown. It is observed that the PLIC method is more accurate in reconstructing the interface.
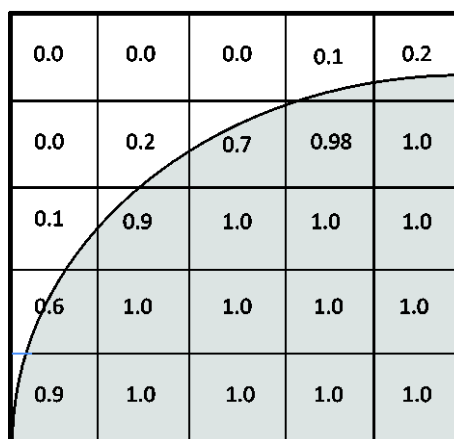

Figure 2.7 Representation of the volume-of-fluid method.

The advantage of the VOF method lies in the fact that the volume fraction of each phase is known in each cell at every time step and it is therefore easy to obtain the amount of mass. However, capturing the interface depends on the accuracy of the reconstruction of the interface.

Level-set method

In the level-set method the different fluids or phases are identified by a smooth marker function as a distance function to the interface, which takes positive values in one fluid and negative values in the other. The interface is then identified by the zero value level-set; this is shown in Figure 2.9. Furthermore, for convenience the gradient of the level-set is, $|\nabla(\phi) = 1|$. In this way the distance to the interface is always known. The interface motion depends only on the normal velocity component. Since the level-set function is smooth, in principle it can be advected using any standard method for hyperbolic equations.

The advection of the LS function results in a non-volume conserving representation of the interface. Therefore, a reinitialization of the LS function $\varphi^{n+1/2}$ is required to keep it as a distance function to the advected VOF function $\psi^{n+1/2}$. The reinitialization of the corrected LS function is performed with a reconstruction distance function (RDF) using fast marching method (FMM) over a few grid cells (at least 4) to ensure $|\nabla(\phi) = 1|$. For the reinitialization first in the cells which contain the interface a piecewise linear reconstruction of the interface is performed. The normal vector is obtained from the updated LS function while the intercept of the linear segment is obtained from the updated VOF function. The for more detail of the reinitialization procedure the reader is referred to Coyajee and Boersma (2009).

The level-set method has the advantage of simplicity comparing to the VOF method in which the interface reconstruction is required and the front-tracking methods which need addition or removal of marker points. Disadvantage of the level-set method is that it is not mass conserving and its accuracy depends on the order of accuracy of the advection scheme.
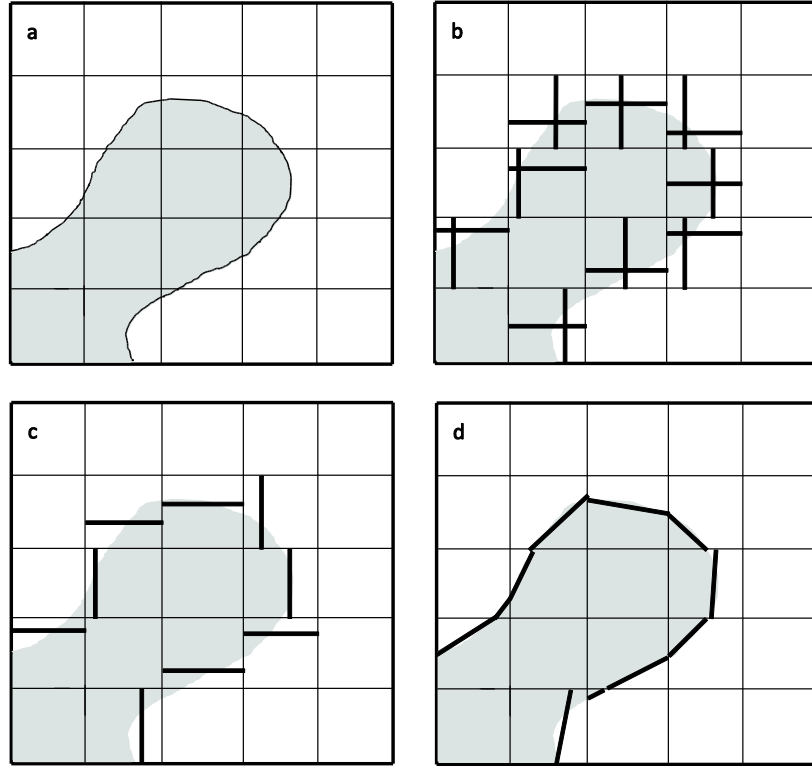
Figure 2.8 VOF reconstruction of interface. (a)The original interface. (b)SLIC reconstruction. (c)The Hirt and Nichols (1981) reconstruction. (d)PLIC reconstruction. Figure adapted from Tryggvason, Scardovelli et al. (2011).

2.4.3   Coupled level-set and volume-of-fluid method

In this study a coupled level-set and volume-of-fluid (CLSVOF) method is used. As it was mentioned before, the advection of the level-set function is not mass (or volume) conserving. However, it is a very elegant method in locating the interface since the calculation of the interface curvature and its normal are straightforward because of the mathematical definition of the level-set function. On the other hand the volume of fluid method is mass conserving but requires reconstruction of the interface and also calculating the normal to the interface is more complicated than in the level-set method. In order to benefit from the advantages of both methods, in this work a coupled level-set and volume-of-fluid method is used for the representation and advection of the interface.

Figure 2.9 Representation of the level-set method. ϕ represents the level-set function; the interface is indicated by the zero level-set.

2.5 Time and spatial discretization of the governing equations

For the discretization of equations (2.7)-(2.9) a staggered grid is used such that the velocity components are placed at faces of the cells and the scalars such as temperature, pressure, level set and volume of fluid denoted as T, P, ϕ and ψ are respectively located at the center of each cell. A schematic of a staggered grid is shown in Figure 2.10.

Figure 2.10 Standard 2D MAC mesh. Vector properties are calculated at faces of the cells and scalar properties are calculated at the cell center.

For an incompressible flow, usually a pressure correction method is used, in which the pressure is modified to guarantee a divergence free velocity field at the end of each time step. In this method, fir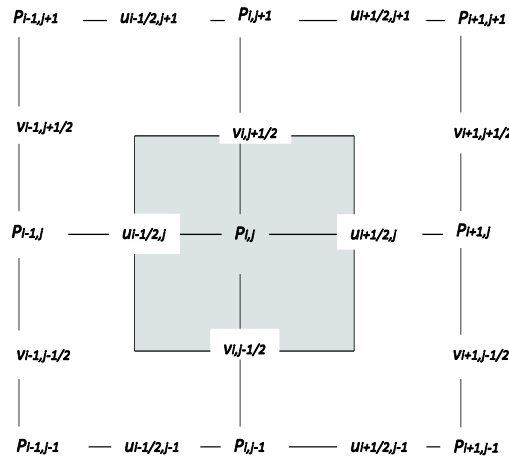st a velocity field which is generally not divergence free is calculated. The velocity is then corrected by adding the correct pressure gradient. The non-dimensional momentum equation (2.8) is split into a predictor and a corrector step. The prediction step reads:

$$\frac{u^* - u^n}{\Delta t} = -\left(\frac{3}{2} A\left(u^n\right) - \frac{1}{2} A\left(u^{n-1}\right)\right) +$$
$$\frac{1}{\rho^{n+\frac{1}{2}}} \left(\frac{1}{Re} D_{imp}\left(u^*\right) + \frac{1}{Re} D_{exp}\left(u^n\right) - Gp^{n-\frac{1}{2}}\right) + \frac{1}{Fr} z \tag{2.31}$$

In which A and D are numerical approximations for the advection and diffusion terms respectively. G is the numerical approximation of gradient. The advection terms are explicitly integrated by a second-order Adams-Bashforth method, i.e. the factors 3/2 and 1/2. The diffusive terms are split into an implicit and an explicit part which results in three separate linear systems for each predicted velocity component, Coyajee and Boersma (2009). These systems are solved with an incomplete Choleski preconditioned conjugate gradient (ICCG) solver. In the correction step the velocity field is corrected by adding the pressure gradient:

$$\frac{u^{n+1} - u^*}{\Delta t} = -\frac{Gp^*}{\rho} \tag{2.32}$$

In which:

$$p^* = p^{n+\frac{1}{2}} - p^{n-\frac{1}{2}} \tag{2.33}$$

The velocity at the new time level should be divergence free:

$$DIV\left(u^{n+1}\right) = 0 \tag{2.34}$$

In which *DIV* is the discrete divergence operator. Taking the divergence of the corrector equation (2.32) and applying(2.34), the Poisson equation for pressure is obtained:

$$DIV\left(\frac{1}{\rho^{n+\frac{1}{2}}}Gp^*\right) = \frac{1}{\Delta t}DIV\left(u^*\right) \qquad (2.35)$$

The thermodynamic properties in equations (2.31) and (2.35) are obtained based on the interface position at time level of *n+1/2* and *n-1/2*. Due to the definition of p^*, the Poisson equation for p^* is not separable and is therefore solved with an ICCG method. Then by substituting u^* and p^* in equation (2.32), u^{n+1} is obtained. At the end of this chapter we will discuss a new approach to make the Poisson equation separable.

Since the regularized viscosity is used, the velocity gradients are continuous at the interface. Therefore, derivatives of the velocity can be easily approximated by central second order finite difference methods. However, there will be a pressure jump at the interface which is treated by using the Level-Set function to locate the interface. The one-dimensional pressure gradient near an interface can be written as:

$$\left(\frac{\partial p^*}{\partial x}\right)_{i+1/2} = \frac{p^*_{i+1} - p^*_i - \left[p^*\right]}{\Delta x} \qquad (2.36)$$

Taking equation (2.19) into account, the pressure gradient at the cell face (*i+1/2*) can be written as:

$$\left(\frac{\partial p^*}{\partial x}\right)_{i+1/2} = \begin{cases} \dfrac{p^*_{i+1} - p^*_i - \kappa_\Gamma/We}{\Delta x} & if\,\phi_i \le 0 \quad and\,\phi_{i+1} > 0, \\[2ex] \dfrac{p^*_{i+1} - p^*_i + \kappa_\Gamma/We}{\Delta x} & f\,\phi_i > 0 \quad and\,\phi_{i+1} \le 0, \\[2ex] \dfrac{p^*_{i+1} - p^*_i}{\Delta x} & otherwise. \end{cases} \qquad (2.37)$$

The Poisson problem should be solved to obtain p* from equation(2.35). For a one-dimensional case the discretization of equation (2.35) at x_i is written as:

$$\left(\frac{1}{\rho_{i+1/2}} \frac{p_{i+1}^* - p_i^* - \left[p^* \right]}{\Delta x} - \frac{1}{\rho_{i-1/2}} \frac{p_i^* - p_{i-1}^*}{\Delta x} \right) \Bigg/ \Delta x = \frac{1}{\Delta t} \frac{u_{i+1/2}^* - u_{i-1/2}^*}{\Delta x} \tag{2.38}$$

Which can also be written as:

$$\left(\frac{1}{\rho_{i+1/2}} \frac{p_{i+1}^* - p_i^*}{\Delta x} - \frac{1}{\rho_{i-1/2}} \frac{p_i^* - p_{i-1}^*}{\Delta x} \right) \Bigg/ \Delta x = \frac{1}{\Delta t} \frac{u_{i+1/2}^* - u_{i-1/2}^*}{\Delta x} + \frac{1}{\rho_{i+1/2}} \frac{\left[p^* \right]}{\Delta x^2} \tag{2.39}$$

As it is seen in equation (2.39), the jump condition for pressure appears as a source term on the right hand side of the discrete Poisson problem. Therefore, (2.39) can be solved with a fast iterative method. The relevant matrix of the linear system of this equation is symmetric which is suitable for a conjugate gradient method.

Using the Continuous Surface Force (CSF) by Brackbill, Kothe and Zemach (1992), the jump condition can be included in the discretization as follows:

$$\left(\frac{\partial p}{\partial x} \right)_{i+1/2} = \frac{p_{i+1} - p_i}{\Delta x} - \frac{\kappa_\Gamma}{We} \frac{H(\phi_{i+1}) - H(\phi_i)}{\Delta x} \tag{2.40}$$

Using the smoothed Heaviside function (2.14), the pressure gradient can be written as:

$$\left(\frac{\partial p}{\partial x} \right)_{i+1/2} = \frac{p_{i+1} - p_i}{\Delta x} - \frac{\kappa_\Gamma}{We} \frac{H_\alpha(\phi_{i+1}) - H_\alpha(\phi_i)}{\Delta x} \tag{2.41}$$

To obtain values of $1/\rho$ at the cell face near the interface, the weighted average is used:

$$\frac{1}{\rho_{i+\frac{1}{2}}} = \frac{1}{\rho_i \theta + \rho_{i+1}(1-\theta)} \tag{2.42}$$

In which $\rho_i = \rho(\phi_i)$ and θ is:

$$\theta = \frac{|\phi_i|}{|\phi_i| + |\phi_{i+1}|} \tag{2.43}$$

2.6   Discritization of the energy equation

The energy equation can be discretized as:

$$\frac{T^{n+1} - T^n}{\Delta t} = -\left(\frac{3}{2} A(T^n) - \frac{1}{2} A(T^{n-1})\right) +$$

$$\frac{1}{\rho^{n+\frac{1}{2}} C_p^{n+\frac{1}{2}} RePr} \left(\frac{3}{2} D(T^n) - \frac{1}{2} D(T^n)\right) \tag{2.44}$$

The advective and diffusive terms are integrated using the second order Adams-Bashforth method. The corresponding velocity time level and the updated interface at n+1/2 are applied. The thermodynamic properties are obtained from the interface position and therefore are at n+1/2 time level.

Since there are sharp variation of the gradients across the interface Koren's flux limiter as in Waterson and Deconinck (2007) is used for the advection terms of the energy equation. Whit this scheme the solution is kept monotonic:

$$A(T_{i,j,k}) = -\left(\frac{Fu_{i,j,k} - Fu_{i-1,j,k}}{\Delta x} + \frac{Fv_{i,j,k} - Fv_{i,j-1,k}}{\Delta y} + \frac{Fw_{i,j,k} - Fw_{i,j,k-1}}{\Delta z}\right) \tag{2.45}$$

In which,

$$Fu_{i,j,k} = Su_{i,j,k}u_{i,j,k} \tag{2.46}$$

$$Fv_{i,j,k} = Sv_{i,j,k}v_{i,j,k} \tag{2.47}$$

$$Fw_{i,j,k} = Sw_{i,j,k}w_{i,j,k} \tag{2.48}$$

Depending on the velocity direction in the computational cell under consideration, *Su*, *Sv* and *Sw* are calculated differently. As an example the calculation of *Su* is presented:

If $u_{i,j,k} \geq 0$,

$$Su_{i,j,k} = T_{i,j,k} + 0.5\Phi_1\left(T_{i,j,k} - T_{i-1,j,k}\right) \tag{2.49}$$

In which,

$$\Phi_1 = \max\left(0, \min\left(2r_1, 1/3\left(1 + 2r_1\right), 2\right)\right) \tag{2.50}$$

$$r_1 = \frac{T_{i+1,j,k} - T_{i,j,k}}{T_{i,j,k} - T_{i-1,j,k}} \tag{2.51}$$

If $u_{i,j,k} < 0$,

$$Su_{i,j,k} = T_{i+1,j,k} + 0.5\Phi_1\left(T_{i+1,j,k} - T_{i+2,j,k}\right) \tag{2.52}$$

In which Φ_1 is calculated by (2.38) and,

$$r_1 = \frac{T_{i+1,j,k} - T_{i,j,k}}{T_{i+2,j,k} - T_{i+1,j,k}} \tag{2.53}$$

Sv and *Sw* are calculated in the same way.

The diffusion terms of the energy equations are discretized by a second order central difference scheme as:

$$D(T_{i,j,k}) = \frac{k_{i+\frac{1}{2},j,k}\left.\frac{dT}{dx}\right|_{i+\frac{1}{2},j,k} - k_{i-\frac{1}{2},j,k}\left.\frac{dT}{dx}\right|_{i-\frac{1}{2},j,k}}{\Delta x} +$$

$$\frac{k_{i,j+\frac{1}{2},k}\left.\frac{dT}{dy}\right|_{i,j+\frac{1}{2},k} - k_{i,j-\frac{1}{2},k}\left.\frac{dT}{dy}\right|_{i,j-\frac{1}{2},k}}{\Delta y} + \frac{k_{i,j,k+\frac{1}{2}}\left.\frac{dT}{dz}\right|_{i,j,k+\frac{1}{2}} - k_{i,j,k-\frac{1}{2}}\left.\frac{dT}{dz}\right|_{i,j,k-\frac{1}{2}}}{\Delta z}$$

(2.54)

In which,

$$\left.\frac{dT}{dx}\right|_{i+\frac{1}{2},j,k} = \frac{T_{i+1,j,k} - T_{i,j,k}}{\Delta x}$$

(2.55)

$$\left.\frac{dT}{dx}\right|_{i-\frac{1}{2},j,k} = \frac{T_{i,j,k} - T_{i-1,j,k}}{\Delta x}$$

(2.56)

dT/dy and *dT/dz* are calculated the same way for the other directions. To calculate the thermal conductivity at a cell face, the weighted harmonic average is used:

$$k_{i+\frac{1}{2}} = k_i\theta + k_{i+1}\left(1-\theta\right)$$

(2.57)

In which θ is obtained by equation (2.43).

2.7 Interface description and advection by CLSVOF method

In moving boundary problems with topological changes proper locating of the interface is an important step in the computational approach. In this work the level-set method is used to describe the interface where a fixed grid is used for the whole domain. The level-set function is used to distinguish between different phases by taking different

values in each phase. Every time step this marker function has to be updated due to the movement of the interface.

As it was mentioned before, the advection of the level-set function is not mass (or volume) conserving. However, it is a very elegant method in locating the interface since the calculation of the interface curvature and its normal are straightforward because of the mathematical definition of the level-set function. On the other hand the volume of fluid method is mass conserving but requires reconstruction of the interface and also calculating the normal to the interface is more complicated than in the level-set method. In order to benefit from the advantages of both methods, in this work a coupled level-set and volume-of-fluid method is used for the representation and advection of the interface. The interface is described as:

$$\Gamma(t) = \left\{ \mathbf{x} \big| \phi(\mathbf{x},t) = 0 \right\} \tag{2.58}$$

In which ϕ is the level-set function, $\phi > 0$ inside the droplet and $\phi < 0$ outside the droplet. In the CLSVOF method the volume fraction in each computational cell is defined in terms of the level-set function:

$$\psi_{i,j,k}(t) = \frac{1}{\Delta x \Delta y \Delta z} \int_{\Omega_{i,j,k}} H(\phi(\mathbf{x},t)) d\mathbf{x} \tag{2.59}$$

In which Ω denotes the volume of a computational cell and H is the Heaviside function as in equation (2.14).

The conservation law for the volume fraction can be written as,

$$\frac{\partial}{\partial t} \int_v \psi \, dv = -\oint_A \left(\frac{1}{\Delta x \Delta y \Delta z} \int_\Omega H(\phi) d\mathbf{x} \right) \mathbf{u}.n \, dA \tag{2.60}$$

Where A is the surface and v is the volume. Using Gauss's theorem,

$$\oint_A \left(\frac{1}{\Delta x \Delta y \Delta z} \int_\Omega H(\phi)\mathrm{d}\mathbf{x} \right) \mathbf{u}.n\mathrm{d}A = \int_v \nabla.\left(\left(\frac{1}{\Delta x \Delta y \Delta z} \int_\Omega H(\phi)\mathrm{d}\mathbf{x} \right) \mathbf{u} \right) \mathrm{d}v \qquad (2.61)$$

Substituting equation (2.61) in (2.60) and using equation (2.59) and differentiating with respect to v, the conservation of the volume fraction is obtained as,

$$\frac{d\psi_{i,j,k}}{dt} + \nabla \cdot \left(\mathbf{u}\, \psi_{i,j,k} \right) = 0 \qquad (2.62)$$

Which can also be written as:

$$\psi_t + \nabla \cdot \left(\mathbf{u}\psi \right) = 0 \qquad (2.63)$$

The discrete volume fractions is defined as,

$$\psi_{i,j,k} = \frac{1}{\Delta x \Delta y \Delta z} \int_{\Omega_{i,j,k}} H(\phi^L(\mathbf{x}))\mathrm{d}\mathbf{x} \qquad (2.64)$$

In which ϕ^L is a linearized LS function around the center of the computational cell *(i,j,k)*:

$$\phi^L(\mathbf{x}) = \phi_{i,j,k} + \left(\mathbf{x} - \mathbf{x}_{i,j,k} \right) \cdot \nabla\phi\big|_{i,j,k} \qquad (2.65)$$

In the compact form equation (2.62) can be rewritten as,

$$\psi = f\left(\phi, \nabla\phi\right) \tag{2.66}$$

The conservation equation for the LS function is simply:

$$\frac{\partial \phi}{\partial t} + \nabla \cdot \left(\mathbf{u}\phi\right) = 0 \tag{2.67}$$

2.7.1 Advection of the LS and VOF functions:

Using u^n, $\varphi^{n-1/2}$ and $\psi^{n-1/2}$ the level-set and volume-of-fluid functions are advected separately using a second order operator split advection scheme proposed by Sussman and Puckett (2000). For a given scalar s the scheme works as follows.

$$\tilde{s}_{i,j,k} = \frac{s_{i,j,k}^n + \left(\Delta t/\Delta x\right)\left(G_{i-1/2,j,k} - G_{i+1/2,j,k}\right)}{1 - \left(\Delta t/\Delta x\right)\left(u_{i+1/2,j,k} - u_{i-1/2,j,k}\right)} \tag{2.68}$$

$$\hat{s}_{i,j,k} = \frac{\tilde{s}_{i,j,k} + \left(\Delta t/\Delta x\right)\left(\tilde{G}_{i,j-1/2,k} - \tilde{G}_{i,j+1/2,k}\right)}{1 - \left(\Delta t/\Delta x\right)\left(v_{i,j+1/2,k} - v_{i,j-1/2,k}\right)} \tag{2.69}$$

$$\overline{s}_{i,j,k} = \frac{\hat{s}_{i,j,k} + \left(\Delta t/\Delta x\right)\left(\hat{G}_{i,j,k-1/2} - \hat{G}_{i,j,k+1/2}\right)}{1 - \left(\Delta t/\Delta x\right)\left(w_{i,j,k+1/2} - w_{i,j,k-1/2}\right)} \tag{2.70}$$

$$s_{i,j,k}^{n+1} = \overline{s}_{i,j,k} - \Delta t \left(\begin{array}{l} \dfrac{\tilde{s}_{i,j,k}}{\Delta x}\left(u_{i+1/2,j,k} - u_{i-1/2,j,k}\right) + \\[2mm] \dfrac{\hat{s}_{i,j,k}}{\Delta y}\left(v_{i,j+1/2,k} - v_{i,j-1/2,k}\right) + \dfrac{\overline{s}_{i,j,k}}{\Delta z}\left(w_{i,j,k+1/2} + w_{i,j,k-1/2}\right) \end{array} \right) \tag{2.71}$$

In which,

$$G_{i+1/2,j,k} = s_{i+1/2,j,k} u_{i+1/2,j,k} \tag{2.72}$$

$$\tilde{G}_{i,j+1/2,k} = \tilde{s}_{i,j+1/2,k} v_{i,j+1/2,k} \tag{2.73}$$

$$\hat{G}_{i,j,k+1/2} = \hat{s}_{i,j,k+1/2} w_{i,j,k+1/2} \tag{2.74}$$

In order to keep the second order accuracy, the order of coordinate directions is changed every time step. If the scalar *s* represents the level-set function, depending on the direction of velocity, *s* is calculated differently,

If $u_{i+1/2,j,k} > 0$,

$$s_{i+1/2,j,k} = s_{i,j,k}^{n} + \frac{\Delta x}{2} \left(1 - u_{i+1/2,j,k} \frac{\Delta t}{\Delta x}\right) \frac{s_{i+1,j,k}^{n} - s_{i-1,j,k}^{n}}{2\Delta x} \tag{2.75}$$

If $u_{i+1/2,j,k} \leq 0$,

$$s_{i+1/2,j,k} = s_{i+1,j,k}^{n} - \frac{\Delta x}{2} \left(1 + u_{i+1/2,j,k} \frac{\Delta t}{\Delta x}\right) \frac{s_{i+2,j,k}^{n} - s_{i,j,k}^{n}}{2\Delta x} \tag{2.76}$$

The same procedure is used for other directions. Then the advected level-set function is corrected and reinitialized to satisfy the mass conservation.

When *s* represents the volume-of-fluid function, the discrete flux $s_{i+1/2,j,k}$ is computed from a geometric reconstruction of phases in each cell. Depending on the direction of velocity $s_{i+1/2,j,k}$ is calculated as,

If $u_{i+1/2,j,k} > 0$,

$$s_{i+1/2,j,k} = \frac{\int_{z_{i-1/2}}^{z_{i-1/2}} \int_{y_{i-1/2}}^{y_{i+1/2}} \int_{x_{i+1/2} - u_{i+1/2,j,k}\Delta t}^{x_{i+1/2}} H\left(\phi^{L}_{i,j,k}\right) dxdydz}{u_{i+1/2,j,k}\Delta t \Delta y \Delta z} \tag{2.77}$$

If $u_{i+1/2,j,k} \leq 0$,

$$s_{i+1/2,j,k} = \frac{\int_{z_{i-1/2}}^{z_{i-1/2}} \int_{y_{i-1/2}}^{y_{i+1/2}} \int_{x_{i+1/2}}^{x_{i+1/2}-u_{i+1/2,j,k}\Delta t} H\left(\phi^{L}_{i,j,k}\right) dxdydz}{\left|u_{i+1/2,j,k}\right| \Delta t \Delta y \Delta z} \tag{2.78}$$

In which ϕ^{L} represents the linear reconstruction of the interface,

$$\phi^{L}_{i,j,k} = \phi^{*}_{i,j,k} + \left(\mathbf{x}-\mathbf{x}_{i,j,k}\right)\cdot\nabla\phi^{*}\big|_{i,j,k} \tag{2.79}$$

The current level-set function is first computed according to the current Volume-of-fluid function. The level-set function is then updated in the considered direction by,

If $u_{i+1/2,j,k} > 0$,

$$\phi^{*} = \phi - \frac{1}{2}\left(1-u_{i+1/2,k}\right)n_{z} \tag{2.80}$$

If $u_{i+1/2,j,k} \leq 0$,

$$\phi^{*} = \phi + \frac{1}{2}\left(1+u_{i+1/2,k}\right)n_{z} \tag{2.81}$$

A piecewise linear reconstruction is performed in the cells carrying the interface. The normal to the reconstructed interface is obtained from the uncorrected LS function while the intercept of the linear reconstruction is determined by the VOF function. Since the level-set function is defined as a signed distance function to the interface, the mathematical property of this function is defined as,

$$\left|\nabla\phi\right| = 1 \tag{2.82}$$

2.7.2 Reinitialization of the LS function:

The advection of the LS function results in a non-volume conserving representation of the interface. Therefore, a reinitialization of the LS function $\varphi^{n+1/2}$ is required to keep it as a distance function to the advected VOF function $\psi^{n+1/2}$.

The reinitialization of the corrected LS function is performed with a reconstruction distance function (RDF) using fast marching method (FMM) over a few grid cells (at least 4) to ensure (2.82). For the reinitialization first in the cells which contain the interface a piecewise linear reconstruction of the interface is performed. The normal vector is obtained from the updated LS function while the intercept of the linear segment is obtained from the updated VOF function. The for more detail of the reinitialization procedure the reader is referred to Coyajee and Boersma (2009).

2.8 Coalescence/breakup model

When the droplets approach each other, depending on the momentum and the surface tension of droplets they can either, bounce or coalesce. The coalescence of droplets occurs when the surface distance of the droplets becomes of the order of 10 nm Oldenziel (2014). This is where the van der Waals force can come into account and could result in the rupture of the liquid film between the droplets, Oldenziel (2014). If the surface tension is high enough, the surface energy can be converted into kinetic energy and result in bouncing of droplets. The breakup of a droplet would occur if the velocity and pressure variations around or within the droplet are large with respect to the surface tension forces. The coalescence/breakup model of Kwakkel et al. (2013) is used in this work. This model is based on the film drainage model of Zhang and Law (2011) which predicts the result of a binary head-on collision of identical droplets as well as the drainage time and contact time of droplets.

2.9 Implementation of direct solvers

As it was mentioned in section 2.4 when using the pressure correction method to solve the Navier-Stokes equations, a Poisson equation for pressure, equation (2.83) should be solved every time step which is the most time consuming part in the pressure correction method

$$DIV\left(\frac{1}{\rho^{n+\frac{1}{2}}}Gp^*\right) = \frac{1}{\Delta t}DIV\left(u^*\right) \tag{2.83}$$

In order to overcome the computationally expensive approach of solving a variable coefficient Poisson equation every time step, a velocity correction method can be used. By using this method as introduced by Dodd and Ferrante (2014) the variable coefficient Poisson equation is transformed to a constant coefficient equation. This is done by splitting the variable coefficient pressure gradient term into a constant term which is treated implicitly and a variable term which is treated explicitly.

$$\frac{1}{\rho^{n+1}}Gp^{n+1} \rightarrow \frac{1}{\rho_0}Gp^{n+1} + \left(\frac{1}{\rho^{n+1}} - \frac{1}{\rho_0}\right)G\hat{p} \tag{2.84}$$

In which $\rho_0 = \min\left(\rho_g, \rho_l\right)$ and

$$\hat{p} = \begin{cases} p^n & , J = 1 \\ 2p^n - p^{n-1} & , J = 2 \end{cases} \tag{2.85}$$

J=1 and J=2 indicate constant or linear extrapolation of p^{n+1}. Substituting (2.84) in (2.83) a constant coefficient Poisson equation for pressure is achieved,

$$LAP\left(p^{n+1}\right) = DIV\left[\left(1 - \frac{\rho_0}{\rho^{n+1}}\right)G\left(\hat{p}\right)\right] + \frac{\rho_0}{\Delta t}DIV\left(\mathbf{u}^*\right) \tag{2.86}$$

LAP and *G* are discrete Laplace and gradient operators. Equation (2.86) can be solved directly by a fast Poisson solver such as McKenney, Greengard and Mayo (1995).

2.9.1 Direct pressure solver
The governing equations for incompressible two-phase flow are:

$$\nabla \cdot \mathbf{u} = 0 \tag{2.87}$$

$$\frac{\partial \mathbf{u}}{\partial t} + \nabla \cdot (\mathbf{u}\mathbf{u}) = \frac{1}{\rho}\left[-\nabla p + \frac{1}{Re}\nabla \cdot \left(\mu\left(\nabla \mathbf{u} + \nabla \mathbf{u}^T\right)\right) + \frac{1}{We}f_\sigma \right] + \frac{1}{Fr}g \tag{2.88}$$

Where f_σ is the force per unit volume due to surface tension:

$$f_\sigma = \sigma \kappa \nabla H(\phi) \tag{2.89}$$

To compute an approximate velocity the right-hand side of the momentum equation (2.88) without the pressure gradient term is used,

$$RU^n = -\nabla \cdot \left(\mathbf{u}^n\mathbf{u}^n\right) + \frac{1}{Re}\left[\frac{1}{\rho^{n+1}}\nabla \cdot \left(\mu^{n+1}\left(\nabla \mathbf{u}^n + \left(\nabla \mathbf{u}^n\right)^T\right)\right)\right] +$$
$$\frac{1}{We}\left[\frac{1}{\rho^{n+1}}\kappa^{n+1}\nabla H^{n+1}(\phi)\right] + \frac{1}{Fr}g \tag{2.90}$$

The surface tension force is then multiplied by $\rho/\langle\rho\rangle$, in which $\langle\rho\rangle \equiv 1/2\left(\rho_g + \rho_l\right)$. Therefore, the surface tensions is constant across the interface. Thus (2.90) becomes:

$$RU^n = -\nabla \cdot \left(\mathbf{u}^n\mathbf{u}^n\right) + \frac{1}{Re}\left[\frac{1}{\rho^{n+1}}\nabla \cdot \left(\mu^{n+1}\left(\nabla \mathbf{u}^n + \left(\nabla \mathbf{u}^n\right)^T\right)\right)\right] +$$
$$\frac{1}{We}\left[\frac{\kappa^{n+1}\nabla H^{n+1}(\phi)}{\langle\rho\rangle}\right] + \frac{1}{Fr}g \tag{2.91}$$

The approximate velocity is used to advance the velocity field in the pressure-correction method.

$$\frac{\mathbf{u}^{n+1} - \mathbf{u}^*}{\Delta t} = \frac{1}{\rho^{n+1}}\nabla p^{n+1} \tag{2.92}$$

By taking the divergence of (2.92) and imposing the divergence free condition on $\mathbf{u}^{n+1}$ the Poisson equation with the variable coefficient is obtained. By substituting the split

as in equation (2.84) in (2.92), and taking its divergence, equation (2.86) is obtained which can be solved by a fast Poisson solver. The Poisson equation is solved by one-dimensional FFTs in two directions and Gauss elimination in the other direction.

Depending on the explicit schemes to solve convective, viscous and surface tension terms, the time step is restricted as follows:

$$\Delta t \leq \frac{1}{2} \min \left(\Delta t_c, \Delta t_s, \Delta t_f \right) \tag{2.93}$$

In which,

$$\Delta t_c = \frac{h}{|u|_{max} + |v|_{max} + |w|_{max}} \tag{2.94}$$

$$\Delta t_s = \sqrt{\frac{We \max(\zeta, 1)}{4\pi}} h^{3/2} \tag{2.95}$$

$$\Delta t_f = \frac{2h}{|\mathbf{u}^n| + \sqrt{|\mathbf{u}^n|^2 + 4hF}} \tag{2.96}$$

Where h is the uniform mesh width and,

$$\zeta = \frac{\rho_l}{\rho_g} \tag{2.97}$$

$$F = \left| -\frac{3}{2} A\left(\mathbf{u}^n\right) + \frac{1}{2} A\left(\mathbf{u}^{n-1}\right) - \frac{1}{\rho} \left(\frac{1}{Re} D\left(\mathbf{u}^n\right) - Gp^{n-\frac{1}{2}} \right) + \frac{1}{Fr} z \right| \tag{2.98}$$

$$D = D_{exp} + D_{imp} \tag{2.99}$$

The spatial discretization of the equations are presented here in 2D. The 3D discretization is analogous.

$$RU = RCU + RDU + RBU \tag{2.100}$$

In which RCU refers to the convective fluxes, RDU diffusive fluxes and RBU body forces.

$$RCU = -\nabla \cdot \left(\mathbf{u}^n \mathbf{u}^n \right) \tag{2.101}$$

$$RDU = \frac{1}{\text{Re}} \left[\frac{1}{\rho^{n+1}} \nabla \cdot \left(\mu^{n+1} \left(\nabla \mathbf{u}^n + \left(\nabla \mathbf{u}^n \right)^T \right) \right) \right] \tag{2.102}$$

$$RBU = \frac{1}{We} \left[\frac{\kappa^{n+1} \nabla H^{n+1} (\phi)}{\langle \rho \rangle} \right] + \frac{1}{Fr} g \tag{2.103}$$

The diffusive terms are discretized as follows:

$$U_{i+1/2,j} = \frac{1}{\text{Re}} \frac{1}{\rho_{i+1/2,j}} \left(\begin{array}{c} \dfrac{DUX_{i+1,j} - DUX_{i,j}}{\Delta x} + \\ \dfrac{DUY_{i+1/2,j+1/2} - DUY_{i+1/2,j-1/2}}{\Delta y} \end{array} \right) \tag{2.104}$$

$$RDV_{i,j+1/2} = \frac{1}{\text{Re}} \frac{1}{\rho_{i,j+1/2}} \left(\begin{array}{c} \dfrac{DUY_{i+1/2,j+1/2} - DUY_{i+1/2,j-1/2}}{\Delta x} + \\ \dfrac{DVY_{i,j+1} - DVY_{i,j}}{\Delta y} \end{array} \right) \tag{2.105}$$

The arithmetic mean is used to compute the density at the staggered locations:

$$\rho_{i+1/2,j} = \frac{1}{2} \left(\rho_{i+1,j} + \rho_{i,j} \right) \tag{2.106}$$

$$DUX_{i,j} = 2\mu_{i,j} \left(\frac{u_{i+1/2,j} - u_{i-1/2,j}}{\Delta x} \right) \tag{2.107}$$

$$DUY_{i+1/2,\,j+1/2} = \mu_{i+1/2,\,j+1/2} \left(\dfrac{\dfrac{u_{i+1/2,\,j+1} - u_{i+1/2,\,j}}{\Delta y} +}{\dfrac{v_{i+1,\,j+1/2} - v_{i,\,j+1/2}}{\Delta x}} \right) \qquad (2.108)$$

$$DVY_{i,\,j} = 2\mu_{i,\,j} \left(\dfrac{v_{i,\,j+1/2} - v_{i,\,j-1/2}}{\Delta y} \right) \qquad (2.109)$$

The staggered viscosity is computed as follows:

$$\mu_{i+1/2,\,j+1/2} = \dfrac{1}{4}\left(\mu_{i+1,\,j+1} + \mu_{i+1,\,j} + \mu_{i,\,j+1} + \mu_{i,\,j} \right) \qquad (2.110)$$

In order to prevent uniform acceleration when gravity acts in the direction of periodic boundaries, special treatment is needed. Therefore, a term for hydrostatic pressure is added to the right hand side of equation (2.88) as follows:

$$f_h = -\dfrac{\rho_1 V_1 + \rho_2 V_2}{V_1 + V_2} g \qquad (2.111)$$

The weighted average is used to better capture the flow properties in the cells containing the interface.

Then the components of the RBU are discretized as:

$$RBU_{i+1/2,\,j} = \dfrac{1}{We}\dfrac{k_{i+1/2,\,j}}{\langle \rho \rangle}\left(\dfrac{C_{i+1,\,j} - C_{i.j}}{\Delta x} \right) \qquad (2.112)$$

$$RBV_{i,j+1/2} = \frac{1}{We} \frac{k_{i,j+1/2}}{\langle \rho \rangle} \left(\frac{C_{i,j+1} - C_{i,j}}{\Delta y} \right) +$$
$$\frac{1}{Fr} \left(\frac{f_h}{\rho_{i,j+1/2}} - 1 \right) \tag{2.113}$$

In which,

$$k_{i+1/2,j} = \begin{cases} \kappa_{i+1,j} & if \quad \kappa_{i,j} = 0 \\ \kappa_{i,j} & if \quad \kappa_{i+1,j} = 0 \\ \frac{1}{2}\left(\kappa_{i+1,j} + \kappa_{i,j} \right) & otherwise. \end{cases} \tag{2.114}$$

The input for the fast Poisson solver is obtained by taking the divergence of the right hand side of (2.86) as:

$$\nabla^2 p_{i,j}^{n+1} = \frac{DPX_{i+1/2,j} - DPX_{i-1/2,j}}{\Delta x} +$$
$$\frac{DPY_{i,j+1/2} - DPY_{i,j-1/2}}{\Delta y} + DIVU_{i,j} \tag{2.115}$$

Where,

$$PX_{i+1/2,j} = \left(1 - \frac{\rho_0}{\rho_{i+1/2,j}} \right) \left(\frac{\hat{p}_{i+1,j} - \hat{p}_{i,j}}{\Delta x} \right) \tag{2.116}$$

$$DPY_{i,j+1/2} = \left(1 - \frac{\rho_0}{\rho_{i,j+1/2}} \right) \left(\frac{\hat{p}_{i,j+1} - \hat{p}_{i,j}}{\Delta y} \right) \tag{2.117}$$

$$DIVU_{i,j} = \frac{\rho_0}{\Delta t} \left(\frac{u^*_{i+1/2,j} - u^*_{i-1/2,j}}{\Delta x} \right) \left(\frac{v^*_{i,j+1/2} - v^*_{i,j-1/2}}{\Delta y} \right) \tag{2.118}$$

Then the components of updated velocity field by applying the pressure correction to $\mathbf{u}^*$ are discretized as:

$$u_{i+1/2,j}^{n+1} = u_{i+1/2,j}^{*} - \Delta t \left[\begin{array}{l} \dfrac{1}{\rho_0} \left(\dfrac{p_{i+1,j}^{n+1} - p_{i,j}^{n+1}}{\Delta x} \right) + \\[2ex] \left(\dfrac{1}{\rho_{i+1/2,j}} - \dfrac{1}{\rho_0} \right) \left(\dfrac{\hat{p}_{i+1,j} - \hat{p}_{i,j}}{\Delta x} \right) \end{array} \right] \tag{2.119}$$

$$v_{i,j+1/2}^{n+1} = v_{i,j+1/2}^{*} - \Delta t \left[\begin{array}{l} \dfrac{1}{\rho_0} \left(\dfrac{p_{i,j+1}^{n+1} - p_{i,j}^{n+1}}{\Delta y} \right) + \\[2ex] \left(\dfrac{1}{\rho_{i,j+1/2}} - \dfrac{1}{\rho_0} \right) \left(\dfrac{\hat{p}_{i,j+1} - \hat{p}_{i,j}}{\Delta y} \right) \end{array} \right] \tag{2.120}$$

2.9.2 Direct velocity solver

The same splitting technique is used for the viscous terms in the Navier-Stokes equations:

$$\frac{\mathbf{u}^{*} - \mathbf{u}^{n}}{\Delta t} = \frac{1}{2} \left(3H^{n} - H^{n-1} \right) + $$
$$\frac{1}{2} \frac{1}{\text{Re}} \frac{1}{\rho^{n+1}} \left(\nabla \cdot \left(\mu^{n+1} D \left(u^{n} \right) \right) + \nabla \cdot \left(\mu^{n+1} D \left(u^{*} \right) \right) \right) \tag{2.121}$$

$$H^{k} = -\nabla \cdot \left(u^{k} u^{k} \right) + \frac{1}{\rho^{k+1}} \frac{1}{We} f_{\sigma}^{k+1} \tag{2.122}$$

$$D \left(u^{k} \right) = \left(\nabla u^{k} + \left(\nabla u^{k} \right)^{T} \right) \tag{2.123}$$

$$\frac{1}{\rho^{n+1}} \nabla \cdot \left(\mu^{n+1} D \left(u^{*} \right) \right) \rightarrow $$
$$\nu_0 \nabla^2 u^{*} + \frac{1}{\rho^{n+1}} \nabla \cdot \left(\mu^{n+1} D \left(u^{n} \right) \right) - \nu_0 \nabla^2 u^{n} \tag{2.124}$$

In which,

$$\nu_0 = \frac{1}{2} \left(\frac{\mu_1}{\rho_1} + \frac{\mu_2}{\rho_2} \right) \tag{2.125}$$

Substituting (2.124) in (2.121) gives:

$$\frac{\mathrm{u}^* - \mathrm{u}^n}{\Delta \mathrm{t}} = \frac{1}{2}\left(3H^n - H^{n-1}\right) +$$

$$\frac{1}{\mathrm{Re}}\frac{1}{\rho^{n+1}}\left(\nabla \cdot \left(\mu^{n+1}D\left(u^n\right)\right)\right) + \frac{1}{2}\frac{1}{\mathrm{Re}}\left(\nu_0 \nabla^2 u^* - \nu_0 \nabla^2 u^n\right) \quad (2.126)$$

The constant coefficient Helmholtz equation is obtained by multiplying equation (2.126) by ($-2\mathrm{Re}/\nu_0$):

$$\nabla^2 \mathrm{u}^* - \frac{2\,\mathrm{Re}}{\nu_0 \Delta t}u^* = -\frac{2\,\mathrm{Re}}{\nu_0 \Delta t}u^n - \frac{\mathrm{Re}}{\nu_0}\left(3H^n - H^{n-1}\right) -$$

$$\frac{2}{\nu_0}\frac{1}{\rho^{n+1}}\left(\nabla \cdot \left(\mu^{n+1}D\left(u^n\right)\right)\right) + \nabla^2 u^n \quad (2.127)$$

Equation (2.127) can be solved by a fast elliptic solver.

2.9.3 Verification and validation of the numerical scheme with direct solvers

In order to verify the numerical scheme with the direct pressure and velocity solver, simulations on colliding water droplets in air in Figure 2.11, falling droplet and rising bubble, Figure 2.12 are performed. The simulation parameters are presented in Table 2.1. As the results show, there is an excellent agreement between the results of the direct solver scheme and the iterative solver while the direct solver is 25 times faster than the other method. This advantage makes it possible to perform simulations on finer mesh. Since the results of the iterative solver scheme have already been validated by experimental data for colliding droplets by Kwakkel et al. (2013), this comparison shows the validity of the direct solver scheme.

Table 2.1 Simulation parameters for validation cases

Case	Solver	Re	We	Domain dimension	Mesh size	dt
Colliding droplets	Direct	8.77	0.0037	4×5×4	120×150×120	3×10^{-5}
	Iterative					5×10^{-5}
Falling droplet	Direct	15.21	6.3×10^{-4}	6×6×6	144×144×144	6×10^{-5}
	Iterative				96×96×96	
Rising bubble	Direct	108.30	60.53	6×6×6	144×144×144	6×10^{-5}
	Iterative				96×96×96	

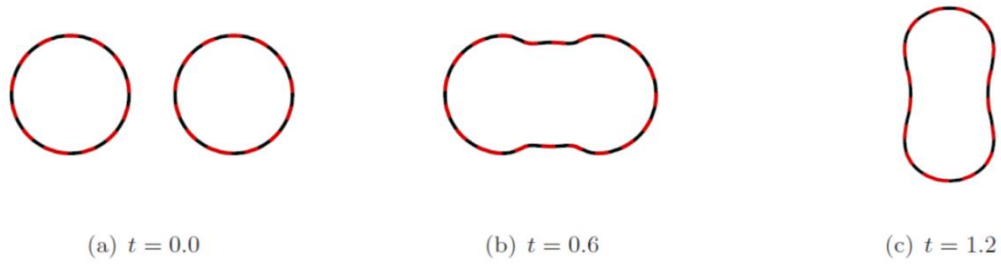(a) $t = 0.0$ (b) $t = 0.6$ (c) $t = 1.2$

Figure 2.11 Colliding water droplets in air, the dashed line refers to the iterative solver and the solid line refers to the direct solver, t is the dimensionless time.
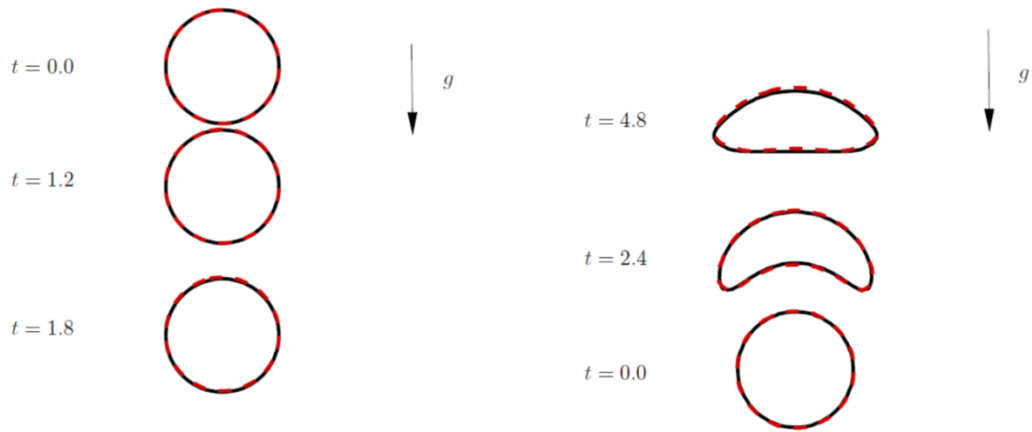

$t = 0.0$

g

$t = 4.8$

g

$t = 1.2$

$t = 2.4$

$t = 1.8$

$t = 0.0$

Figure 2.12 Colliding water droplets in air, the dashed line refers to the iterative solver and the solid line refers to the direct solver, t is the dimensionless time.

3   Heat transfer from a solid spherical particle

In this chapter the heat transfer from a single solid spherical particle is studied. Direct Numerical Simulations are performed for different Reynolds numbers. In the first part heat transfer from a solid spherical particle with uniform surface temperature is studied. In the next part, heat transfer from a spherical particle with variable internal temperature is studied. The main objective of this chapter is to study the effect of the non-uniform surface temperature on the heat transfer rate at the surface of a spherical particle.

3.1 Literature review

There are many studies in the literature on flow, heat and mass transfer from solid spherical particles and deforming droplets. As it was mentioned in chapter 2, in most of these studies, simplifications and assumptions are made such as considering an axisymmetric two-dimensional geometry. Figure 3.1 is an example of an experimental study on the flow over a cylinder which can be used to compare with numerical results of an axisymmetric two-dimensional model of flow over a sphere.

In the study of flow and heat transfer over bodies a few non-dimensional numbers are of importance. The Reynolds number (*Re*) defines the ratio between the inertial forces and the viscous forces and is used to determine whether the flow is laminar or turbulent which can be written as,

$$\mathrm{Re} = \frac{\rho U D}{\mu} \tag{3.1}$$

For flow over a solid sphere for a Reynolds number between 20 and 210, the flow is steady axisymmetric and a two-dimensional axisymmetric model is sufficient to capture the flow streamlines. However, for a Reynolds between 210 and 270 the wake behind the flow is steady but not axisymmetric and therefore a three-dimensional model should be used to capture the flow streamlines, Magarvey and Bishop (1961).
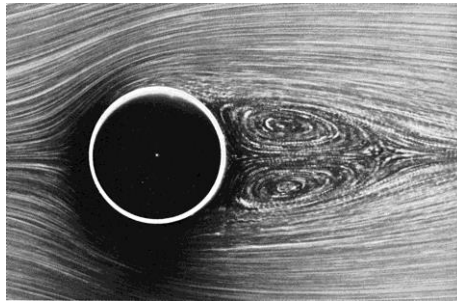
Figure 3.1 Flow passing a cylinder (2D flow)

The Prandtl number (*Pr*) is the ratio between the viscous diffusivity and the thermal diffusivity. It determines the relative thickness of the momentum to the thermal boundary layer. If *Pr<<1* it means that the thermal diffusivity is dominant and the

thermal boundary layer thickness is much larger than the momentum boundary layer. For *Pr=1* the momentum and thermal boundary layer thickness are equal and for *Pr>>1* the momentum diffusivity is dominant and therefore the momentum boundary layer is much larger than the thermal boundary layer.

The Biot number (*Bi*) describes the ratio between the convection at the surface and the conduction inside of a body. For *Bi<<1* the conduction inside of the body is dominant and therefore the temperature of the body can be assumed uniform. The difference between the Bi number and the Nusselt number (*Nu*) is that the latter describes the ration between the convection at the surface and conduction in the fluid over the body. The Peclet number (*Pe*) in heat transfer is the ratio of the convective heat transfer to the diffusive heat transfer and it can be written as, *Pe=RePr*.

In some studies the surface temperature is assumed to be uniform, and in some other studies the whole spherical particle is assumed to be at a uniform temperature, such as the study of Comer and Kleinstreuer (1995). However, this assumption is only valid in case of smaller Biot numbers than unity, where the conduction inside the object is much faster than convection heat transfer.

Some early studies on heat and mass transfer from solid spheres are, the study of Gostkowski and Costello (1970) in which they experimentally investigated the effect of free stream turbulence on heat transfer to the stagnation point of a sphere. Chen and Mucoglu (1977) later studied flow and heat transfer characteristics of laminar mixed forced and free convection about a sphere. They solved the transformed conservation equations by a finite difference method for gases with a Prandtl number of 0.7. They have also examined the effects of the variation of the local free stream velocities on the wall shear and surface heat transfer. Hayward and Pei (1978) studied the local heat transfer of a sphere in turbulent air stream for Reynolds number ranging between 2600 and 6100 based on the sphere diameter. They have shown that the interaction between the free stream turbulence and the boundary layer causes the boundary layer to become turbulent at the laminar separation point. Morris (1982) studied the effect of a strongly temperature-dependent viscosity on slow flow past a hot sphere. In all of these studies the surface temperature is assumed to be uniform. In a more recent study Feng and Michaelides (2001) investigated transient heat transfer rate from a sphere at high Reynolds and Peclet numbers. The stream function-vorticity formulation is used to solve the governing equations. They have shown the dependence of the heat transfer rate on the Reynolds number.

The abovementioned numerical studies assume axisymmetric solutions. Increased computing power made full three-dimensional simulations possible. Dandy and Dwyer

(1990) performed a three-dimensional study for steady linear shear flow past a heated sphere for low Reynolds numbers assuming the spherical particle to be isothermal. Nguyen et al. (1993) have studied unsteady conjugate heat transfer from a translating spherical droplet by direct numerical simulation. The energy and momentum equations are solved by a hybrid spectral scheme. Simulations on a single sphere settling under gravity by Lattice-Boltzmann techniques were performed by ten Cate et al. (2002), they have also compared their results with particle imaging velocimetry experiments.

Bagchi, Ha and Balachandar (2000) have performed a direct numerical simulation (DNS) of flow and heat transfer from a sphere in a uniform cross flow in spherical coordinates using the Fourier-Chebyshev spectral collocation method for Reynolds numbers up to 500. Three different wake regimes are identified with increasing the Reynolds number. They have investigated the effect of unsteadiness and three-dimensionality on heat transfer from a sphere. They have found larger difference between the local Nusselt numbers in the wake region of a three-dimensional flow comparing with the axisymmetric results. However, there is a small difference between the surface-average Nusselt numbers of the two cases.

Niazmand and Renksizbulut (2003) have modeled the heat transfer from a rotating sphere in a spherical coordinates with a control-volume based integration technique. They found out that the temperature distributions around the particle are strongly affected by the particle rotation and surface blowing. However, the surface-average heat transfer rates are not affected significantly. Dan and Wachs (2010) have studied the heat transfer of spherical particles by a Finite Element Method (FEM). They have computed the motion of the particles by a Discrete Element Method (DEM). The objective of their work is to understand the effect of heat transfer on the flow pattern in non-isothermal particulate flows. They have reported the sedimentation of a single sphere in a semi-finite channel.

In a more recent study, Tavassoli et al. (2013) have investigated heat transfer in a particulate flow with direct numerical simulation. They use an immersed boundary method and a fixed Eulerian grid to solve the momentum and energy equations. The particulate phase is treated by introducing momentum and heat source terms at the boundary of the solid particle, representing the momentum and thermal interactions between fluid and particle. Santarelli and Fröhlich (2015) have simulated spherical bubbles in a turbulent channel flow by immersed boundary method, while Koblitz et al. (2017) have used an overset grid method to simulated a particulate flow with rigid particles using refinement of the grid at the particle surfaces to reduce the total number of grid points.

The purpose of the present chapter is to provide a detailed overview on heat transfer in solid sphere for high Biot numbers to show the effect of the internal temperature distribution in Nusselt number calculation.

3.2 Modeling heat transfer from a solid spherical particle

The non-dimensional form of the continuity, the Navier-Stokes and the energy equations are solved in a spherical coordinates with a spherical particle at the center of the coordinate system. The surrounding fluid is assumed to be initially stationary and approaches the sphere with a uniform velocity of U_∞. The geometry of the domain and the coordinates system which is applied is shown in Figure 3.2. Inside the sphere, the internal domain, there is no advection and heat transfer is purely by conduction. Therefore, the domain of solution is divided into an internal domain which represents the solid sphere and an external domain representing the surrounding fluid. For each of these domains the corresponding governing equations are solved separately. The interaction of the solid sphere and the surrounding fluid is taken into account by introducing ghost cells adjacent to the interface in each domain. During the time integration of the energy equations the values of temperature are exchanged between the two domains by means of these ghost cells.
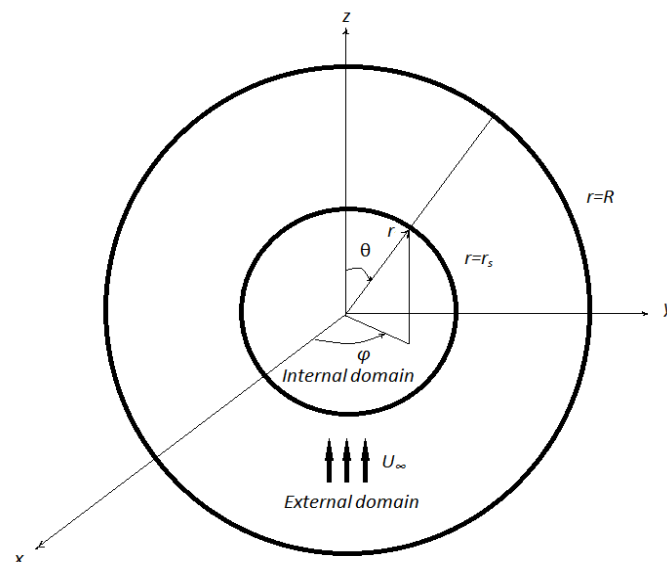
Figure 3.2 Geometry and coordinates.

In order to simulate flow over and heat transfer from the solid sphere, the following equations for conservation of mass, momentum and energy are solved in the spherical coordinates for the external domain:

$$\nabla \cdot \mathbf{u} = 0 \tag{3.2}$$

$$\frac{\partial \mathbf{u}}{\partial t} + \nabla \cdot (\mathbf{u}\mathbf{u}) = -\nabla p + \frac{1}{Re}\nabla^2 \mathbf{u} \tag{3.3}$$

$$\frac{\partial T}{\partial t} + \nabla \cdot (\mathbf{u}T) = \frac{1}{RePr}\nabla^2 T \tag{3.4}$$

In which $\mathbf{u}$ is the velocity vector, ρ is the mass density, P is the pressure and T is the temperature. The governing non-dimensional numbers, the Reynolds number and the Prandtl number are defined as:

$$Re = \frac{\rho_g U_\infty D_0}{\mu_g}, Pr = \frac{C_{p_g}\mu_g}{k_g}$$

The isothermal assumption is only valid if the Biot number is much smaller than 1 (Bi << 1). The Biot number is defined as:

$$Bi = \frac{hL_c}{k_s} \tag{3.5}$$

In which h is the heat transfer coefficient and L_c is the characteristic length as:

$$L_c = \frac{V_s}{A_s} \tag{3.6}$$

In which V_s is the volume of the sphere and A_s is the surface area of the sphere.

In the case that the solid sphere is assumed to be isothermal (Bi << 1) and the internal temperature distribution of the particle is not taken into account solving equations (3.2) - (3.4) gives the complete solution. However, when the isothermal assumption is abandoned, meaning Bi ~ O (1), the internal temperature distribution has to be considered and the energy equation for the internal domain has to be solved as well.

$$\frac{\partial T}{\partial t} = \frac{k'}{\rho' c_p'} \frac{1}{RePr} \nabla^2 T \tag{3.7}$$

In which the non-dimensional thermo-physical properties inside the sphere are:

$$\rho' = \frac{\rho_s}{\rho_g}, C_p{}' = \frac{C_{p_s}}{C_{p_g}}, k' = \frac{k_s}{k_g}$$

In this study a solid sphere of wood in air is considered, the thermal properties are given in Table 3.1.

Table 3.1 Values of constant parameters and properties.

Constant	Value	Unit
D_0	1.2	mm
k_s	0.05	W/mK
ρ_s	900	kg/m^3
Cp_s	2400	J/kgK
k_g	0.0242	W/mK
ρ_g	1.225	kg/m^3
Cp_g	1006.43	J/kgK

A three-dimensional model is applied for this problem in which the spatial terms are discretized by a second order finite volume method on a staggered grid. The Navier-stokes equations are integrated in time with a second order Adams-Bashforth Scheme. The Poisson equation for the pressure is computed with a direct solver using Fourier transformation in φ with cyclic reduction in r and the circumferential direction, θ.

It is assumed that the no-slip boundary condition for velocity holds at the surface of the sphere, while for the external domain the zero-gradient condition is applied at the outer boundary. The boundary condition for the temperature field if the sphere temperature us variable is such that at the surface of the sphere no jump occurs in the heat transfer rate. Therefore, the surface temperature is calculated by the conduction equation in radial direction at the interface. The two domains are coupled by the temperature at the surface of the sphere, as shown in Figure 3.3. Since the two domains are overlapping at the sphere surface, the parameters in ghost cells of one domain are used in solving the governing equations of the other domain. The initial value of these cells is set by the initial

conditions. The sphere temperature is initially higher than the ambient air ($T_s=1$ and $T_\infty=0$). The boundary conditions are summarized as follows:

At $r=R$ (the outer radius of the external domain),

$$\frac{\partial u}{\partial r} = \frac{\partial v}{\partial r} = \frac{\partial w}{\partial r} = \frac{\partial T}{\partial r} = 0 \qquad (3.8)$$

At $r=r_s$ (the radius of the sphere),

$$u = v = w = 0 \qquad (3.9)$$

$$q_{out} = q_{in} \qquad (3.10)$$

In which u, v and w are the velocity components in r, θ and φ direction respectively. r is the radius of the external domain and r_s is the radius of the sphere. The boundary condition which holds in φ direction is the periodic boundary condition for both velocity and temperature. Due to the staggered arrangement of the grid no boundary condition at $\theta = 0$ and π is required. The temperature at the center of the sphere is assumed to remain constant as T_s.
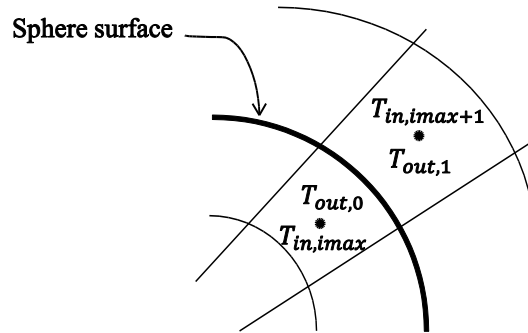
Figure 3.3 Ghost cells next to the solid surface are used to determine the boundary conditions.

If the sphere temperature is considered to be constant, there is no interface temperature boundary condition needed but only a fixed wall temperature at the sphere is used. The far field temperature boundary condition remains the same as in (3.8).

The velocity field is updated with the pressure correction method, see Chapter 2. This velocity field is used in the energy equation of the external domain to find the temperature distribution. At this point the updated outer temperature field is used as the new boundary condition for the energy equation inside the particle to find the internal temperature distribution at the same time step. The result of the internal temperature distribution will then be used as the boundary condition for the external domain solver in the next time step. The governing equations of the external and the internal domains are solved sequentially until the steady state solution is reached. The non-dimensional time step which is used in these simulations is 2.5e-4.

3.3 Heat transfer on a solid sphere with uniform surface temperature

The steady state flow and temperature field for the Reynolds numbers in the range of 50, 100 and 200 are shown in Figure 3.4. The effect of separation at the rear of the particle and the recirculating flow in the wake region of the thermal boundary layer is very well observed. Due to the increase in the thickness of the boundary layer, one can expect the local heat transfer coefficient on the surface of the sphere to be minimal in the separation region. The calculation of the Nusselt number at the surface of the sphere confirms that the lowest heat transfer rate occurs at the separation points at the rear of the spheres. As mentioned before the only phenomenon happening inside the particle is the thermal diffusion which is negligible. The validity of the assumption Bi<<1 is studied later in this chapter. To show the validity of our simulation, the wake length for Re=100 and 200 is compared with the results of Fornberg (1988) as shown in Figure 3.5.
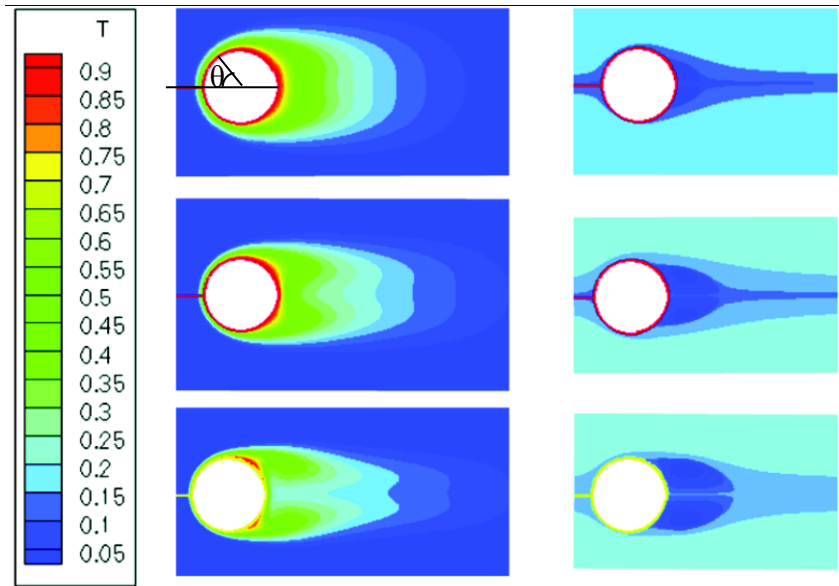
Figure 3.4 External flow isotherms on the left and streamlines on the right for Re=50, 100, 200 and Pr=1.
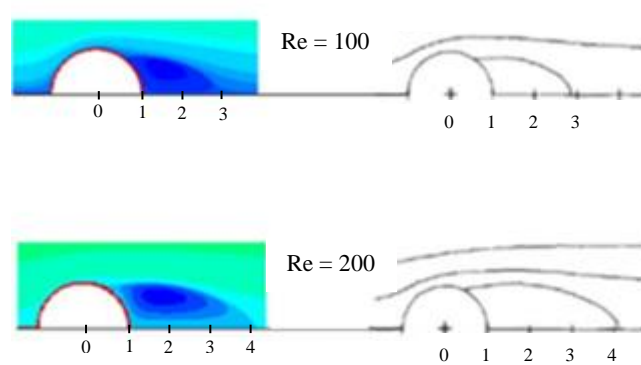
Figure 3.5 Validation of the flow field with wake length, (left) present work, (right) Fornberg (1988).

The local Nusselt number is defined as:

$$Nu_\theta = \frac{h_\theta D_0}{k_g} \tag{3.11}$$

In which, k_g is the air thermal conductivity, D_0 is the sphere initial diameter and h_θ is the local heat transfer coefficient. Since all the equations are non-dimensional the heat transfer coefficient which is calculated from the continuity of heat flux at the interface is also non-dimensional. Replacing the non-dimensional length and thermal conductivity and dropping the primes, the local Nusselt number will be equal to the local heat transfer coefficient:

$$Nu_\theta = h'_\theta \qquad (3.12)$$

From the energy equilibrium at the surface, the heat transfer coefficient can be written as:

$$h'_\theta = \nabla T \cdot n \qquad (3.13)$$

And the surface average Nusselt number is defined as:

$$Nu_{ave,A} = \frac{1}{A} \int_A \nabla T \cdot n dA \qquad (3.14)$$

In which A is the surface area of the sphere and n is the normal vector to the surface of the sphere.

3.3.1 Mesh sensitivity analysis

A mesh size sensitivity test is performed to obtain the proper resolution for this problem. The applied mesh sizes at the interface are shown in Table 3.2. The average Nusselt number for five mesh sizes is shown in Figure 3.6. The results show that for a 50% decrease in the mesh size from 0.005 to 0.0025, the average Nusselt number only changes 3%. Therefore, for the sake of computation expenses simulations are performed with the HRes resolution with the mesh size of 0.005 in the vicinity of the sphere.

Table 3.2 Mesh resolution for sensitivity check.

Mesh resolution label in simulation	Δr adjacent to the interface
LLRes	0.04
LRes	0.02
MRes	0.01
HRes	0.005
HHRes	0.0025
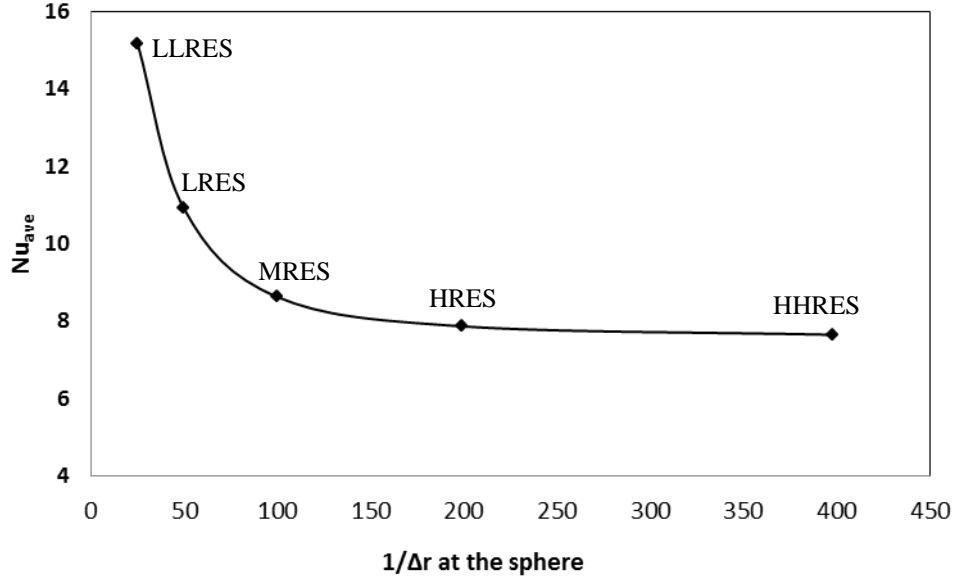
Figure 3.6 The average Nusselt number as a function of the numerical resolution for Re=100.

As an additional check for the near wall grid resolution, the non-dimensional y^+ is calculated as follows:

$$y^+ = \frac{\rho'_g U_\tau \Delta y_1}{\mu'_g}$$

(3.15)

In which, ρ'_g is the non-dimensional density of the air as 1, $U\tau$ is the frictional velocity and Δy_1 is the first cell height. The frictional velocity is calculated using the following equation:

$$U_\tau = \sqrt{\frac{\tau_w}{\rho'_g}}$$

(3.16)

The wall shear stress τ_w can be calculated as follows:

$$\tau_w = \mu'_g \left. \frac{\partial v}{\partial r} \right|_{r=dr_1}$$

(3.17)

v is the velocity in θ direction and dr_1 is the grid size in r direction at the wall. The value of y^+ for Re=200 is shown in Figure 3.7 along the surface of the sphere from the front

stagnation point to the rear stagnation point. It is observed that the maximum y^+ occurs right before the separation point where the shear stress is the maximum. The near wall grid size is below the y^+ value for the whole surface. Therefore, it is concluded that the grid size is sufficiently fine to capture all the small scale effects.
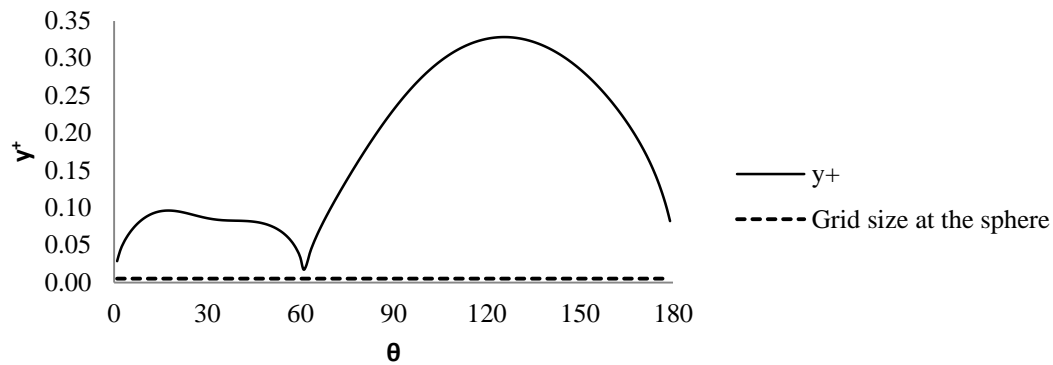
Figure 3.7 y^+ at wall for Re=200 vs grid size at the sphere.

3.3.2 Results and discussions

The local Nusselt number is calculated based on equation (3.12). The results for the case of uniform surface temperature and for different Reynolds numbers in the range of 50-200 are shown in Figure 3.8-Figure 3.10. The local Nusselt number values are compared with the results of Niazmand and Renksizbulut (2003), Bagchi et al. (2000), Gilmanov and Acharya (2008). In the following Figures $\theta=0$ corresponds to the front stagnation point and $\theta=\pi$ corresponds to the rear stagnation point. From the mesh sensitivity and near wall grid resolution study in the previous section it is concluded that the two latter studies do not have enough resolution to capture the heat transfer at the stagnation point accurately. For a given Reynolds number the Nusselt number decreases monotonically to its minimum when moving streamwise along the particle surface. This minimum Nusselt number corresponds to the separation point at the rear of the particle. For a lower Reynolds number the separation will occur farther from the front stagnation point and therefore the minimum local Nusselt number also occurs further away from the front stagnation point. Passing the separation point an increase in the Nusselt number is observed, this is the result of forced convection due to the recirculation behind the sphere in the wake region. As the Reynolds number increases the local Nusselt number increases. This is due to the enhanced forced convection which becomes more dominant than diffusion for higher Reynolds numbers. The average Nusselt number is also larger for a larger Reynolds number as shown in Figure 3.11.
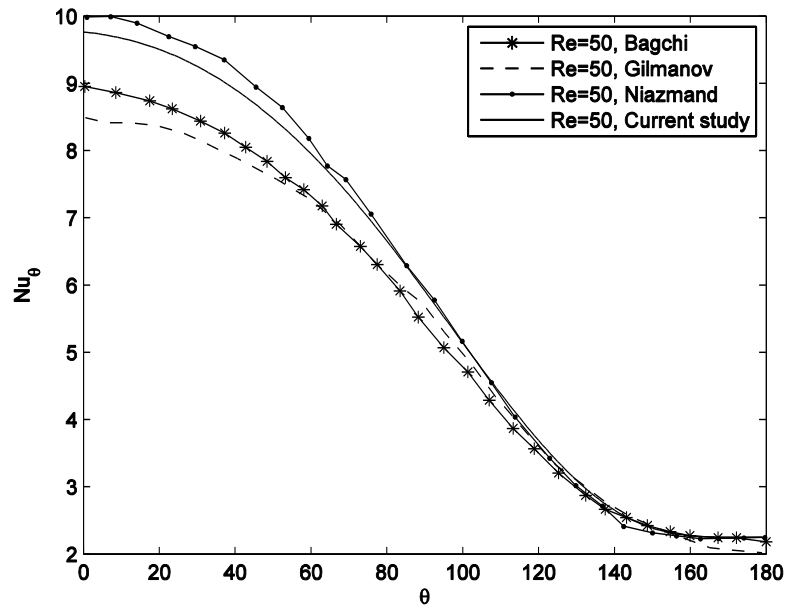
Figure 3.8 Variation of local Nusselt number for Re=50 over an isothermal sphere comparing with results of Bagchi et al. (2000), Gilmanov and Acharya (2008) and Niazmand and Renksizbulut (2003).
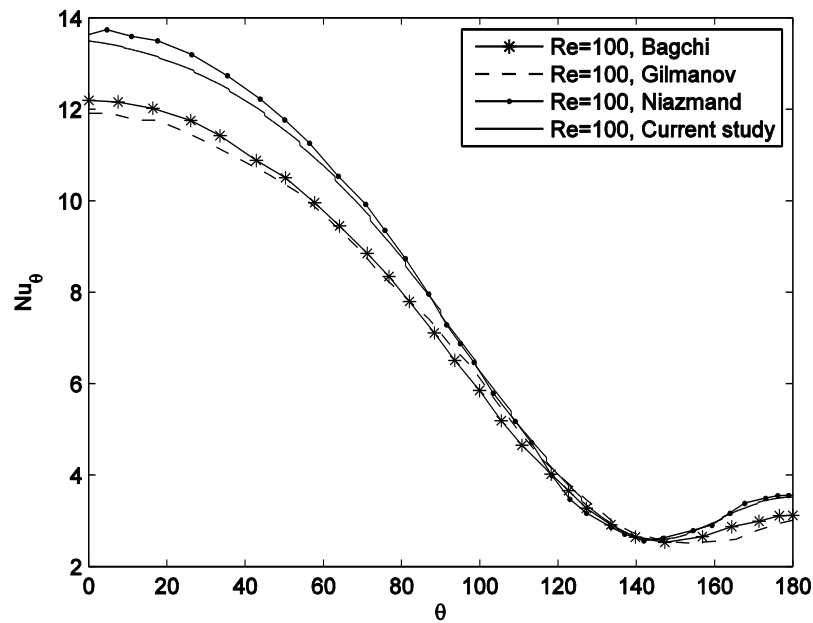

Figure 3.9 Variation of local Nusselt number for Re=100 over an isothermal sphere comparing with results of Bagchi et al. (2000), Gilmanov and Acharya (2008) and Niazmand and Renksizbulut (2003).
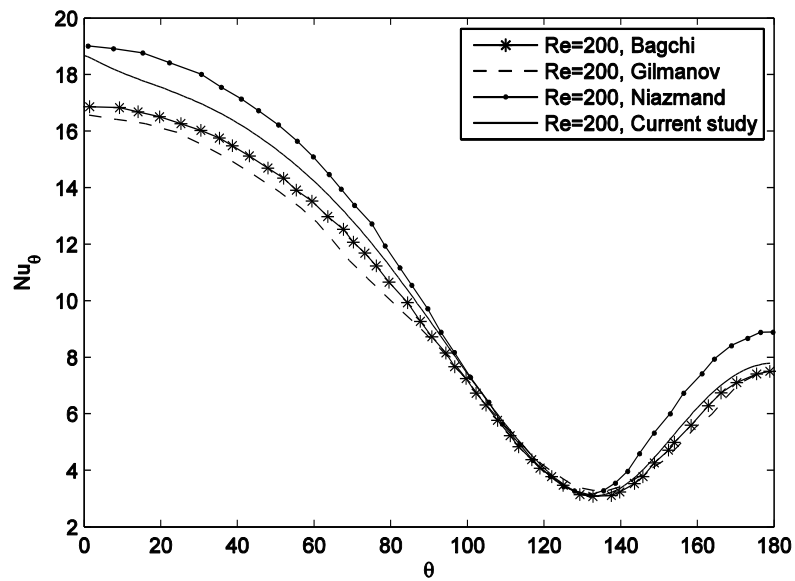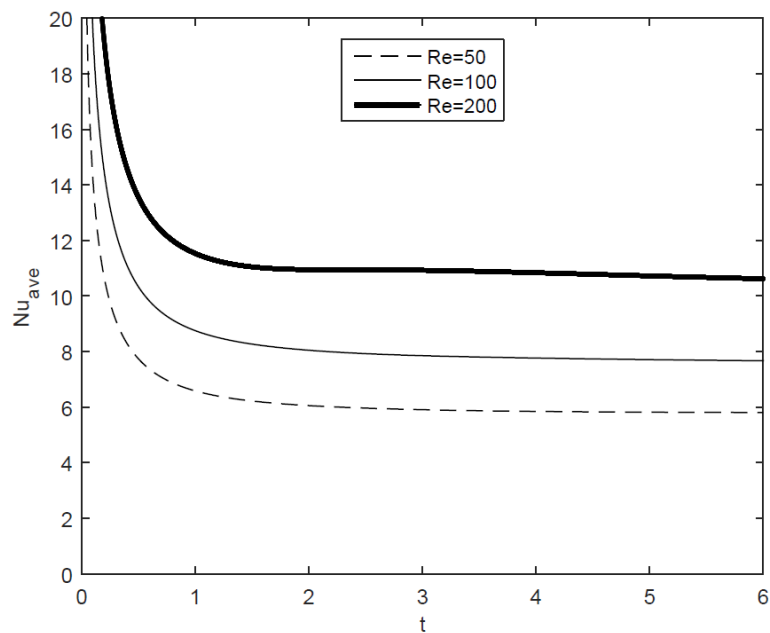
Figure 3.10 Variation of local Nusselt number for Re=200 over an isothermal sphere comparing with results of Bagchi et al. (2000), Gilmanov and Acharya (2008) and Niazmand and Renksizbulut (2003).

Figure 3.11 Variation of average Nusselt number in dimensionless time over an isothermal sphere.

3.3.3 Validation of results

For validation, the average Nusselt number is compared with different correlations available in the literature. These correlations can be applied for flow with a Reynolds number up to 200 and $Pr = 1$.

Ranz and Marshall (1952),

$$Nu = 2 + 0.60 \, Re^{1/2} \, Pr^{1/3} \tag{3.18}$$

Beard (1971),

$$Nu = 1.56 + 0.61 \, Re^{1/2} \, Pr^{1/3} \tag{3.19}$$

Whitaker (1972),

$$Nu = 2 + \left(0.40 \, Re^{1/2} + 0.06 \, Re^{2/3} \right) Pr^{0.4} \tag{3.20}$$

Sayegh (1979),

$$Nu = 2 + 0.473 Re^{0.552} \, Pr^{0.78/Re^{0.145}} \tag{3.21}$$

Clift, Grace and Weber (1978),

$$Nu = 1 + \left[1 + \left(Re \, Pr \right)^{-1} \right]^{1/3} Re^{0.41} \, Pr^{1/3} \tag{3.22}$$

As it is observed in Figure 3.12, the average Nusselt number obtained in this study is in line with the results from the correlations.
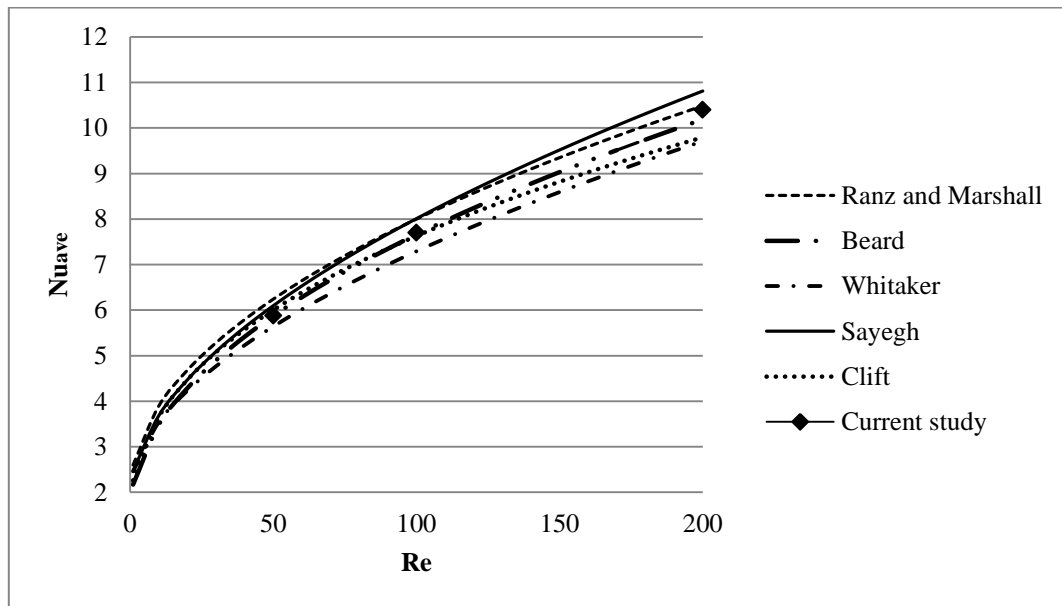
Figure 3.12 Comparison of average Nusselt numbers for a solid sphere.

Using the non-dimensional length and thermal conductivity and the average Nusselt number the average Biot number can be written as:

$$Bi_{ave} = \frac{6Nu_{ave,A}}{k_s/k_g} \tag{3.23}$$

Substituting the $Nu_{ave,A}$ from Figure 3.11 for different Reynolds numbers gives the corresponding Biot number as shown in Table 3.3. The results show that the assumption of uniform temperature inside the particle is not valid and therefore the internal temperature distribution has to be considered as well.

Table 3.3 The average Biot number for sphere with uniform temperature.

Re	Bi$_{ave}$
50	16.8
100	22.4
200	30.4

3.4 Results and discussions on solid sphere heat transfer with non-uniform internal temperature

For the case of a sphere with internal temperature variation the energy equation inside the sphere is also solved. Evaluating the energy equilibrium at the surface of the sphere gives the heat transfer coefficient as:

$$h'_\theta = \frac{1}{(T_{s'} - T'_\infty)} \nabla T \cdot n \qquad (3.24)$$

In which $T_{s'}$ is the local non-dimensional surface temperature of the sphere, T_∞' is the non-dimensional initial ambient temperature. The surface average Nusselt number is then:

$$Nu_{ave} = \frac{1}{A(T_{s'} - T'_\infty)} \int \nabla T \cdot n \, dA \qquad (3.25)$$

In which A is the surface area of the sphere and n is the normal vector to the surface of the sphere.

The isotherms of internal and external domain for cooling of a solid sphere for Reynolds numbers of 50, 100 and 200 are shown in Figure 3.13 for a steady average Nusselt number from the sphere, which is reached at a later time for a higher Reynolds number as shown in Figure 3.14. In Figure 3.14 the variation of the local surface temperature on the symmetry plane is shown for different Reynolds numbers. At first the surface temperature increases gradually and then dramatically from the front stagnation point towards the separation point. At the separation point the surface temperature reaches its maximum. At this point the hydraulic boundary layer thickness is the largest and consequently heat transfer rate due to forced convection is the least. Therefore, the surface temperature has its minimum change from the initial value.

If the effect of the variation of the surface temperature is considered in the calculation of the Nusselt number, the local Nusselt number according to equation (3.24) will be as shown in Figure 3.16. In this figure the minimum local Nusselt number is occurring at the separation point which occurs closer to the front stagnation point for a larger Reynolds number.
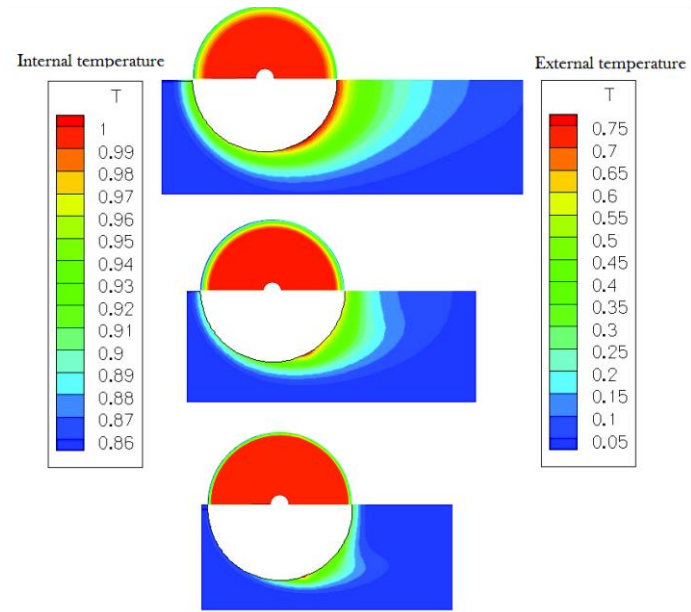
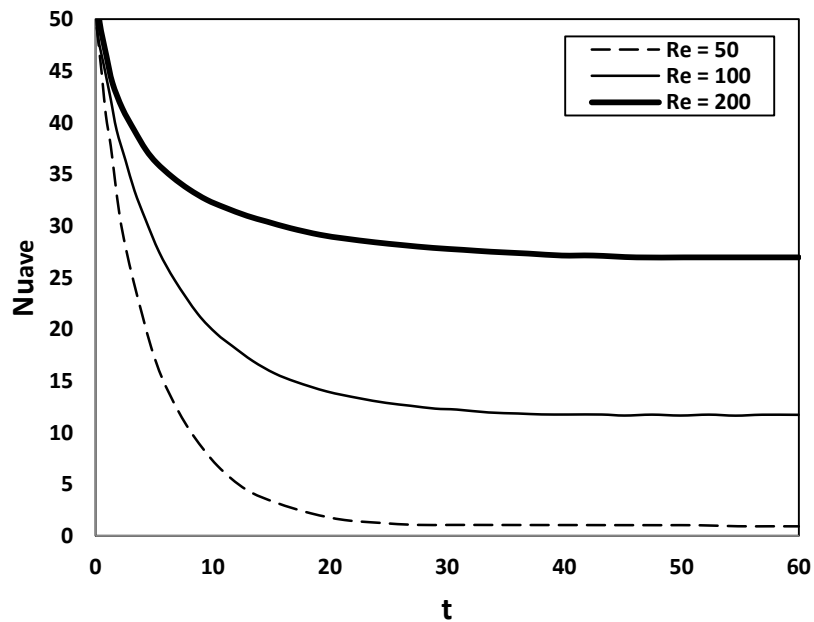**Figure 3.13 Internal and external isotherms for Re=50, 100, 200 (up-down) and Pr=1.**

Figure 3.14 Variation of average Nusselt number in dimensionless time over a sphere with non-uniform surface temperature.
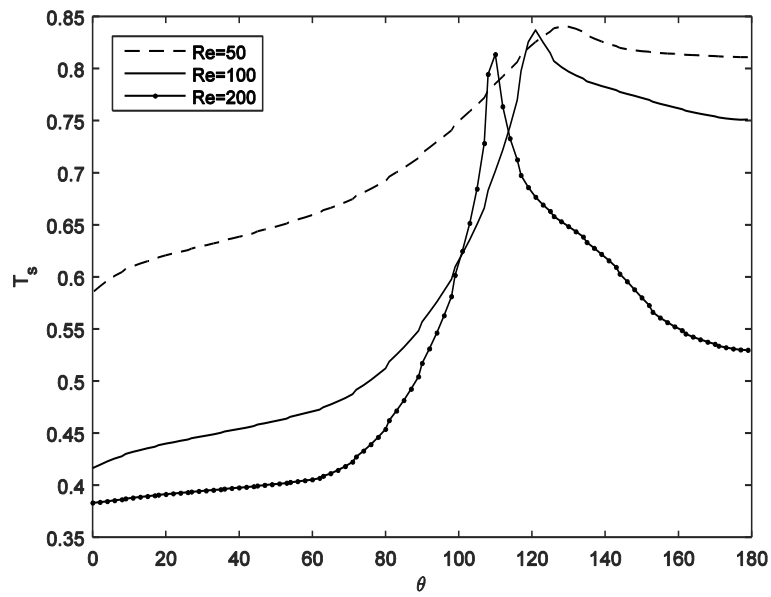
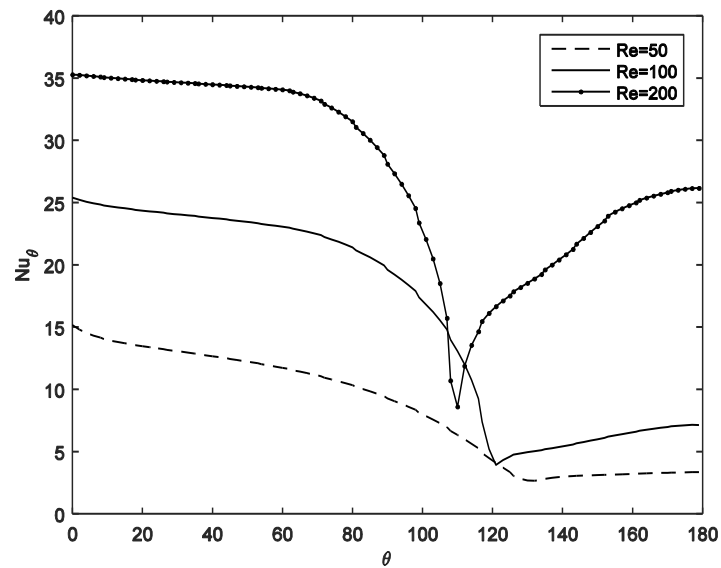**Figure 3.15 Variation of the local surface temperature with Reynolds number.**

Figure 3.16 The local Nusselt number for different Reynolds numbers over a sphere with non-uniform surface temperature including the effect of variable surface temperature.

3.5 Conclusions

The heat transfer from solid spheres with uniform temperature and internal temperature distribution are considered. The grid spacing does not significantly affect the average Nusselt number, but in order to have reliable local Nusselt number, a proper mesh resolution should be used. The results show that if the Biot number is larger than 1, the internal temperature distribution significantly affects the local heat transfer rate. Therefore, to have a reliable estimation of the local Nusselt number, the internal temperature distribution should also be considered. The Biot number is also an indication of how fast the heat transfer rate from a body is stabilized.

4 Heat transfer from a single deforming droplet

In this chapter flow and heat transfer from a single deforming droplet is studied for different Weber and Reynolds numbers. The Navier-Stokes equations and the energy equation are solved on a staggered grid in Cartesian coordinates. Droplets are allowed to deform under the hydrodynamic forces of the surrounding flow. A coupled level-set and volume of fluid (CLSVOF) method is used to capture the highly deformable topology of the droplets. The temperature distribution inside the droplet and its effect on the Nusselt number is studied. The results show that the heat transfer rate is highly influenced by the Reynolds number while the Weber governs the extent of the deformations. Besides the main results, the sensitivity of the Nusselt number calculation on the surface area is also investigated.

4.1 Literature review

Apart from the studies on hard spheres, there are many studies on heat transfer from non-spherical particles and deforming droplets. Abramzon and Sirignano (1989) have performed a study on the droplet vaporization to be used in spray calculations. They have formulated a one-dimensional effective conductivity model for the transient liquid heating with internal circulation. Haywood, Renksizbulut and Raithby (1994) have studied transient deformation and evaporation of droplets numerically. They could predict the droplet shape, as well as the velocity, pressure, temperature and concentration fields in both liquid and gas phases. They concluded that the damping of droplets is due to the circulations inside the droplets.

Comer and Kleinstreuer (1995) studied convection heat transfer to non-spherical particles. They considered heat transfer from rigid spheroids in steady laminar axisymmetric flow and presented mean Nusselt number for different Reynolds numbers, aspect ratios and Prandtl numbers. In the work of Gilmanov and Acharya (2008), heat transfer and flow past deformable objects is studied. The moving boundaries are captured by a hybrid immersed boundary method and a material point method is used to resolve the structural stresses on a fixed Eulerian grid. They have reported flow and heat transfer past a rigid and deforming isothermal sphere as well.

Hase and Weigand (2004) have studied transient heat transfer of deforming droplets by direct numerical simulation using a volume of fluid method. Their study covers flow with a Reynolds number in the range of 360-853 and droplets with a Weber number of 1.33-10.41. They have found that the Nusselt number is significantly dependent on the Weber number at higher Reynolds numbers. They have also investigated the effect of deformations and the consequent variation in the surface area on the Nusselt number.

Sultana et al. (2017) have studied the phase change and dynamics of a free falling water droplet by the Volume of Fluid method in a 2D axisymmetric model while Abdelouahab and Gatignol (2016) have focused on the study of the terminal velocity and instantaneous velocity of a falling water droplet in stagnant air and

Reviewing the literature on this topic, shows still more information is needed on the heat transfer from deforming droplets. The purpose of this chapter is to investigate the effect of surface tension and Reynolds number on heat transfer from a single deforming droplet. The effect of the Weber number on the variation of the surface area and the resulting effect on heat transfer are also addressed.

4.2   Modeling heat transfer from a single deforming droplet

In this section flow past a single deforming droplet with heat transfer between the two fluids is discussed. In comparison with rigid particles, when dealing with deformable objects, the surface tension plays an important role. Therefore, the effect of the surface tension has to be considered when solving the governing equations. The results are presented for different Reynolds and Weber numbers.

The domain and the boundary conditions are shown in Figure 4.1. Equations (2.7)-(2.9) are the governing equations which are solved as explained in Chapter 2. The flow is assumed to approach from the left side to the droplet with a constant velocity of U_∞ at the boundary, where the same boundary conditions as on the other walls are applied for the pressure and the temperature. The flow leaves the domain from the right side where the temperature and velocity gradient in the normal direction to the wall is put to zero and the pressure is assumed to be zero. The velocity is assumed to be continuous across the droplet surface. Since the continuity of stress must hold at the interface, the external forces should be compensated by the surface tension. From the conservation of energy at the interface the boundary conditions for the temperature are obtained. The initial time step is 1.0 e-7 and the fixed time step is 0.002. The constant properties and parameters are given in Table 4.1.
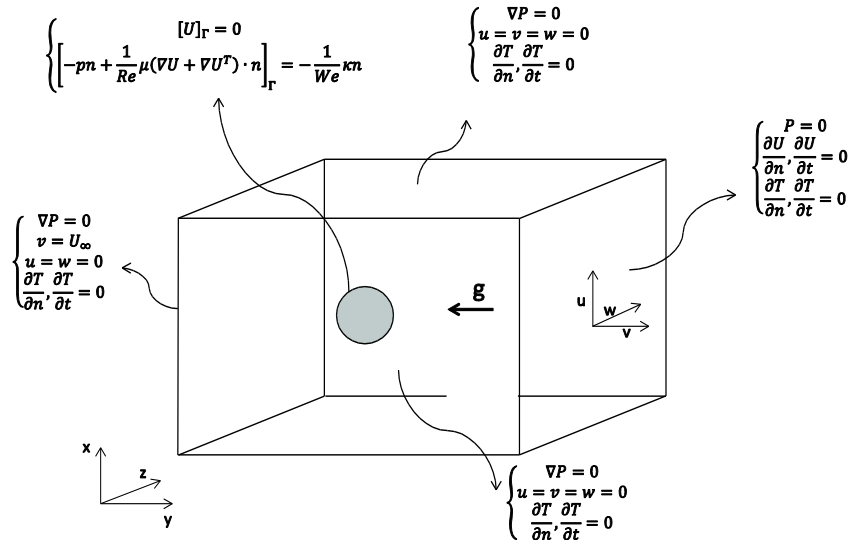
Figure 4.1 Geometry, coordinates and boundary conditions for falling droplet.

Table 4.1 Values of constant parameters and properties in a water-air system.

Constant	Value
k_l / k_g	22.57
ρ_l / ρ_g	833.33
Cp_l / Cp_g	4.16

4.3 Results and discussions on deforming droplet heat transfer

The numerical setup for this case is a single droplet in a rectangular box of (6,18,6) which is meshed by (60,180,60) points. Since larger topological changes occur in colliding droplets finer grids are applied later to capture these changes in more detail. The size of the box is non-dimensionalized by the droplet diameter, D_0=1.2 mm. The non-dimensional temperature of the droplet is initially 1 and for the surrounding air is 0. The development of the temperature field inside and around a single deforming droplet for different Reynolds and Weber numbers are shown in Figure 4.2 to Figure 4.4. It is observed that for a Reynolds number of 50 and different Weber numbers the droplet deformations are more significant with the increase in the Weber number. This is actually expected due to the decrease of the surface tension, since the Weber number and the surface tension have an inverse relation. The larger deformations make a larger surface area for the heat transfer. In Figure 4.5 the development of temperature contours are shown for Re = 100 and We = 1.33. In this case the heat transfer is enhanced due to thinner thermal boundary layer because of the larger Reynolds number.

$$Re = \frac{\rho_g U_\infty D_0}{\mu_g} \tag{4.1}$$

In which U_∞ is the free stream gas velocity and ρ_g=1.225 kg/m^3.

$$We = \frac{\rho_g D_0 U_\infty^2}{\sigma} \tag{4.2}$$

In which σ=0.072 N/m is the surface tension of the water-air system.

In order to take the local temperature variations into account, the temperature gradients at the interface are used and the average Nusselt number can be determined by,

$$Nu_{ave} = \frac{1}{A(T_{s'} - T'_{\infty})} \int k_{reg} \nabla T \cdot n dA \tag{4.3}$$

In which $n = \nabla \phi / |\nabla \phi|$ and k_{reg} is the non-dimensional regularized thermal conductivity.

$$k_{reg} = 1 + \left(\frac{k_l}{k_g} - 1 \right) H(\phi) \tag{4.4}$$

Equations (3.25) and (4.3) only differ in the applied thermal conductivity; which is in the first the thermal conductivity of the air and in the later the regularized thermal conductivity at the interface.

The results of the variation of the Reynolds and Weber numbers and the effect on the Nusselt number are shown in Figure 4.6-Figure 4.8.The average Nusselt number generally increases with increasing the Reynolds number. When the Reynolds number is increased the forced convection becomes dominant in the vicinity of the droplet which enhances the heat transfer rate and therefore results in increasing the Nusselt number. In case of the increase of the Weber number variations in the shape are more significant which results in bluff body shapes and therefore the separation of the streamlines occurs at a smaller angle from the front of the droplet. This results in a small reduction of the Nusselt number.

The effect of surface tension on the average surface temperature is less significant compared to the effect of the Reynolds number. A larger Nusselt number implies a higher heat transfer rate between the droplet and the ambient flow. Therefore, the ambient flow temperature rises more rapidly when the Nusselt number is larger. This, consequently results in higher average surface temperature for larger Reynolds and Weber numbers as shown in Figure 4.9 and Figure 4.10. The Variation of the surface area of the droplets is shown in Figure 4.11, an oscillatory behavior is observed which is more evident for smaller Weber numbers. This behavior has been studied in the literature and for more details the reader is referred to the study of Becker, Hiller and Kowalewski (2006).
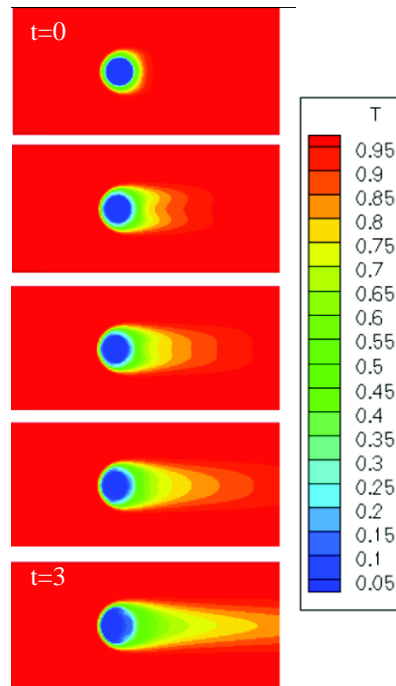
Figure 4.2 Development of temperature distribution as a function of time for Re=50 and We=1.33 (snapshots with constant ∆t during t=3).
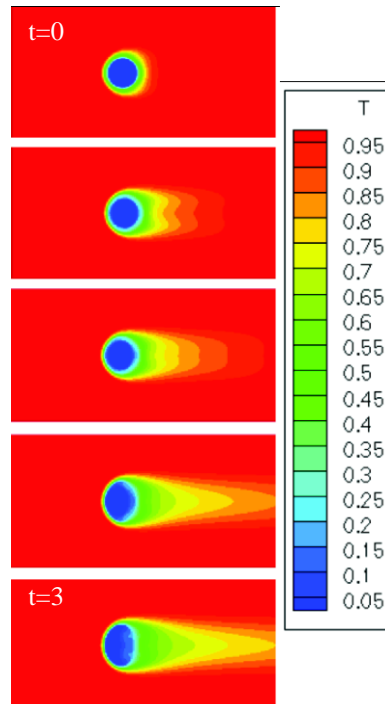

Figure 4.3 Development of temperature distribution as a function of time for Re=50 and We=4.86 (snapshots with constant ∆t during t=3).
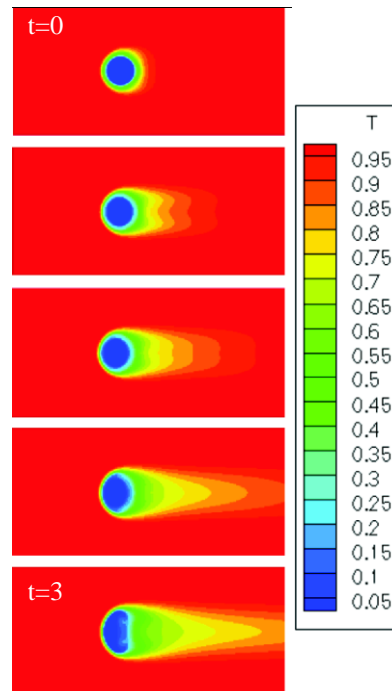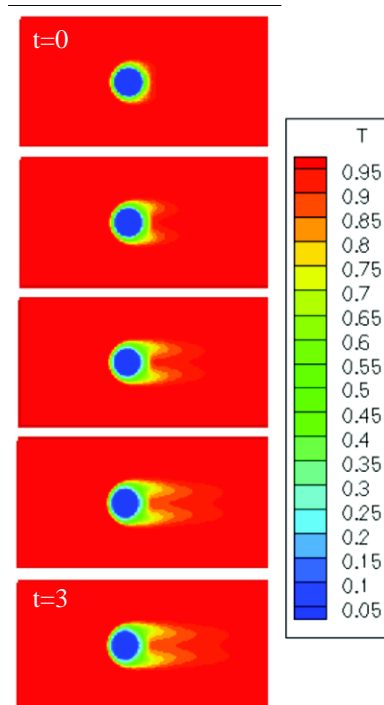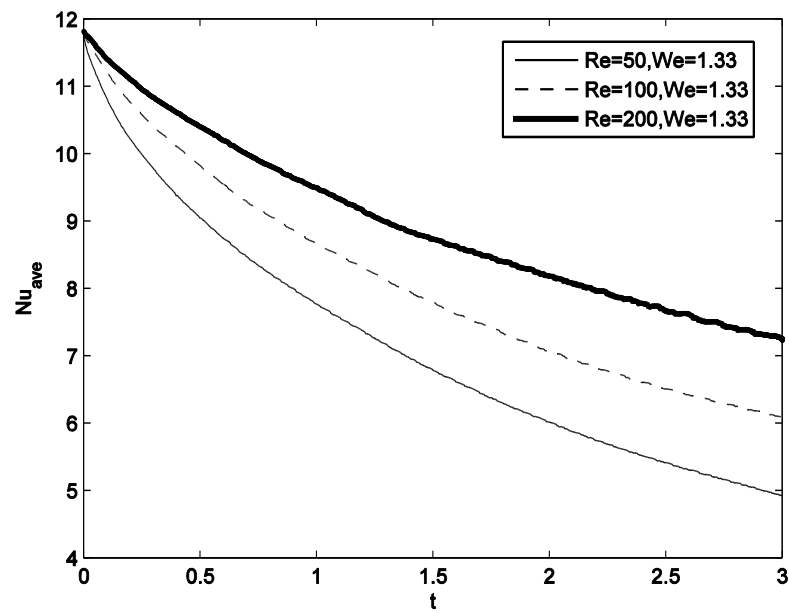
Figure 4.4 Development of temperature distribution as a function of time for Re=50 and We=10.41 (snapshots with constant Δt during t=3).

Figure 4.5 Development of temperature distribution as a function of time for Re=100 and We=1.33 (snapshots with constant Δt during t=3).

Figure 4.6 The average Nusselt number variation in time for different Reynolds numbers and We = 1.33.
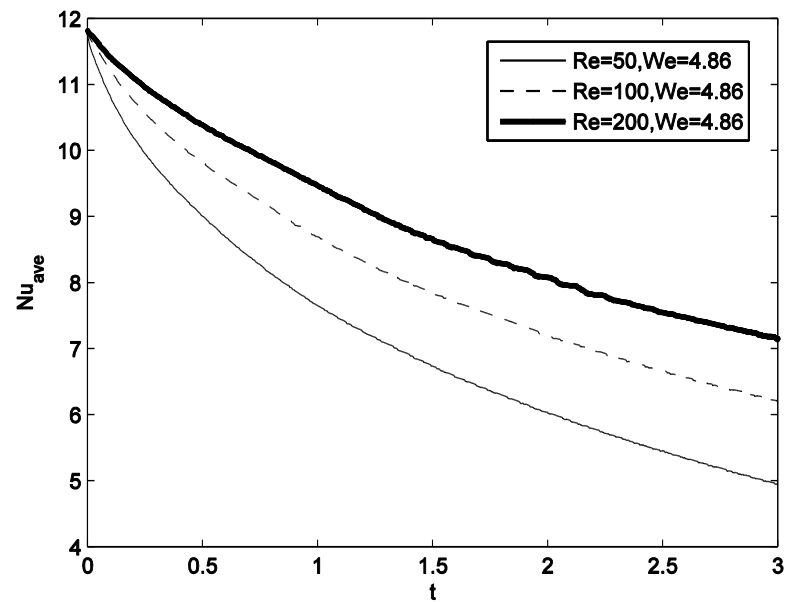
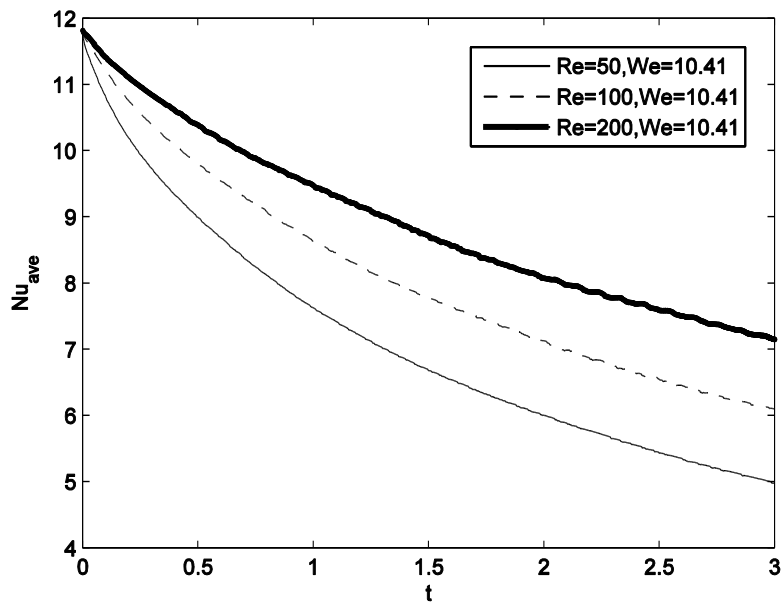**Figure 4.7 The average Nusselt number variation in time for different Reynolds numbers and We = 4.86.**

Figure 4.8 The average Nusselt number variation in time for different Reynolds numbers and We = 10.41.
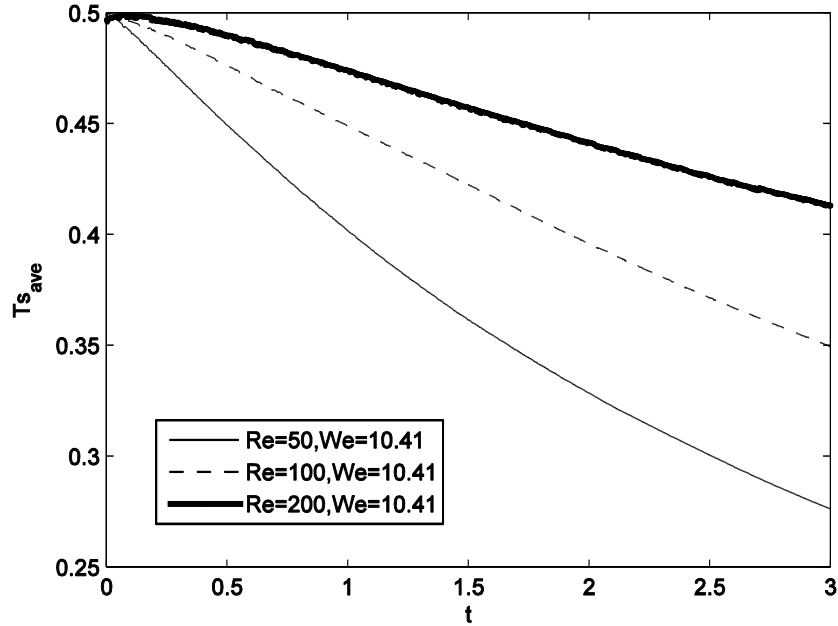
Figure 4.9 Variation of the average surface temperature in time for different Reynolds numbers and We = 10.41.
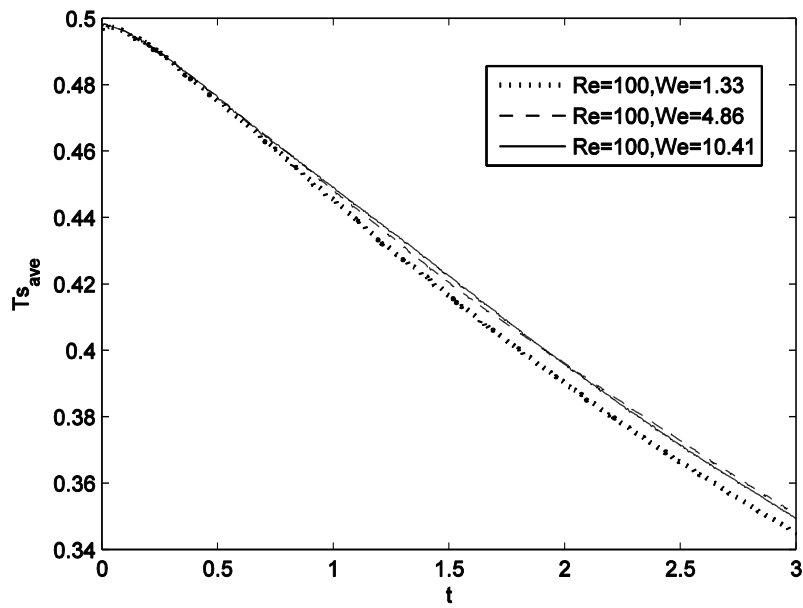
Figure 4.10 Variation of the average surface temperature in time for different Weber numbers and Re = 100.
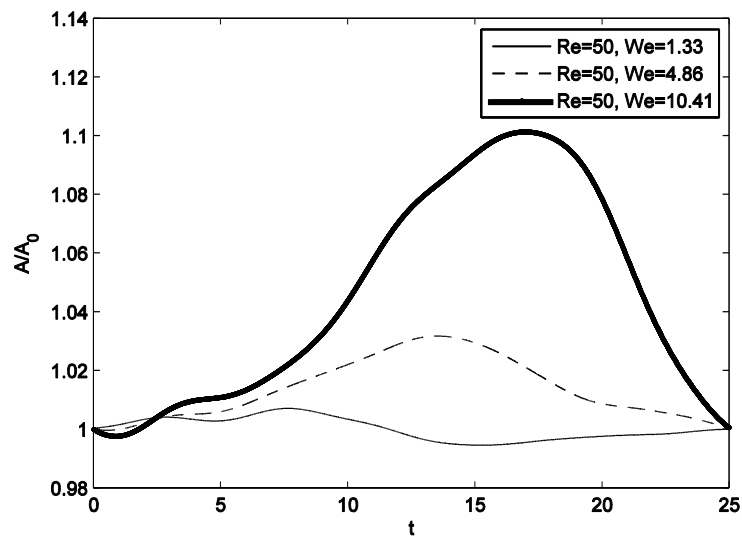

Figure 4.11 Variation of surface area in time for different Weber numbers and Re = 50 with filtering the natural frequency of oscillation of droplets.

4.4 Conclusions

In this chapter the heat transfer over a falling and deforming water droplet in air is studied for different Weber and Reynolds numbers. The results show that the internal temperature distribution affects the heat transfer rate significantly. Therefore, in order to have a reliable estimation of the local Nusselt number, the internal temperature distribution should be considered. In this way the correct local surface temperature of the droplet which is used in the Nusselt number calculations is obtained. By looking into the variation of surface area of droplet due to falling it is observed that a cyclic deformation occurs for which the period increases by increasing the Weber number. Since in the calculation of the Nusselt number the surface area is used, it is important to use the correct surface area from which the heat is being transferred.

The sensitivity study of the heat transfer rate to the Reynolds number and the Weber number shows that increasing the Reynolds number and Weber number both increase the Nusselt number. However, the effect of the Reynolds number variation is more significant as an increase of 100% in the Reynolds number results in an increase 20% in the Nusselt number. While an increase of 250% of the Weber number only results in decreasing the Nusselt number for about 3%. An increase in the Reynolds number increases the convection heat transfer rate. However, the variation of the Weber number results in different frequencies of cyclic deformations and does not affect the heat transfer rate significantly.

5 Heat transfer from colliding droplets

In this chapter flow and heat transfer of colliding droplets of water in air is studied for different Weber numbers, Reynolds numbers and eccentricities of droplets in 3D. The Navier-Stokes equations and the energy equation are solved on a staggered grid in Cartesian coordinates. Droplets are allowed to deform under the hydrodynamic forces of the surrounding flow and the internal and external temperature variations are captured. A coupled level-set and volume of fluid (CLSVOF) method is used to capture the highly deformable topology of the droplets. The effect of the temperature distribution inside the droplet on the Nusselt number is studied. The results show that the heat transfer rate is more influenced by the Reynolds number and the initial configuration of droplets while the surface tension governs the extent of the deformations. The sensitivity of the Nusselt number calculation to the surface area is also investigated. The simulations are performed with two different solvers for the pressure and the velocity to show the difference between the iterative and the direct solvers.

5.1 Introduction

In this chapter a three-dimensional numerical model is used to capture detailed information of the heat transfer problem in colliding droplets. Internal temperature distribution and non-uniform surface temperature are considered in the Nusselt number calculations. The deformations of droplets are captured and the effect of the surface area variation on heat transfer rate is investigated. The heat transfer rate is quantified by the Nusselt number variations for different Reynolds numbers, Weber numbers and collision eccentricities.

5.2   Modeling heat transfer from colliding droplets

The governing equations (2.7)-(2.9) and the numerical method are explained in Chapter 2. The computational domain is a rectangular box of (4.2×4.2×4.2) in which a fixed uniform grid is defined. The domain size is non-dimensionalized by the droplet diameter. The velocity boundary condition for the normal velocity component to each face is the Neumann boundary condition and for other components is the symmetry boundary condition. Pressure is assumed to be zero at all boundaries. The droplet properties are as of water and the ambient flow is assumed to be air. The two droplets approach each other with the initial velocity of U_0. The ambient air is initially still, the velocity is non-dimensionalized by the relative velocity of droplets. The model has been validated against experimental results for head-on collision of droplets, Kwakkel et al. (2013). The Nusselt number is calculated by equation (4.3) and the effect of droplets deformation on the heat transfer rate is investigated. The distance between the centerline of droplets is defined as the eccentricity, E as shown in Figure 5.1. Figure 5.2 shows the schematic configuration of the approaching droplets and the boundary conditions.
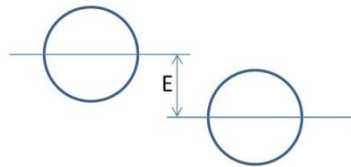

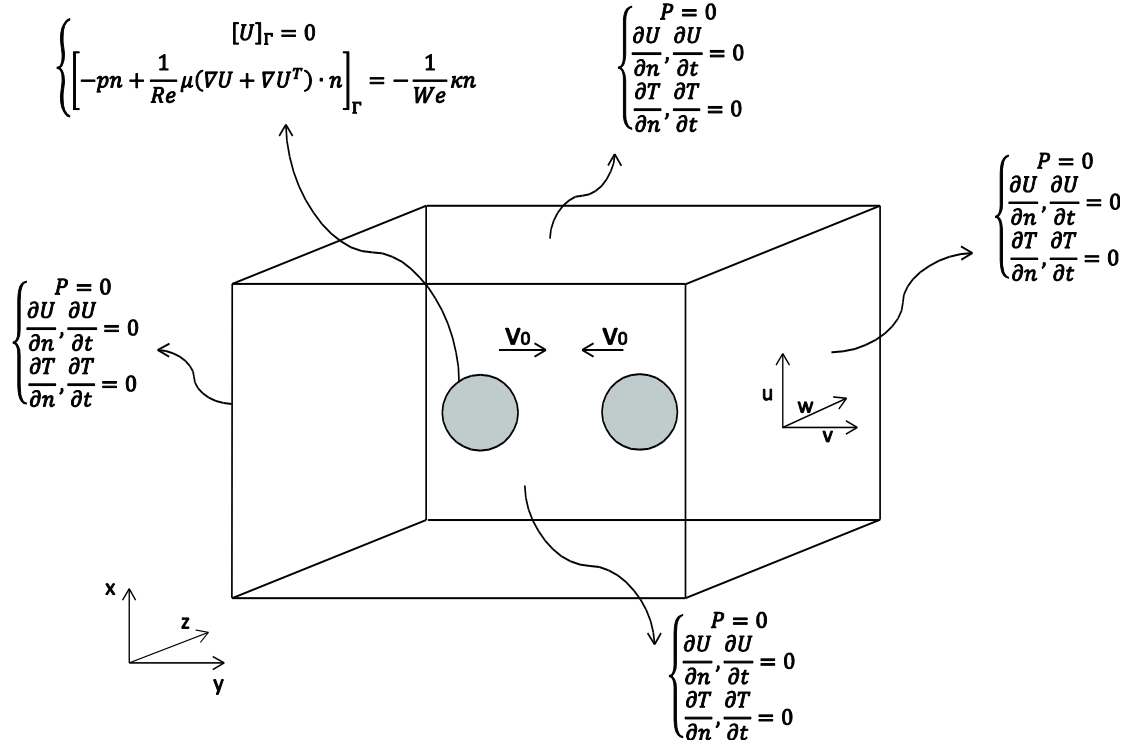**Figure 5.1 Droplets approach with relative velocity U_0 and eccentricity of E.**

$$\begin{cases} [U]_\Gamma = 0 \\ \left[-pn + \dfrac{1}{Re}\mu(\nabla U + \nabla U^T) \cdot n \right]_\Gamma = -\dfrac{1}{We}\kappa n \end{cases}$$

$$\begin{cases} P = 0 \\ \dfrac{\partial U}{\partial n}, \dfrac{\partial U}{\partial t} = 0 \\ \dfrac{\partial T}{\partial n}, \dfrac{\partial T}{\partial t} = 0 \end{cases}$$

$$\begin{cases} P = 0 \\ \dfrac{\partial U}{\partial n}, \dfrac{\partial U}{\partial t} = 0 \\ \dfrac{\partial T}{\partial n}, \dfrac{\partial T}{\partial t} = 0 \end{cases}$$

$$\begin{cases} P = 0 \\ \dfrac{\partial U}{\partial n}, \dfrac{\partial U}{\partial t} = 0 \\ \dfrac{\partial T}{\partial n}, \dfrac{\partial T}{\partial t} = 0 \end{cases}$$

$$\begin{cases} P = 0 \\ \dfrac{\partial U}{\partial n}, \dfrac{\partial U}{\partial t} = 0 \\ \dfrac{\partial T}{\partial n}, \dfrac{\partial T}{\partial t} = 0 \end{cases}$$

Figure 5.2 Domain and boundary conditions.

5.3   Heat transfer from colliding droplets with an iterative solver

To simulate heat transfer in colliding droplets with an iterative solver for pressure and velocity a fixed uniform grid with dimension of (84×84×84) is used. The physical parameters of the simulation cases are shown in Table 5.1. Figure 5.3 shows development of the level-set at the interface for cases 1-3. The temperature development in time for the same cases is shown in Figure 5.4. The droplets deformations and the time development of temperature for bouncing droplets (case 8) are shown in Figure 5.5 and Figure 5.6, respectively. The results are reported in dimensionless numbers as introduced in Chapter 2.

Table 5.1 Simulation parameters for the iterative solver

Case No.	D_0 (mm)	U_0(m/s)	Re	We	Eccentricity(E)
1	1.2	4.5	360	1.33	0
2	1.2	4.5	360	1.33	R_0
3	1.2	4.5	360	1.33	$2R_0$
4	1.2	4.5	360	4.86	$2R_0$
5	1.2	4.5	360	10.41	$2R_0$
6	1.2	4.5	520	1.33	$2R_0$
7	1.2	4.5	835	1.33	$2R_0$
8	1.2	0.5	22.14	0.0149	0
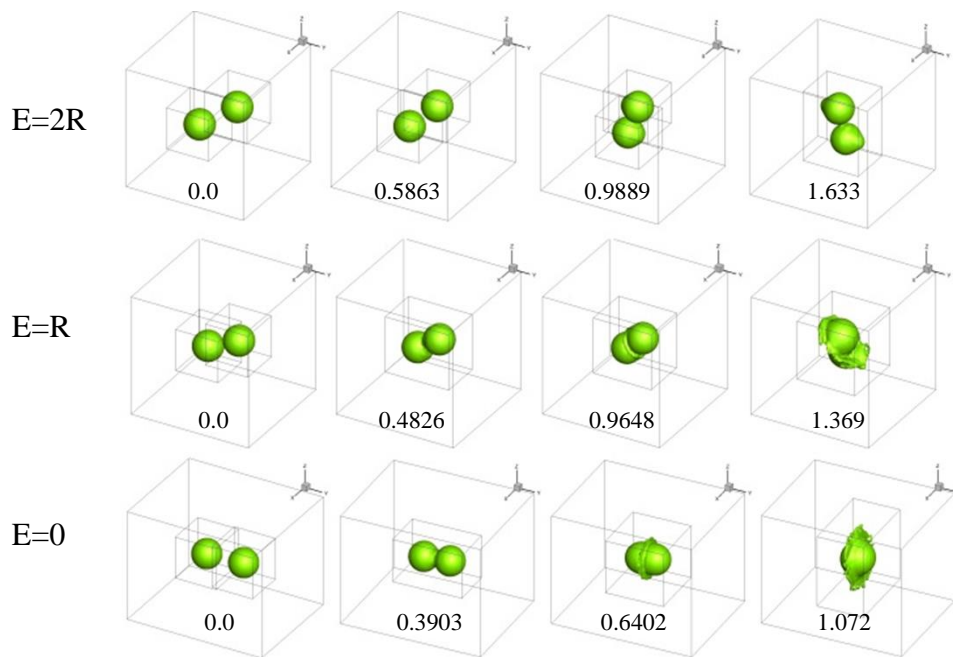
Figure 5.3 The Level set at surface of droplets in time for three different eccentricities for Re = 360 and We = 1.33.
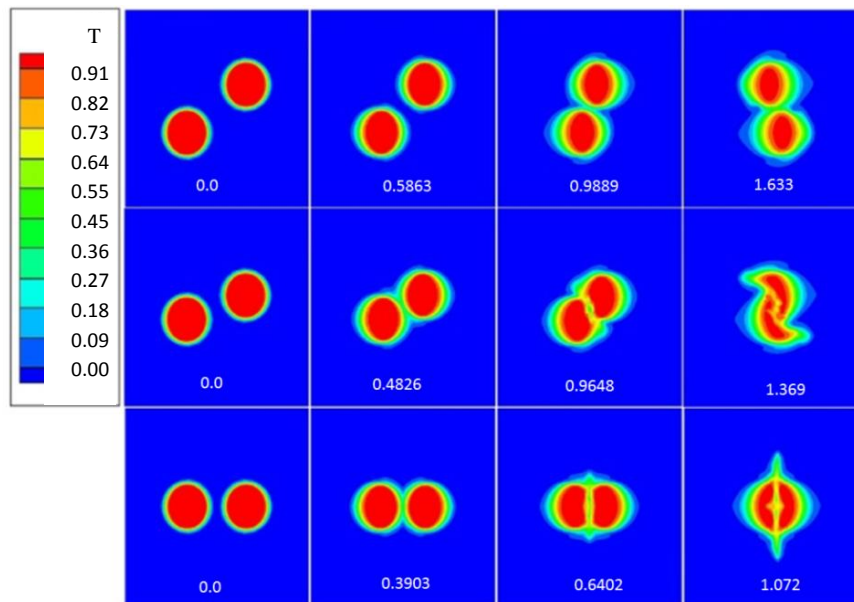
Figure 5.4 The temperature distribution in dimensionless time for three different configuration for Re = 360 and We = 1.33.

Figure 5.7 shows the Nusselt number calculated based on the real surface area, taking into account the deformation of droplets due to collisions and movements. In Figure 5.8 the variation of the Nusselt number is shown for different eccentricity of the approaching droplets with the initial surface area of the droplets applied in the calculation of the Nusselt number. In case of the head-on collision the Nusselt number has a minimum value at $t = 0.8$. At this point the Nusselt number exceeds the corresponding values of the case of $E = 2R_0$, where E is the eccentricity of droplets. This is the result of the thin elongated volumes originated from the collision which enhances the heat transfer rate in this case. From this point the Nusselt number of the droplets with $E = 2R_0$ is the smallest since the droplets remain almost spherical. In the case off-center collision of droplets with $E = R_0$, the heat transfer rate is initially enhanced due to the flow passing the droplets. Since the droplets are experiencing high deformations after collision, the Nusselt number remains high.

Comparing these two figures, the importance of using the real surface area in the calculation of the Nusselt number is evident. If the constant initial surface area is used in the Nusselt number calculation, it is observed in Figure 5.8 that the Nusselt number increases after the collision due to the increase in the surface area in contact with the

flow. Therefore, if the real increasing surface area is applied in the denominator of the Nusselt equation, the overall Nusselt number will decrease as it is seen in Figure 5.7.
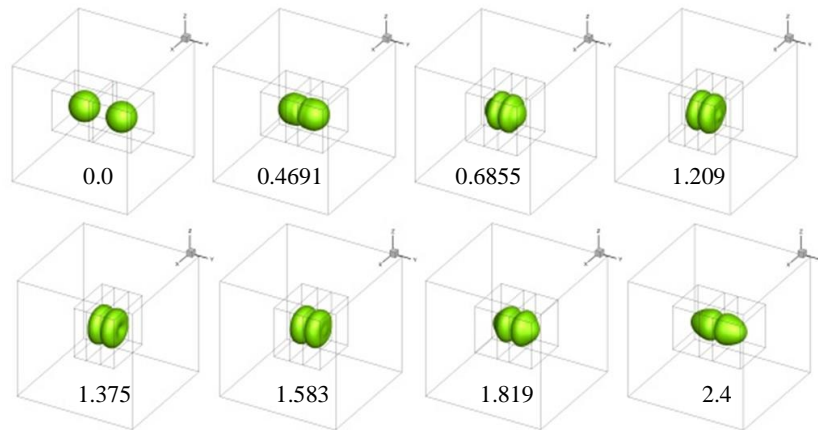

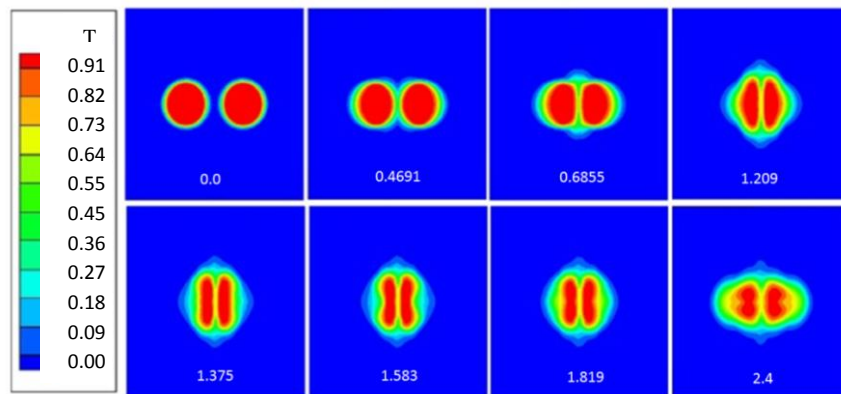**Figure 5.5 The level set at surface of bouncing droplets for
Re = 22.14 and We = 0.0149.**

**Figure 5.6 The temperature distribution in bouncing droplets for
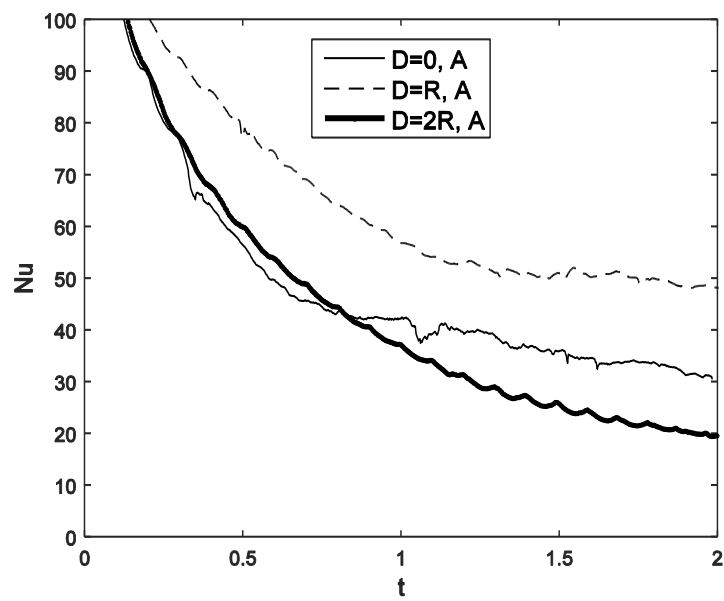Re = 22.14 and We = 0.0149.**

Figure 5.7 Re = 360, We = 1.33 and different eccentricities (E) of droplets. The variation of the Nusselt number in time using the real surface area of droplets.
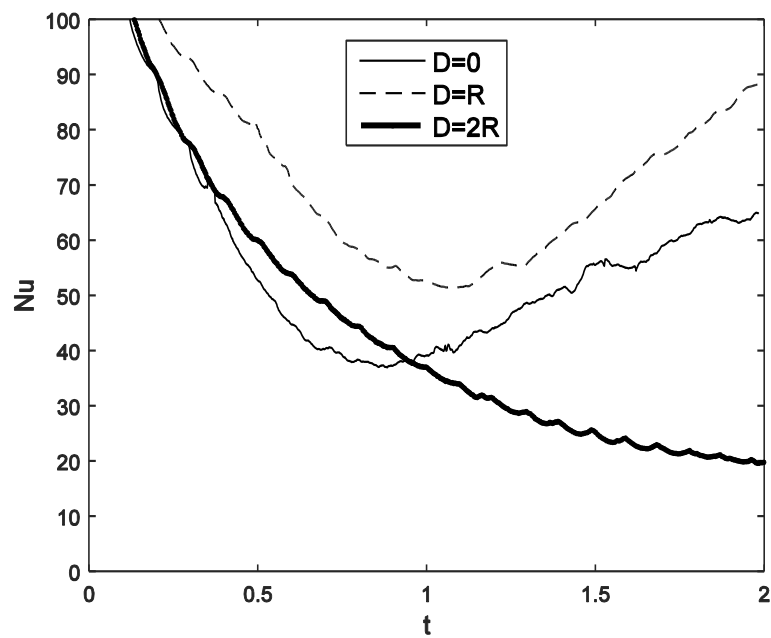
Figure 5.8 Re = 360, We = 1.33 and different eccentricities (E) of droplets. The variation of the Nusselt number in time using the initial surface area of droplets.

In Figure 5.9 the effect of the Weber number on heat transfer rate is shown when the eccentricity of droplets is $2R_0$. In this case the shape of droplets does not change due to the collision. It is observed in this graph that since the Reynolds number is large the Nusselt number is in less affected by the Weber number. The Nusselt number slightly decreases when the Weber number is lower. According to the definition of the Weber number, for a certain approach velocity, a lower value of the Weber number means a higher surface tension. When the surface tension is higher the droplets will rupture more slowly and therefore preserving the enclosed volume of each droplet for a longer time. The result of a lower Weber number is a smaller surface area in contact with the ambient flow which can result in a decrease in the Nusselt number.

The Nusselt number for the initial surface area is shown in Figure 5.10. Since the changes in the surface area of droplets in case of $E = 2R_0$ is almost negligible, one can expect that using the initial surface area of droplets in the Nusselt number calculation would not affect the results considerably.
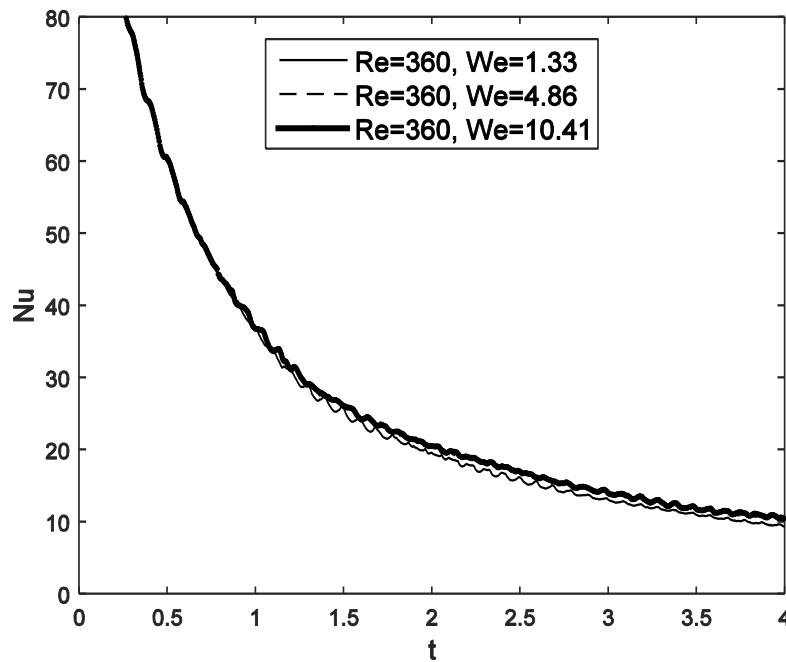

Figure 5.9 Re = 360, E = 2R and different Weber numbers. The variation of the Nusselt number in time using the real surface area of droplets.
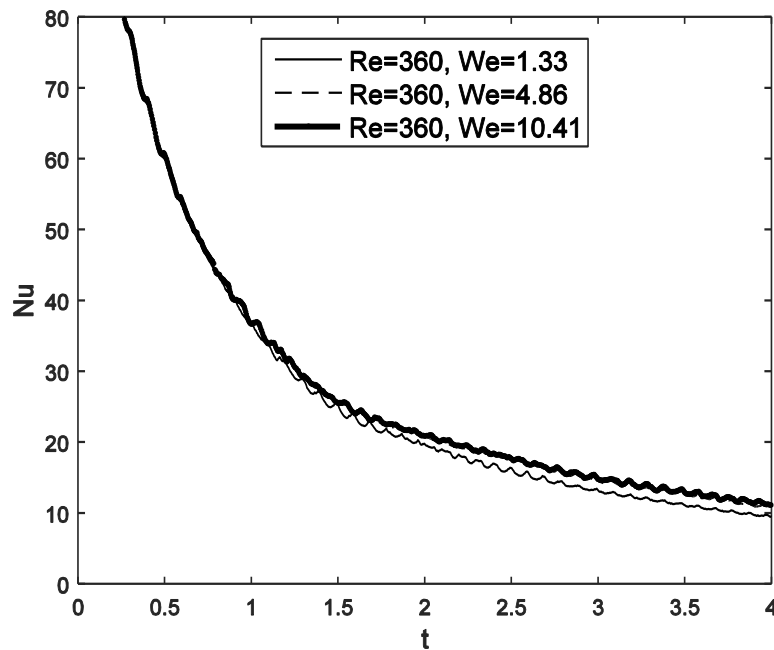
Figure 5.10 Re = 360, E = 2R and different Weber numbers. The variation of the Nusselt number in time using the initial surface area of droplets.

The effect of the Reynolds number on heat transfer rate is also investigated for Re = 360, 520 and 835, when the eccentricity of droplets is $2R_0$ and We = 1.33. As it expected a higher Reynolds number enhances the heat transfer rate due to the better mixing of flow around the droplets and the predominant turbulence effects. The variation of the Nusselt number taking into account the real surface area of droplets is presented in Figure 5.11. It is observed that the Nusselt number decreases by lowering the Reynolds number. The Weber number applied for the simulations in this figure is small and the variation of the surface area is limited. Therefore, the heat transfer rate is mainly ruled by the Reynolds number variation. It is also concluded that when the Reynolds number is large enough, increasing the Reynolds number or changing the Weber number do not have significant effect on the variation of the Nusselt number. So there seems to be a maximum to the heat transfer enhancement for increasing Reynolds numbers.
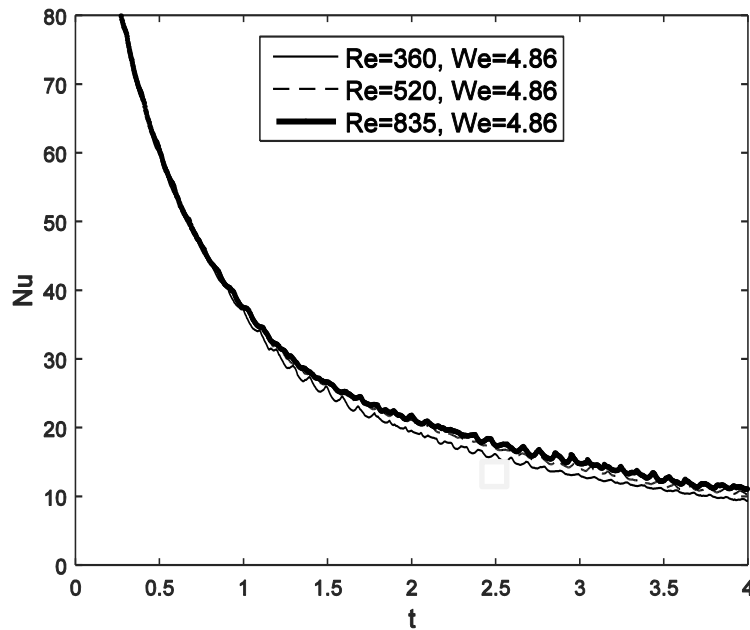
Figure 5.11 We = 4.86, E = 2R and different Reynolds numbers. The variation of the Nusselt number in time using the real surface area of droplets.

5.4   Heat transfer from colliding droplets with a direct solver

As it was mentioned in Chapter 2, the iterative solvers are computationally expensive and using fine mesh for better numerical stability in highly deforming topologies might not be achievable. Therefore, in the this section to perform simulations with high resolution to capture small scale details with high computational speed the direct solver is used. To simulate heat transfer from two colliding droplets with a direct solver for pressure and velocity a fixed uniform grid of ($144 \times 180 \times 144$) is defined on a domain of a rectangular box of ($4 \times 5 \times 4$). The velocity boundary condition in x and z directions is Neumann condition for the normal velocity component to each face and symmetry condition for other components, while the pressure is assumed to be zero at these directions. A periodic boundary condition is applied in y direction. The flow parameters used in the simulations with the direct solver are shown in Table 5.2. The results of this section are published in the International Communications in Heat and Mass Transfer.

Table 5.2 Simulation parameters for the direct solver.

Case	Re	We	Eccentricity (E)
1	8.77	0.00135	0
2	35	0.01351	0
3	70	0.05404	0
4	140	0.21616	0
5	8.77	0.00135	R_0
6	35	0.01351	R_0
7	70	0.05404	R_0
8	140	0.21616	R_0

Figure 5.12 shows the temperature field development in time for head-on collisions. As it is observed in this figure, for cases 1 and 2 in which the Reynolds number and the Weber number are relatively low compared to the other two cases, the droplets remain intact after collision. An oscillating behavior is observed in the overall shape of droplets. Right after collision due to the momentum the droplets are squeezed but since the Weber number is low the surface tension can overcome this momentum and keeps the enclosed volume of droplets. As the Reynolds and Weber numbers increase in cases 3 and 4, the initial momentum of the collision increases and at the same time the surface tension cannot compensate. That is the reason to see those elongated parts in case 3 and separated volumes in case 4 after collision.

In Figure 5.13 the temperature field development in time for the off-center collision of droplets is shown. In this case the effect of the momentum is lowered due to the contact point of droplets after collision. That is why no separated volume is observed for these cases.

The level-set function at the interface is used to visualize the droplet deformations and the variations in the surface area. The changes in the shape and volume of droplets are shown in Figure 5.14 and Figure 5.15 for head-on and off-center collisions respectively. As it is seen in the head-on collision separated volumes of droplet emerge for higher Reynolds and Weber numbers, while in the off-center collision the droplets merge into a larger droplet.
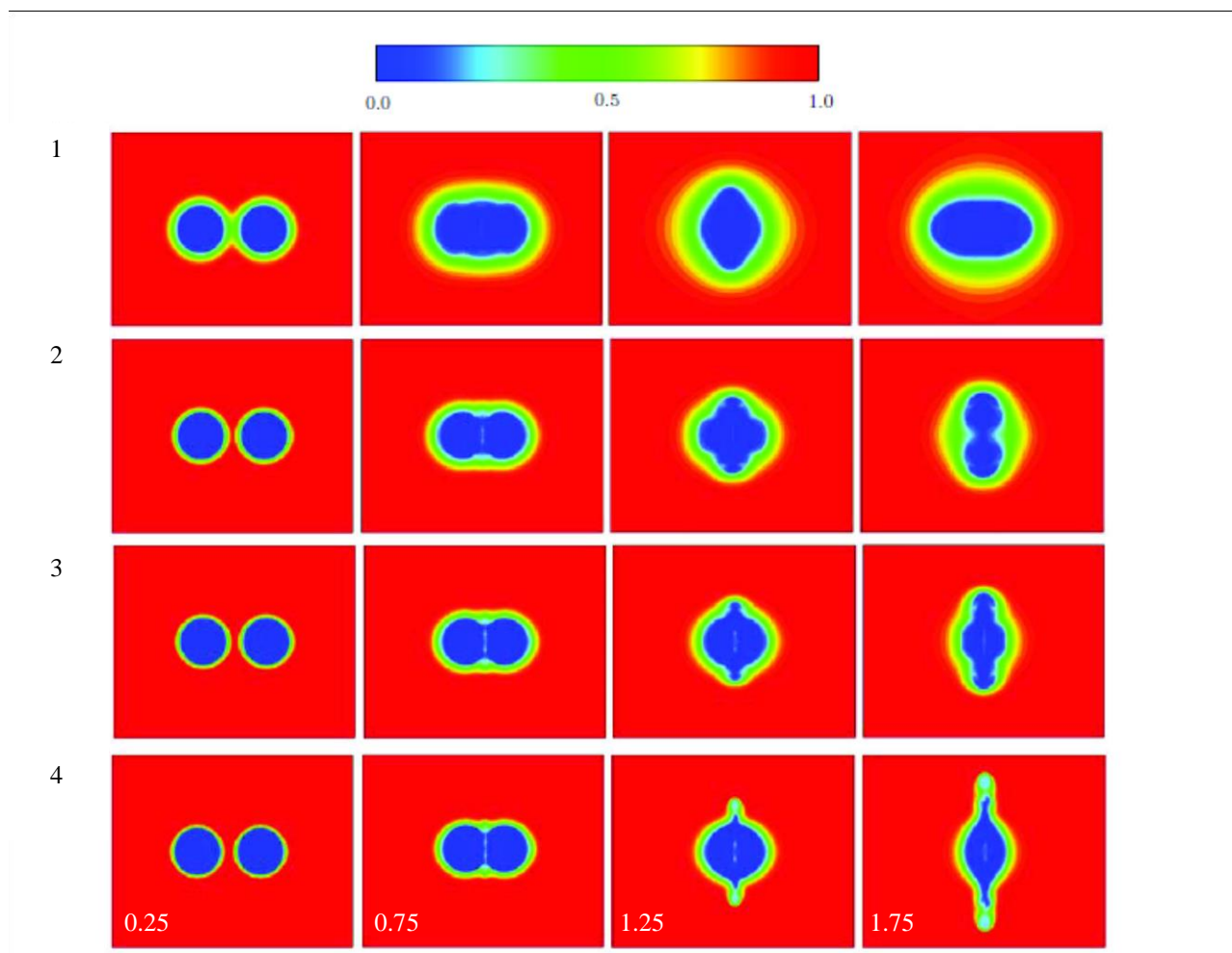
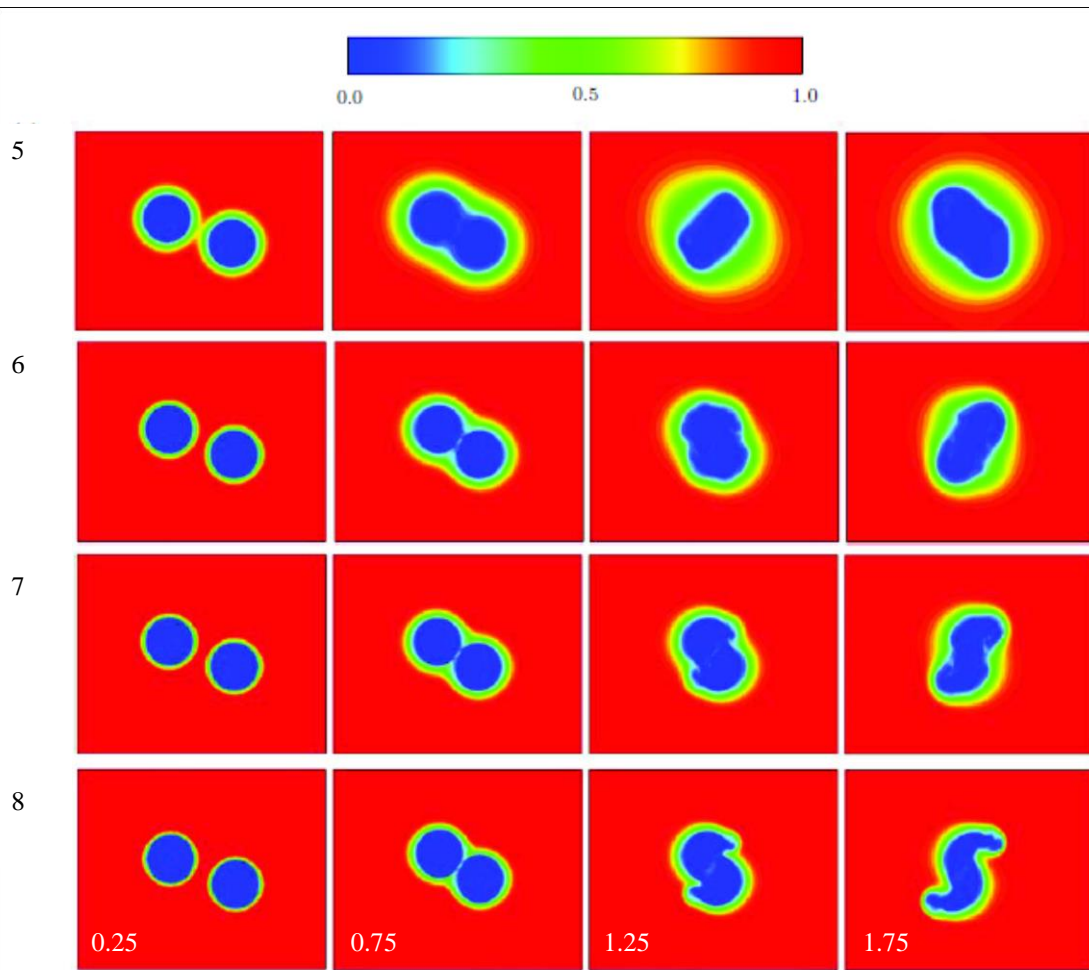**Figure 5.12 Temperature contour for head-on collisions.**

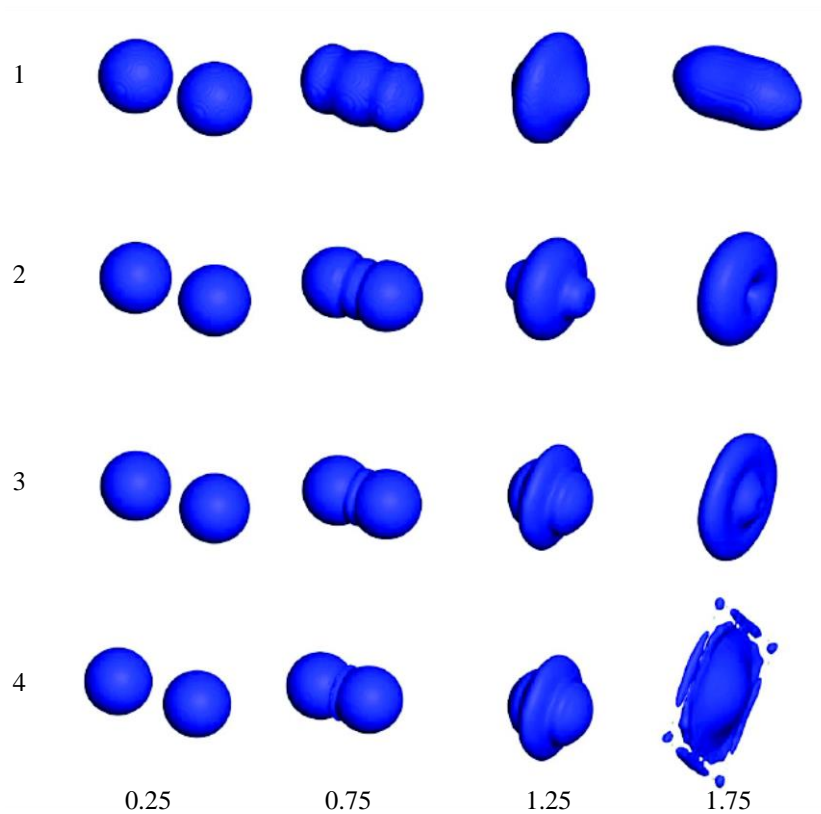**Figure 5.13 Temperature contour for off-center collisions.**

Figure 5.14 Deformations in head-on collisions.

The effect of Reynolds number and Weber number on droplets deformation is shown in Figure 5.16 and Figure 5.17 for head-on and off-center collisions, respectively. As it is observed the extent of deformation of droplets increases by the Reynolds and Weber numbers. In the case of a head-on collision for lower Reynolds and Weber numbers, droplets are first squeezed due to the momentum, but since the surface tension forces are strong enough to prevent droplets to be torn, they start expanding in the orthogonal direction to the collision axis. This elongation is then limited again by the surface tension resulting in an oscillating behavior of droplets which can be seen for cases 1 and 2 in Figure 5.16. For higher Reynolds and Weber numbers this oscillation is not observed since the momentum overcomes the surface tension forces. Therefore, instead of oscillating the surface area keeps increasing due to the elongation of droplets and separation of smaller volumes from the main droplets. For the off-center collision where the centers of droplets are distanced with R_0, the contraction in the area of droplets occurs later in time comparing to the head-on collision. Therefore, the same trend in the variation of the surface area ratio is observed but with a shift in time.
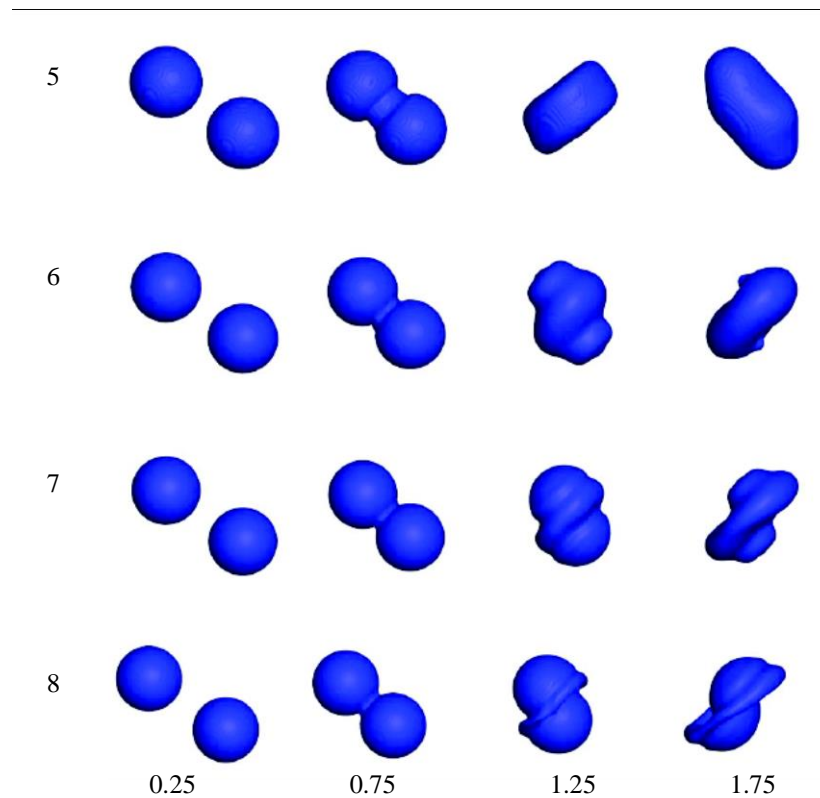
Figure 5.15 Deformations in off-center collisions.

Figure 5.18 and Figure 5.19 show the variation of the average Nusselt number in time for head-on and off-center, respectively. It is observed that a higher Reynolds number and Weber number result in a higher Nusselt number due to larger deformations and the presence of thinner volumes. When deformations are larger the surface area increases which results in higher heat transfer rate and therefore a higher Nusselt number. It is observed in these graphs that the Nusselt number is generally lower for a lower Weber number. According to the definition of the Weber number, for a certain approach velocity a lower value of the Weber number means a higher surface tension, when the surface tension is higher the droplets will rupture more slowly and therefore preserving the enclosed volume of each droplet for longer time. The smaller surface area which is the result of a lower Weber number can result in decreasing the Nusselt number. The comparison between the heat transfer rate in a head-on collision and an off-center collision for the same Reynolds and Weber numbers are shown in Figure 5.20-Figure 5.23. As it is observed, generally the average Nusselt number is higher for the off-center collision for identical Reynolds and Weber numbers but as the Reynolds and Weber number increase the surface area increases more dramatically in a head-on collision due

to the rupture of the droplets and creation of scattered smaller volumes, which results in a higher Nusselt number as shown in Figure 5.23.
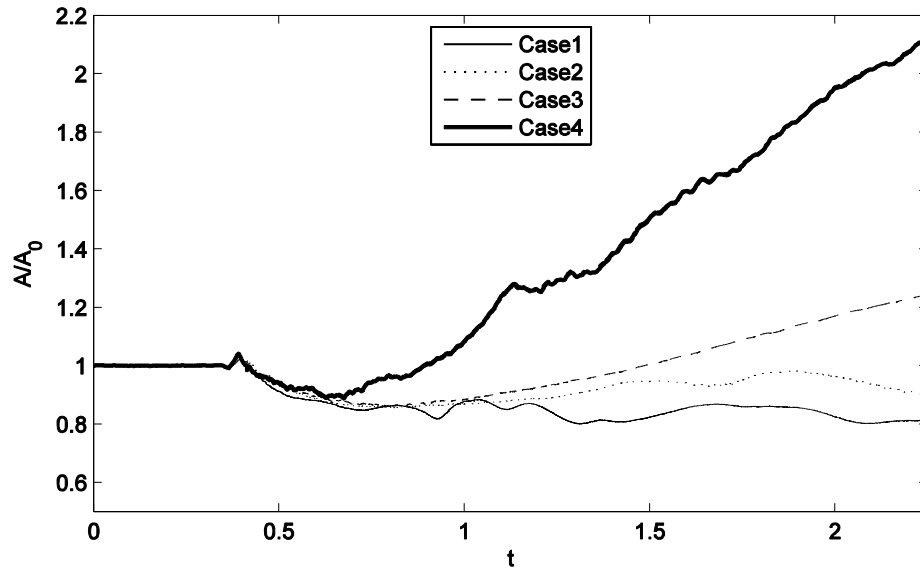

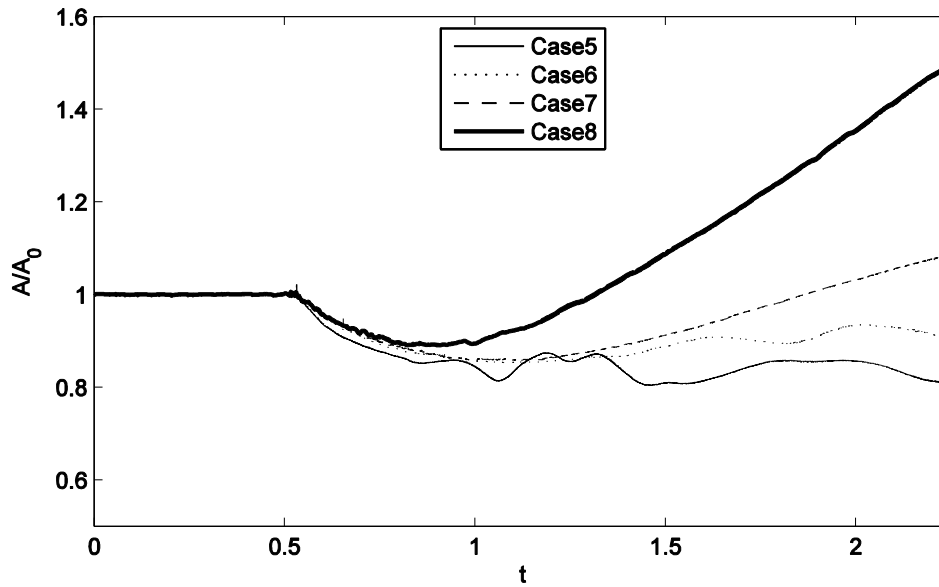**Figure 5.16 Surface area variation for head-on collisions.**

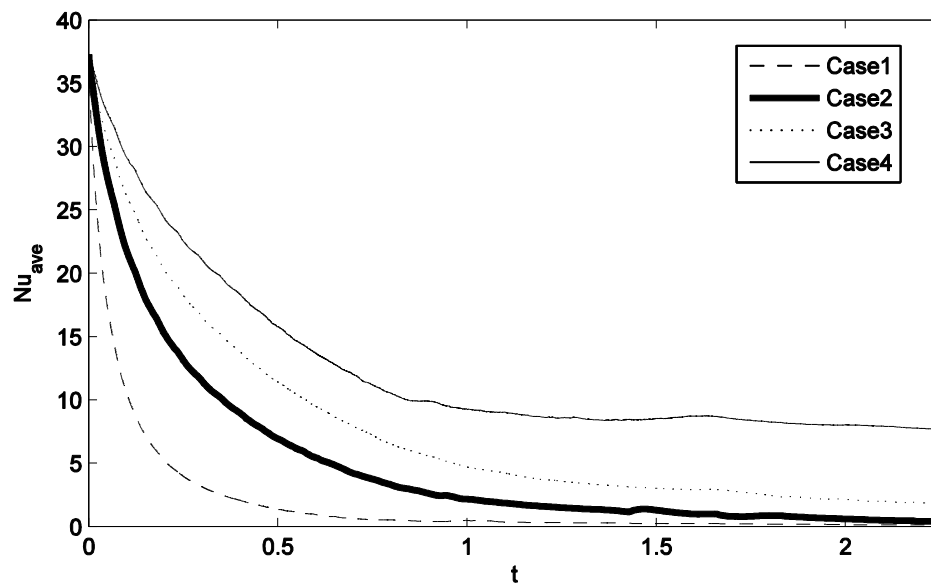**Figure 5.17 Surface area variation for off-center collisions.**

Figure 5.18 Variation of average Nusselt number in time for head-on collisions.
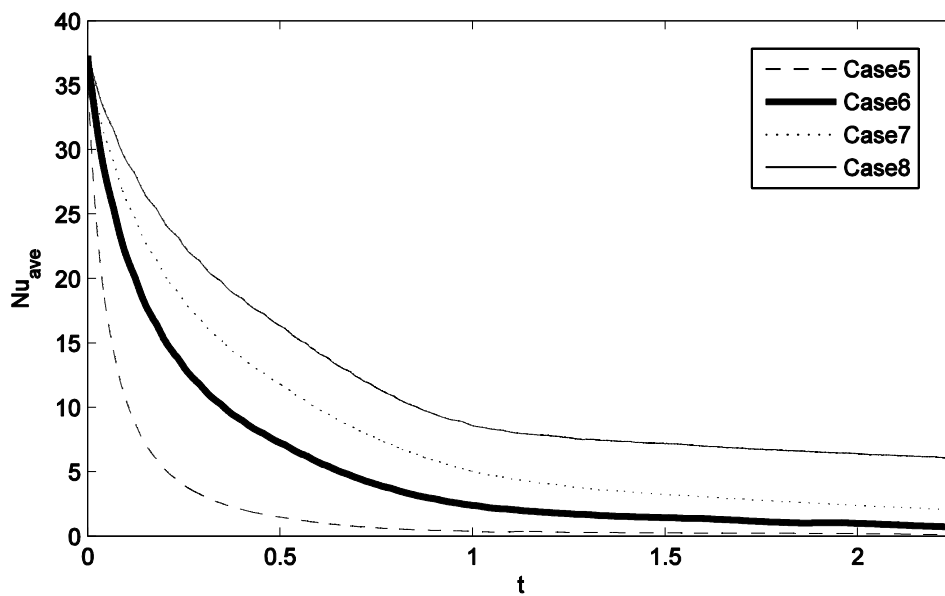

Figure 5.19 Variation of the average Nusselt number for off-center collisions.
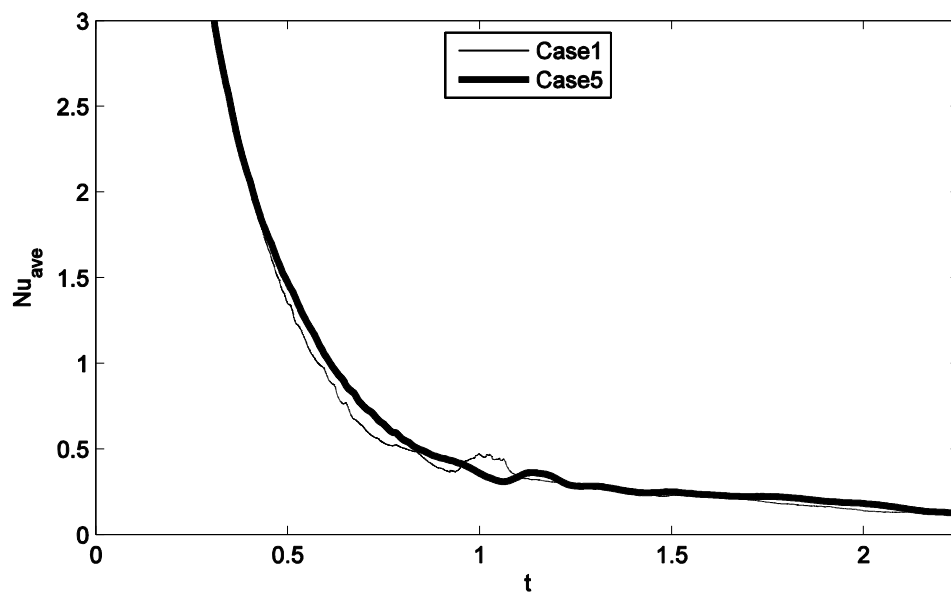
Figure 5.20 Comparison of the average Nusselt number in head-on and off-center collisions for Re=8.77 and We=0.00135.
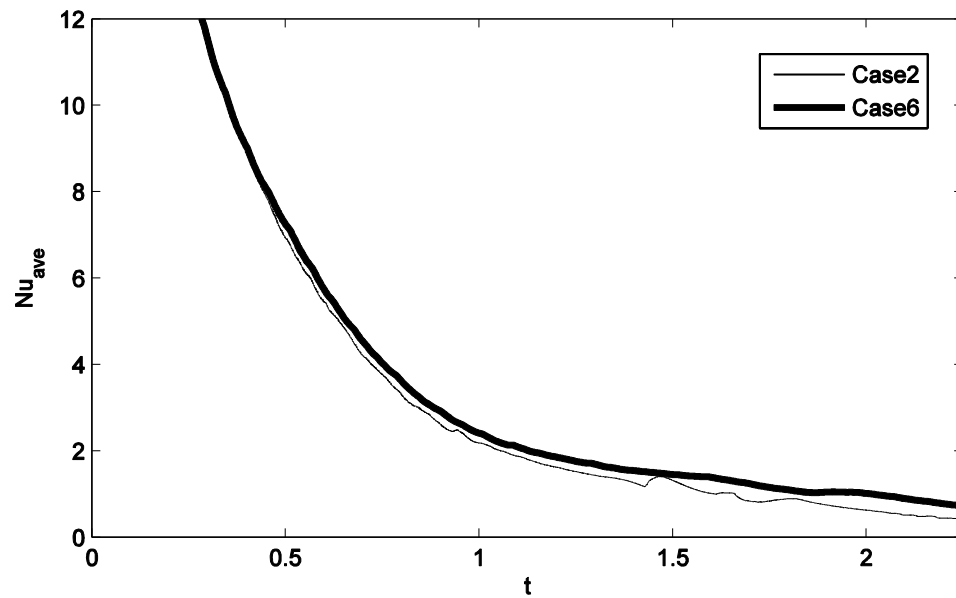

Figure 5.21 Comparison of the average Nusselt number in head-on and off-center collisions for Re=35 and We=0.01351.
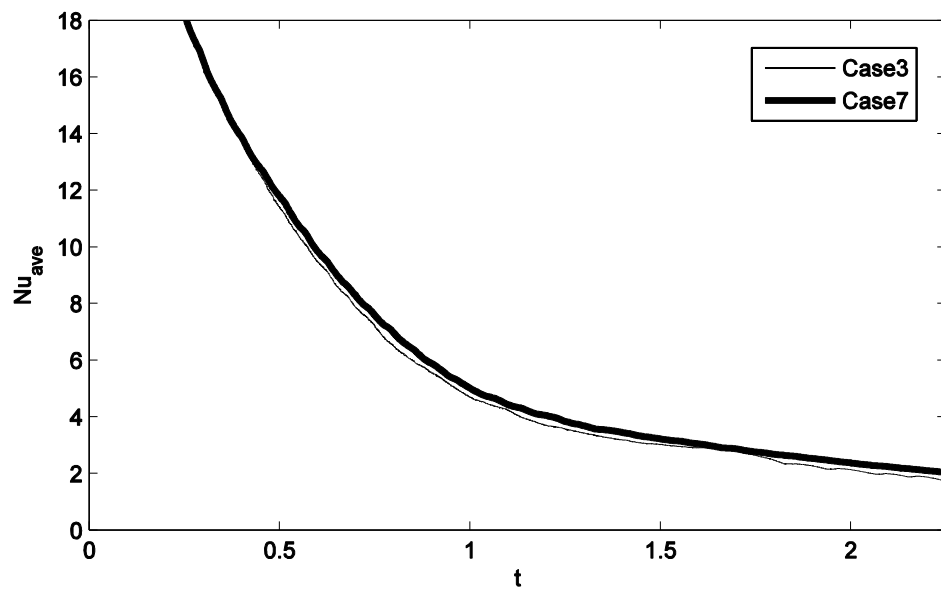
Figure 5.22 Comparison of the average Nusselt number in head-on and off-center collisions for Re=70 and We=0.05404.
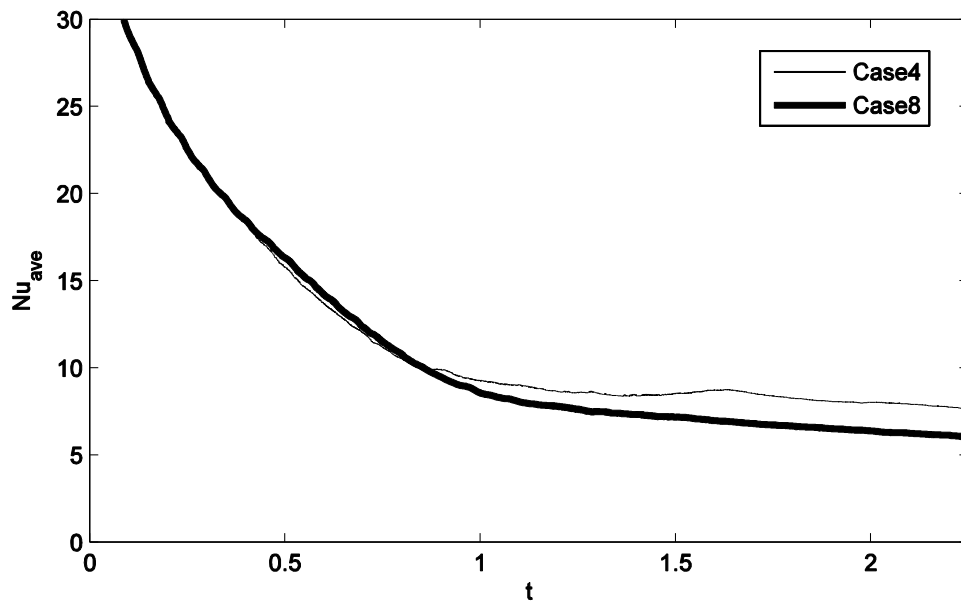

Figure 5.23 Comparison of the average Nusselt number in head-on and off-center collisions for Re=140 and We=0.21616.

5.5   Conclusions

In this chapter the flow and heat transfer in colliding droplets is studied in 3D for different Weber numbers, Reynolds numbers and eccentricity of droplets. Droplets are allowed to deform under the hydrodynamic forces of the surrounding flow. A coupled level-set and volume of fluid (CLSVOF) method is applied to model the highly deforming topology of the droplets. The temperature distribution inside the droplet as well as the outer domain is considered and the consequent effect on the Nusselt number is studied.

The results show that the eccentricity of droplets has a significant effect on the Nusselt number. If the droplets deform considerably due to the collision, the heat transfer from the droplets will be strongly enhanced. It is concluded from the calculations for different Reynolds numbers that heat transfer rate is increased for higher Reynolds numbers. The surface tension controls the extent of deformations, so the larger Weber number for a certain approach velocity results in larger deformations in droplets and therefore a higher heat transfer rate is achieved. The role of using the real surface area of droplets in calculation of the Nusselt number is also studied, it is concluded that in problems with high Weber numbers it is of more importance that the real surface area is used in heat the transfer calculations. On the other hand, for cases with lower Weber numbers in which the deformations are negligible, using the real surface area is not necessary.

Two different solvers for pressure and velocity have been used; an iterative solver and a direct solver. Since the direct solver is computationally less effortful and much faster than the iterative solver it can be applied on finer meshes. Therefore, results with higher resolution and less numerical instabilities can be achieved which makes the direct solver a suitable choice to solve problems with large topological changes.

6   Conclusions and recommendations for future work

In this chapter the results are discussed and some recommendations for future work are given. The goal of this project was to develop a model to simulate heat transfer from multiple colliding and deforming droplets in different flow regimes for different configuration of droplets and physical properties of droplets. In order to achieve this goal, a Coupled Level-Set and Volume-of-Fluid method (CLSVOF) is applied to capture the highly deforming interfaces accurately while mass conservation is also satisfied.

6.1   Conclusions

The governing equations are solved on a fixed grid and since direct methods are used no closure terms are required to be added. Small scales as well as large scale phenomena are well captured in the simulations. Since the level-set function is used in the simulations, the calculation of the normal vector to the interface at every computational cell is straightforward and consequently is the calculation of the Nusselt number where the normal vector is required. Using parallel computing gives higher speed to the computations and thus makes it possible to use the model for higher number of droplets without affecting the computation time significantly. In order to have a good overview of the heat transfer phenomena from spherical objects, solid spheres, single falling droplet and colliding droplets are studied.

In the study of heat transfer from solid spheres the Biot number plays an important role. For *Bi<<1* the conduction inside of the body is dominant and therefore the temperature of the body can be assumed uniform. For systems with *Bi≥1* the internal temperature distribution should also be considered. The results show that the internal temperature distribution affects the heat transfer rate significantly. Therefore, to have a reliable estimation of the local Nusselt number, the internal temperature distribution and the local variation of the surface temperature of the particle should also be considered. The result of the mesh sensitivity study shows that the grid resolution while does not significantly affect the average Nusselt number but affects the local Nusselt number at the front stagnation point and at the rear of the particle, therefore a proper mesh resolution should be used.

In the study of heat transfer over a falling and deforming water droplet in air for different Weber and Reynolds numbers, the results show that the internal temperature distribution affects the heat transfer rate significantly. Therefore, in order to have a reliable estimation of the local Nusselt number, the internal temperature distribution should be considered. In this way the correct local surface temperature of the droplet which is used in the Nusselt number calculations is obtained. By looking into the variation of the surface area of droplet due to falling it is observed that a cyclic deformation occurs for which the period increases by increasing the Weber number. Since in the calculation of the Nusselt number the surface area is used, it is important to use the correct surface area from which the heat is being transferred.

The sensitivity study of the heat transfer rate to the Reynolds number and the Weber number shows that increasing the Reynolds number and Weber number both increase the Nusselt number. However, the effect of the Reynolds number variation is more significant as an increase of 100% in the Reynolds number results in an increase of 20% in the

Nusselt number. While an increase of 250% of the Weber number only results in decreasing the Nusselt number for about 3%. An increase in the Reynolds number increases the convection heat transfer rate while increasing the Weber number results in cyclic deformations in the droplet that decreases the heat transfer rate.

The flow and heat transfer in colliding droplets is studied in 3D for different Weber numbers, Reynolds numbers and eccentricity of droplets. Droplets are allowed to deform under the hydrodynamic forces of the surrounding flow. A coupled level-set and volume of fluid (CLSVOF) method is applied to model the highly deforming topology of the droplets. The temperature distribution inside the droplet as well as the outer domain is considered and the consequent effect on the Nusselt number is studied.

The results show that the eccentricity of droplets has a significant effect on the Nusselt number. If the droplets deform considerably due to the collision, the heat transfer from the droplets will be strongly enhanced. It is concluded from the calculations for different Reynolds numbers that heat transfer rate is increased by increasing the Reynolds number. The surface tension controls the extent of deformations, so increasing the Weber number for a certain approach velocity results in larger deformations in droplets and therefore a higher heat transfer rate is achieved. The role of using the real surface area of droplets in calculation of the Nusselt number is also studied, it is concluded that in problems with high Weber numbers it is required that the real surface area is used in the heat transfer calculations. On the other hand, for cases with lower Weber numbers in which the deformations are negligible, using the real surface area is not necessary.

In the study of flow and heat transfer in colliding droplets two different solvers for pressure and velocity have been used: an iterative solver and a direct solver. Since the direct solver is computationally less effortful and much faster than the iterative solver it can be applied on finer meshes. Therefore, results with higher resolution and less numerical instabilities can be achieved which makes the direct solver a suitable choice to solve problems with large topological changes.

6.2   Recommendations for future work

As the next step in heat transfer study, the evaporation problem can be considered. The problem of evaporation of a single droplet or a spray of droplets has been studied for a few decades both numerically and experimentally. In modeling evaporation problem different assumptions have been made to simplify the computation process. Considering

the droplet to remain a sphere for its whole life time and considering uniform surface temperature for droplets are examples of such assumptions.

As a future step, this model can be used to solve evaporation of droplets by adding another volume of fluid function for the vapor phase as in Schlottke and Weigand (2008) and Eisenschmidt et al. (2016). In this way the vapor phase can also be tracked in the domain and the shrinkage of the droplets due to evaporation can be included as well. Also by using a direct solver as introduced by Dodd and Ferrante (2014) for pressure and velocity, finer mesh with higher numerical stability can be used to capture the interface changes more accurately with less computational effort.

The momentum equation remains the same for this problem as equation (2.8), but since due to evaporation some liquid mass is changed into vapor, the continuity equation will need some modifications and it can be written as:

$$\nabla \cdot \mathbf{u} = -\dot{m}''' \left(\frac{1}{\rho_v} - \frac{1}{\rho_l} \right) \tag{6.1}$$

If the droplets are assumed to be at the saturation temperature at the beginning of the simulations the energy equation can remain as equation (2.9). If droplets are at a temperature lower than the saturation temperature the energy equation also needs some modifications. In this case the latent heat of evaporation should be considered in the energy equation, so it can be written as:

$$\frac{\partial \left(\rho C_p T \right)}{\partial t} + \nabla \cdot \left(\rho C_p \mathbf{u} T \right) = \nabla \cdot \left(k \nabla T \right) + \dot{m}''' h_{lg} \tag{6.2}$$

In which $\dot{m}'''$ is the evaporation rate per unit volume.

When evaporation is present, the equations for continuity of momentum, energy and mass as follows are required at the interface:

$$\left[\mathbf{u} \right]_{\Gamma} = -\dot{m}'' \left(\frac{1}{\rho_v} - \frac{1}{\rho_l} \right) \cdot \mathbf{n} \tag{6.3}$$

$$\left[k \nabla T \cdot \mathbf{n} \right]_{\Gamma} = \dot{m}'' h_{lg} \tag{6.4}$$

$$\left[\rho D_m \nabla Y \cdot \mathbf{n}\right]_\Gamma = \dot{m}''\left(Y_l - Y_g\right) \tag{6.5}$$

Where $[.]_\Gamma$ represents a jump across the interface, $\mathbf{n}$ denotes the interface normal vector, $\dot{m}''$ is the evaporation rate per unit surface and h_{lg} is the latent heat of the evaporation.

In dealing with evaporation problem with the CLSVOF method, an additional VOF function should be introduced for the vapor phase, so the transport equation for the vapor phase can be written as:

$$\frac{\partial \psi_v}{\partial t} + \nabla \cdot \left(\mathbf{u}_g \psi_v\right) = \nabla \cdot \left(D_{vg} \nabla \psi_v\right) + \frac{\dot{m}'''}{\rho_v} \tag{6.6}$$

And the transport equation of the liquid phase should be modified as:

$$\frac{\partial \psi_l}{\partial t} + \nabla \cdot \left(\mathbf{u}_\Gamma \psi_l\right) = -\frac{\dot{m}'''}{\rho_l} \tag{6.7}$$

When there are two VOF functions in the domain, they should both be considered in the computation of the thermophysical variables.

$$\mu(\mathbf{x},t) = \mu_l \psi_l(\mathbf{x},t) + \mu_v \psi_v(\mathbf{x},t) + \mu_g\left(1 - \psi_l(\mathbf{x},t) - \psi_v(\mathbf{x},t)\right) \tag{6.8}$$

$$\rho(\mathbf{x},t) = \rho_l \psi_l(\mathbf{x},t) + \rho_v \psi_v(\mathbf{x},t) + \rho_g\left(1 - \psi_l(\mathbf{x},t) - \psi_v(\mathbf{x},t)\right) \tag{6.9}$$

$$c_p(\mathbf{x},t) = c_{p_l} \psi_l(\mathbf{x},t) + c_{p_v} \psi_v(\mathbf{x},t) + c_{p_g}\left(1 - \psi_l(\mathbf{x},t) - \psi_v(\mathbf{x},t)\right) \tag{6.10}$$

$$k(\mathbf{x},t) = k_l \psi_l(\mathbf{x},t) + k_v \psi_v(\mathbf{x},t) + k_g\left(1 - \psi_l(\mathbf{x},t) - \psi_v(\mathbf{x},t)\right) \tag{6.11}$$

The non-dimensional thermophysical properties used in the non-dimensional Navier-Stokes equations, the energy equation and the interface conditions are defined by:

$$\mu = 1 + \left(\frac{\mu_l}{\mu_g} - 1\right)\psi_l(\mathbf{x},t) + \left(\frac{\mu_v}{\mu_g} - 1\right)\psi_v(\mathbf{x},t) \tag{6.12}$$

$$\rho = 1 + \left(\frac{\rho_l}{\rho_g} - 1 \right) \psi_l(\mathbf{x}, t) + \left(\frac{\rho_v}{\rho_g} - 1 \right) \psi_v(\mathbf{x}, t) \tag{6.13}$$

$$c_p = 1 + \left(\frac{c_{p_l}}{c_{p_g}} - 1 \right) \psi_l(\mathbf{x}, t) + \left(\frac{c_{p_v}}{c_{p_g}} - 1 \right) \psi_v(\mathbf{x}, t) \tag{6.14}$$

$$k = 1 + \left(\frac{k_l}{k_g} - 1 \right) \psi_l(\mathbf{x}, t) + \left(\frac{k_v}{k_g} - 1 \right) \psi_v(\mathbf{x}, t) \tag{6.15}$$

Bibliography

Abdelouahab, M. & R. Gatignol (2016) Study of falling water drop in stagnant air. *European Journal of Mechanics - B/Fluids,* 60**,** 82-89.

Abou Al-Sood, M. M. & M. Birouk (2008) Droplet heat and mass transfer in a turbulent hot airstream. *International Journal of Heat and Mass Transfer,* 51**,** 1313-1324.

Abramzon, B. & W. A. Sirignano (1989) Droplet vaporization model for spray combustion calculations. *International Journal of Heat and Mass Transfer,* 32**,** 1605-1618.

Al-Sharafi, A., B. S. Yilbas & H. Ali (2017) Droplet heat transfer on micro-post arrays: Effect of droplet size on droplet thermal characteristics. *International Journal of Heat and Fluid Flow,* 68**,** 62-78.

Anderson, A., X. Zheng & V. Cristini (2005) Adaptive unstructured volume remeshing – I: The method. *Journal of Computational Physics,* 208**,** 616-625.

Badalassi, V. E., H. D. Ceniceros & S. Banerjee (2003) Computation of multiphase systems with phase field models. *Journal of Computational Physics,* 190**,** 371-397.

Bagchi, P., M. Y. Ha & S. Balachandar (2000) Direct Numerical Simulation of Flow and Heat Transfer From a Sphere in a Uniform Cross-Flow. *Journal of Fluids Engineering,* 123**,** 347-358.

Banerjee, R. (2013) Numerical investigation of evaporation of a single ethanol/iso-octane droplet. *Fuel,* 107**,** 724-739.

Beard, K. V. K. K. V. (1971) A wind tunnel investigation of the rate of evaporation of small water drops falling at terminal velocity in air. *J. Atmos. Sci.,* 28**,** 1455-1464.

Becker, E., W. J. Hiller & T. A. Kowalewski (2006) Experimental and theoretical investigation of large-amplitude oscillations of liquid droplets. *Journal of Fluid Mechanics,* 231**,** 189-210.

Bird, R. B., W. E. Stewart & E. N. Lightfoot. 2007. *Transport phenomena.* New York: Wiley.

Brackbill, J. U., D. B. Kothe & C. Zemach (1992) A continuum method for modeling surface tension. *Journal of Computational Physics,* 100**,** 335-354.

Castanet, G., A. Labergue & F. Lemoine (2011) Internal temperature distributions of interacting and vaporizing droplets. *International Journal of Thermal Sciences,* 50**,** 1181-1190.

Chang, Y. C., T. Y. Hou, B. Merriman & S. Osher (1996) A Level Set Formulation of Eulerian Interface Capturing Methods for Incompressible Fluid Flows. *Journal of Computational Physics,* 124**,** 449-464.

Chatzikyriakou, D., S. P. Walker, C. P. Hale & G. F. Hewitt (2011) The measurement of heat transfer from hot surfaces to non-wetting droplets. *International Journal of Heat and Mass Transfer,* 54**,** 1432-1440.

Che Sidik, N. A. & M. R. Niaki Attarzadeh (2012) The use of cubic interpolation method for transient hydrodynamics of solid particles. *International Journal of Engineering Science,* 51**,** 90-103.

Che, Z., T. N. Wong, N.-T. Nguyen & C. Yang (2015) Three dimensional features of convective heat transfer in droplet-based microchannel heat sinks. *International Journal of Heat and Mass Transfer,* 86**,** 455-464.

Chen, T. S. & A. Mucoglu (1977) Analysis of mixed forced and free convection about a sphere. *International Journal of Heat and Mass Transfer,* 20**,** 867-875.

Chiu, P.-H. & Y.-T. Lin (2011) A conservative phase field method for solving incompressible two-phase flows. *Journal of Computational Physics,* 230**,** 185-204.

Clift, R., J. R. Grace & M. E. Weber. 1978. *Bubbles, drops, and particles*. New York :: Academic Press.

Comer, J. K. & C. Kleinstreuer (1995) Computational analysis of convection heat transfer to non-spherical particles. *International Journal of Heat and Mass Transfer,* 38**,** 3171-3180.

Coyajee, E. & B. J. Boersma (2009) Numerical simulation of drop impact on a liquid-liquid interface with a multiple marker front-capturing method. *Journal of Computational Physics,* 228**,** 4444-4467.

Dan, C. & A. Wachs (2010) Direct Numerical Simulation of particulate flow with heat transfer. *International Journal of Heat and Fluid Flow,* 31**,** 1050-1057.

Dandy, D. S. & H. A. Dwyer (1990) Sphere in shear flow at finite Reynolds number. Effect of shear on particle lift, drag, and heat transfer. *Journal of Fluid Mechanics,* 216**,** 381-410.

Davidson, M. R. & M. J. Rudman (2001) A NUMERICAL METHOD FOR HEAT TRANSFER ACROSS DEFORMING FLUID INTERFACES. 4**,** 437-444.

Dodd, M. S. & A. Ferrante (2014) A fast pressure-correction method for incompressible two-fluid flows. *Journal of Computational Physics,* 273**,** 416-434.

Eisenschmidt, K., M. Ertl, H. Gomaa, C. Kieffer-Roth, C. Meister, P. Rauschenberger, M. Reitzle, K. Schlottke & B. Weigand (2016) Direct numerical simulations for multiphase flows: An overview of the multiphase code FS3D. *Applied Mathematics and Computation,* 272**,** 508-517.

Falcão, D. S., J. P. Pereira & A. M. F. R. Pinto (2016) Numerical simulations of anode two-phase flow in Micro-DMFC using the volume of fluid method. *International Journal of Hydrogen Energy,* 41**,** 19724-19730.

Feng, Z. G. & E. E. Michaelides (2001) A numerical study on the transient heat transfer from a sphere at high Reynolds and Peclet numbers. *International Journal of Heat and Mass Transfer,* 43**,** 219-229.

Fornberg, B. (1988) Steady viscous flow past a sphere at high Reynolds numbers. *Journal of Fluid Mechanics,* 190**,** 471-489.

Fujita, A., R. Kurose & S. Komori (2010) Experimental study on effect of relative humidity on heat transfer of an evaporating water droplet in air flow. *International Journal of Multiphase Flow,* 36**,** 244-247.

Galloway, T. R. & B. H. Sage (1964) Thermal and material transfer in turbulent gas streams-A method of prediction for spheres. *International Journal of Heat and Mass Transfer,* 7**,** 283-291.

Gibou, F., L. Chen, D. Nguyen & S. Banerjee (2007) A level set based sharp interface method for the multiphase incompressible Navier–Stokes equations with phase change. *Journal of Computational Physics,* 222**,** 536-555.

Gilmanov, A. & S. Acharya (2008) A computational strategy for simulating heat transfer and flow past deformable objects. *International Journal of Heat and Mass Transfer,* 51**,** 4415-4426.

Glimm, J. & O. A. McBryan (1985) A computational model for interfaces. *Advances in Applied Mathematics,* 6**,** 422-435.

Gostkowski, V. J. & F. A. Costello (1970) The effect of free stream turbulence on the heat transfer from the stagnation point of a sphere. *International Journal of Heat and Mass Transfer,* 13**,** 1382-1386.

Hase, M. & B. Weigand (2004) Transient heat transfer of deforming droplets at high Reynolds numbers. *International Journal of Numerical Methods for Heat and Fluid Flow,* 14**,** 85-97.

Hayward, G. L. & D. C. T. Pei (1978) Local heat transfer from a single sphere to a turbulent air stream. *International Journal of Heat and Mass Transfer,* 21**,** 35-41.

Haywood, R. J., M. Renksizbulut & G. D. Raithby (1994) Transient deformation and evaporation of droplets at intermediate Reynolds numbers. *International Journal of Heat and Mass Transfer,* 37**,** 1401-1409.

Hirt, C. W. & B. D. Nichols (1981) Volume of fluid (VOF) method for the dynamics of free boundaries. *Journal of Computational Physics,* 39**,** 201-225.

Hou, T. Y., J. S. Lowengrub & M. J. Shelley (2001) Boundary Integral Methods for Multicomponent Fluids and Multiphase Materials. *Journal of Computational Physics,* 169**,** 302-362.

Hu, C. & M. Kashiwagi (2004) A CIP-based method for numerical simulations of violent free-surface flows. *Journal of Marine Science and Technology,* 9**,** 143-157.

Hu, C., S. Xia, C. Li & G. Wu (2017) Three-dimensional numerical investigation and modeling of binary alumina droplet collisions. *International Journal of Heat and Mass Transfer,* 113**,** 569-588.

Hua, J. & J. Lou (2007) Numerical simulation of bubble rising in viscous liquid. *Journal of Computational Physics,* 222**,** 769-795.

Irfan, M. & M. Muradoglu (2017) A front tracking method for direct numerical simulation of evaporation process in a multiphase system. *Journal of Computational Physics,* 337**,** 132-153.

Ishii, M. & K. Mishima (1984) Two-fluid model and hydrodynamic constitutive relations. *Nuclear Engineering and Design,* 82**,** 107-126.

Jain, D., Y. Man Lau, H. Kuipers & N. Deen. 2013. *Discrete bubble modeling for a micro-structured bubble column.*

Jeong, S. H., G. H. Yoon, A. Takezawa & D.-H. Choi (2014) Development of a novel phase-field method for local stress-based shape and topology optimization. *Computers & Structures,* 132**,** 84-98.

Jia, W. & H. H. Qiu (2003) Experimental investigation of droplet dynamics and heat transfer in spray cooling. *Experimental Thermal and Fluid Science,* 27**,** 829-838.

Jin, Y. & B. D. Shaw (2010) Computational modeling of n-heptane droplet combustion in air–diluent environments under reduced-gravity. *International Journal of Heat and Mass Transfer,* 53**,** 5782-5791.

Juncu, G. (2010) A numerical study of the unsteady heat/mass transfer inside a circulating sphere. *International Journal of Heat and Mass Transfer,* 53**,** 3006-3012.

Kadioglu, S. Y. & M. Sussman (2008) Adaptive solution techniques for simulating underwater explosions and implosions. *Journal of Computational Physics,* 227**,** 2083-2104.

Kang, M., R. P. Fedkiw & X.-D. Liu (2000) A Boundary Condition Capturing Method for Multiphase Incompressible Flow. *Journal of Scientific Computing,* 15**,** 323-360.

Koblitz, A. R., S. Lovett, N. Nikiforakis & W. D. Henshaw (2017) Direct numerical simulation of particulate flows with an overset grid method. *Journal of Computational Physics,* 343**,** 414-431.

Kwakkel, M., W.-P. Breugem & B. J. Boersma (2013) Extension of a CLSVOF method for droplet-laden flows with a coalescence/breakup model. *Journal of Computational Physics,* 253**,** 166-188.

Magarvey, R. H. & R. L. Bishop (1961) TRANSITION RANGES FOR THREE-DIMENSIONAL WAKES. *Canadian Journal of Physics,* 39**,** 1418-1422.

Matsumoto, M. (2015) Application of the Constrained Interpolation Profile (CIP) scheme to two-dimensional single-phase hydrothermal reservoir simulations. *Geothermics,* 54**,** 10-22.

McKenney, A., L. Greengard & A. Mayo (1995) A Fast Poisson Solver for Complex Geometries. *Journal of Computational Physics,* 118**,** 348-355.

Mohammadi, M., S. Shahhosseini & M. Bayat (2012) Direct numerical simulation of water droplet coalescence in the oil. *International Journal of Heat and Fluid Flow,* 36**,** 58-71.

Morris, S. (1982) EFFECTS OF A STRONGLY TEMPERATURE-DEPENDENT VISCOSITY ON SLOW FLOW PAST A HOT SPHERE. *Journal of Fluid Mechanics,* 124**,** 1-26.

Nguyen, H. D., S. Paik & J. N. Chung (1993) Unsteady Conjugate Heat Transfer Associated with a Translating Spherical Droplet: A Direct Numerical Simulation. *Numerical Heat Transfer, Part A: Applications,* 24**,** 161-180.

Niazmand, H. & M. Renksizbulut (2003) Transient three-dimensional heat transfer from rotating spheres with surface blowing. *Chemical Engineering Science,* 58**,** 3535-3554.

Nikolopoulos, N., G. Strotos, K. S. Nikas & G. Bergeles (2012) The effect of Weber number on the central binary collision outcome between unequal-sized droplets. *International Journal of Heat and Mass Transfer,* 55**,** 2137-2150.

Noh, W. F. & P. Woodward. 1976. SLIC (Simple Line Interface Calculation). In *Proceedings of the Fifth International Conference on Numerical Methods in Fluid Dynamics June 28 – July 2, 1976 Twente University, Enschede,* eds. A. van de Vooren & P. Zandbergen, 330-340. Springer Berlin Heidelberg.

Oldenziel, G. 2014. *Droplet collisions in turbulence an experimental study Online resource.* S.l: S.n.

Pan, Y. & K. Suga (2005) Numerical simulation of binary liquid droplet collision. *Physics of Fluids,* 17**,** 1-14.

Petera, J. & L. R. Weatherley (2001) Modelling of mass transfer from falling droplets. *Chemical Engineering Science,* 56**,** 4929-4947.

Portela, L. M. & R. V. A. Oliemans (2006) Possibilities and Limitations of Computer Simulations of Industrial Turbulent Dispersed Multiphase Flows. *Flow, Turbulence and Combustion,* 77**,** 381-403.

Prakash, S. & W. A. Sirignano (1980) Theory of convective droplet vaporization with unsteady heat transfer in the circulating liquid phase. *International Journal of Heat and Mass Transfer,* 23**,** 253-268.

Puckett, E. G., A. S. Almgren, J. B. Bell, D. L. Marcus & W. J. Rider (1997) A High-Order Projection Method for Tracking Fluid Interfaces in Variable Density Incompressible Flows. *Journal of Computational Physics,* 130**,** 269-282.

Qin, N., X. Liu & H. Xia. 2005. *An Efficient Moving Grid Algorithm for Large Deformation.*

Quan, S. (2011) Simulations of multiphase flows with multiple length scales using moving mesh interface tracking with adaptive meshing. *Journal of Computational Physics, 230,* 5430-5448.

Quan, S., J. Lou & D. P. Schmidt (2009) Modeling merging and breakup in the moving mesh interface tracking method for multiphase flow simulations. *Journal of Computational Physics,* 228, 2660-2675.

Quan, S. & D. P. Schmidt (2007) A moving mesh interface tracking method for 3D incompressible two-phase flows. *Journal of Computational Physics, 221,* 761-780.

Renksizbulut, M. & R. J. Haywood (1988) Transient droplet evaporation with variable properties and internal circulation at intermediate reynolds numbers. *International Journal of Multiphase Flow,* 14, 189-202.

Santarelli, C. & J. Fröhlich (2015) Direct Numerical Simulations of spherical bubbles in vertical turbulent channel flow. *International Journal of Multiphase Flow, 75,* 174-193.

Sayegh, N. N. N. N. N. (1979) NUMERICAL ANALYSIS OF VARIABLE PROPERTY HEAT TRANSFER TO A SINGLE SPHERE IN HIGH TEMPERATURE SURROUNDINGS. *AIChE Journal,* 25, 522-534.

Schlottke, J. & B. Weigand (2008) Direct numerical simulation of evaporating droplets. *Journal of Computational Physics,* 227, 5215-5237.

Sultana, K. R., K. Pope, L. S. Lam & Y. S. Muzychka (2017) Phase change and droplet dynamics for a free falling water droplet. *International Journal of Heat and Mass Transfer,* 115, 461-470.

Sun, K., P. Zhang, M. Jia & T. Wang (2018) Collision-induced jet-like mixing for droplets of unequal-sizes. *International Journal of Heat and Mass Transfer,* 120, 218-227.

Sussman, M. & E. G. Puckett (2000) A Coupled Level Set and Volume-of-Fluid Method for Computing 3D and Axisymmetric Incompressible Two-Phase Flows. *Journal of Computational Physics,* 162, 301-337.

Takizawa, K., T. Yabe, Y. Tsugawa, T. Tezduyar & H. Mizoe (2007) Computation of free-surface flows and fluid–object interactions with the CIP method based on adaptive meshless soroban grids. *Computational Mechanics,* 40, 167-183.

Tan, Z., K. M. Lim & B. C. Khoo (2007) An adaptive mesh redistribution method for the incompressible mixture flows using phase-field model. *Journal of Computational Physics,* 225, 1137-1158.

Tanguy, S., T. Ménard & A. Berlemont (2007) A Level Set Method for vaporizing two-phase flows. *Journal of Computational Physics, 221,* 837-853.

Tavassoli, H., S. H. L. Kriebitzsch, M. A. van der Hoef, E. A. J. F. Peters & J. A. M. Kuipers (2013) Direct numerical simulation of particulate flow with heat transfer. *International Journal of Multiphase Flow,* 57, 29-37.

ten Cate, A., C. H. Nieuwstad, J. J. Derksen & H. E. A. Van den Akker (2002) Particle imaging velocimetry experiments and lattice-Botlzmann simulations on a single sphere settling under gravity. *Physics of Fluids, 14,* 4012-4025.

Tryggvason, G., B. Bunner, A. Esmaeeli, D. Juric, N. Al-Rawahi, W. Tauber, J. Han, S. Nas & Y. J. Jan (2001) A Front-Tracking Method for the Computations of Multiphase Flow. *Journal of Computational Physics, 169,* 708-759.

Tryggvason, G., A. Esmaeeli, J. Lu & S. Biswas (2006) Direct numerical simulations of gas/liquid multiphase flows. *Fluid Dynamics Research, 38,* 660-681.

Tryggvason, G. t., R. Scardovelli & S. p. Zaleski. 2011. *Direct numerical simulations of gas-liquid multiphase flows*. Cambridge: Cambridge University Press.

Unverdi, S. O. & G. Tryggvason (1992) A front-tracking method for viscous, incompressible, multi-fluid flows. *Journal of Computational Physics,* 100**,** 25-37.

Vanella, M., A. Posa & E. Balaras (2014) Adaptive Mesh Refinement for Immersed Boundary Methods. *Journal of Fluids Engineering,* 136**,** 040909-040909-9.

Waterson, N. P. & H. Deconinck (2007) Design principles for bounded higher-order convection schemes – a unified approach. *Journal of Computational Physics,* 224**,** 182-207.

Welch, S. W. J. & J. Wilson (2000) A Volume of Fluid Based Method for Fluid Flows with Phase Change. *Journal of Computational Physics,* 160**,** 662-682.

Whitaker, S. S. S. (1972) AIChE Journal. 18.

Woo, S. E. & A. E. Hamielec (1971) A Numerical Method of Determining the Rate of Evaporation of Small Water Drops Falling at Terminal Velocity in Air. *Journal of the Atmospheric Sciences,* 28**,** 1448-1454.

Yabe, T., F. Xiao & T. Utsumi (2001) The Constrained Interpolation Profile Method for Multiphase Analysis. *Journal of Computational Physics,* 169**,** 556-593.

Zhang, P. & C. K. Law (2011) An analysis of head-on droplet collision with large deformation in gaseous medium. *Physics of Fluids,* 23**,** 042102.

Acknowledgements

The day has finally come for me to write these lines to express my deepest gratitude to the people who encouraged, inspired and supported me during this journey.

First of all I would like to thank my promotor, Bendiks Jan Boersma for sharing his knowledge and supporting me while giving me freedom to find my way during this research. I thank you for your help and advice which made this thesis possible. I remember during one of our first progress meetings when I was anxious to get results fast, you advised me to enjoy the journey and not only focus on the destination. Well, it was a difficult journey, sometimes impossible to enjoy but now looking back at what I have learned and achieved personally and professionally I am grateful for every single moment of it.

I would like to thank Hassan Nemati for his invaluable support which made this work possible. I deeply admire and appreciate your knowledge in numerical methods and your expertise and brilliance in developing and executing numerical simulations.

I would like to thank Wim Paul Breugem and Marcel Kwakkel for their support during this research, I really appreciate the productive technical discussions we had during the past years. Being a part of a team was always important to me, and that I could achieve with our group meetings during the first year of my PhD. I would like to show my gratitude to Gosse Oldenziel as a member of that group, and later on as a colleague at Deltares. I think I never thanked you for introducing me to Francois Clemens which resulted in me working at Deltares for two life changing years. I really appreciate you and Francois for your trust and support.

Along this journey I was privileged to meet brilliant officemates with whom I still cherish the friendship. "Onursaaal" Yakaboylu and Gerasimos Sarras thank you for being there for me during my hardest times and supporting me. I am very grateful to have such knowledgeable friends to learn from.

Curriculum Vitae

Nafiseh Talebanfard was born on 18th September 1983 in Shiraz, Iran. She got her Bachelor's degree in Mechanical Engineering specialized in heat and flow from Ferdowsi University of Mashhad in 2005. She got her Master's degree in Mechanical Engineering specialized in Energy Conversion from Ferdowsi University of Mashhad in 2008. During her Master's and until 2010 she was working as a Hydromechanical Engineer at Toossab Consulting Engineers Co. in Mashhad, Iran.

In 2010 she moved to the Netherlands to start her doctoral research at Process & Energy department of Delft University of Technology, under supervision of Prof. B.J. Boersma on Numerical study of heat and flow in colliding droplets.

In 2012 she joined Deltares in Delft, the Netherlands as an Advisor/Researcher in Industrial Hydrodynamics department for two years. Since 2014 she has joined ASML in Veldhoven, the Netherlands in EUV Scanner Thermal Architecture group and at the moment she is working there as a Thermal Architect.

Publications

Talebanfard, N., Nemati, H. and Boersma, B.J., "Heat transfer in deforming droplets with a direct solver for a coupled level-set and volume of fluid Method", accepted by the International Communications in Heat and Mass Transfer, 2017.

Talebanfard, N. and Boersma, B.J., "Direct numerical simulation of heat transfer in colliding droplets by a coupled level set and volume of fluid method", Direct and large eddy simulation 9, Dresden, Germany, April 3-5, 2013.

Talebanfard, N. and Boersma, B.J., "Numerical simulation of heat transfer of a spherical particle in an air stream", Advances in Computational Heat Transfer, CHT-12, Bath, England, July 1-6, 2012.